1518

Dissociation and ionization dynamics of state-selected OCS and benzene in laser fields

A Thesis submitted to the University of Tokyo
for the degree of Doctor of Science

Ryuji Itakura

Department of Chemistry,
School of Science,
The University of Tokyo

January, 2001

Acknowledgements

Above all, I would like to express my sincerest gratitude to Professor Kaoru Yamanouchi who has supervised me and has provided the ideal research environment for me throughout the course of this work. I had learned a lot from him. Particularly, his sincere attitude toward science made my thinking on research earnest.

I would also like to acknowledge Professor Akiyoshi Hishikawa for his kind support and valuable advice during the entire course of this work. Almost of my experimental technique and knowledge has been obtained from his detailed instruction and guidance.

I am grateful to Professor Geerd H. F. Diercksen (Max-Planck-Institut für Astrophysik), and Professor Koichi Yamashita (Graduate School of Engineering, the University of Tokyo) for their valuable discussion and comments about the *ab initio* calculation of the potential energy surface of OCS.

I would like to thank Ms. Jun Watanabe for helping me during the experiment using a tandem time-of-flight mass spectrometer, and Dr. Atsushi Iwasaki for building the electronic digital circuit for synchronizing the fs laser and the excimer laser. The study on the mass-selected benzene cations in intense laser fields could not be accomplished without their support.

I am grateful to Professor Shilin Liu (the University of Science and Technology of China), Dr. Mitsuhiko Kono, Dr. Kennosuke Hoshina, Dr. Atsushi Iwamae, Dr. Yuji Fukuda, Dr. Kyoko Ohde, and Dr. Tokuei Sako, for their valuable advice, discussion,

and encouragement.

Furthermore, I would like to express thanks to all the members of Professor Yamanouchi's group for their heart-warming encouragement and help.

I acknowledge the Japan Society for the Promotion of Science for the research fellowship from April 1998 to December 2000.

Finally, I appreciate my parents who understood my academic research life and have supported me during the entire course of this work.

Tokyo,

January 2001 Ryuji Itakura

The present thesis is based on the contents of the following two papers:

1. "Resonance-state selective photodissociation of OCS ($2^1\Sigma^+$): Rotational and vibrational distributions of CO fragments"
   Ryuji Itakura, Akiyoshi Hishikawa, and Kaoru Yamanouchi
   J. Chem. Phys. **113**, (2000) 6598.

2. "Ionization and fragmentation dynamics of benzene in intense laser fields by tandem mass spectroscopy"
   Ryuji Itakura, Jun Watanabe, Akiyoshi Hishikawa, and Kaoru Yamanouchi
   J. Chem. Phys. **114**, (2001) 5598.

The following paper is listed as a reference, and is not included in the thesis:

3. "Femtosecond transition-state dynamics of dissociating OCS on the excited $^1\Sigma^+$ potential energy surface"
   Akiyoshi Hishikawa, Kyoko Ohde, Ryuji Itakura, Shilin Liu, Kaoru Yamanouchi, and Koichi Yamashita
   J. Phys. Chem. A **101**, (1997) 694.

Contents

Chapter 3

Chapter 4

Chapter 5

Chapter 1

General Introduction

The research field of the unimolecular reaction has expanded largely by the recent development of the laser technology. The major issues for researchers in this field are to understand the chemical reaction dynamics and to control the chemical reaction quantum-mechanically.

From the extensive theoretical and experimental investigation for molecular states which have discrete or quasi-discrete eigenvalues, a variety of the characteristic dynamics of highly excited molecules such as intramolecular vibrational energy redistribution (IVR), predissociation dynamics have been clarified. A number of non-linear spectroscopic techniques in the visible (VIS) and ultraviolet (UV) wavelength region have significantly enlarged the research areas.[1,2]

On the other hand, quantum-controls of unimolecular reaction by the coherence of the laser are proposed such as a pump-dump scheme where the wavepacket is controlled via optical transitions between the electronic states by short laser pulses[3,4] and a phase-control scheme where the interference between the continuum wavefunctions leading to different reaction channels are controlled by the relative phase between two optical transition pathways.[5] However, until now, these control schemes could not always be applicable to every molecules. Indeed, IVR processes, which are dependent on the

molecular potential energy surface (PES), are major obstacles for controlling chemical reaction dynamics.

A major theme of this thesis is to understand laser-induced ultrafast molecular processes on a "state-to-state" level. First, the energy region of molecular states was raised to the vacuum ultraviolet (VUV) region, where most of ultrafast dissociative states are located. An ultrafast photodissociation process occurring on the same time scale as a vibrational period is an important research subject for understanding fundamentals of the intramolecular energy partitioning mechanism which governs reaction dynamics.[6]

Then, the intensity of the laser was increased over the perturbative regime. When magnitude of laser fields become comparable to the Coulomb fields within a molecule, such photon fields can not be treated in a perturbative manner and must be included into the Hamiltonian as one of the main interaction terms. In such intense laser fields, PES's of a molecule are distorted and a new class of PES's is formed.[7,8]

In Section I, an overview of ultrafast photodissociation is described, and in Section II, a characteristic aspect of molecular dynamics on the PES deformed by intense laser fields is briefly summarized.

I. Ultrafast photodissociation dynamics

The continuum states via which ultrafast dissociation occurs need to be treated in a different way from the discrete states. In this section, in order to give an insight into the dissociation dynamics, dissociation of triatomic molecules is treated. In most case, the Jacobi coordinate system drawn in Fig. 1 is adopted to treat the dissociation of triatomic molecules, ABC $\rightarrow$ A + BC.

First, the dynamics in which only two coordinates are taken into account, i.e. the dissociative coordinate, R, and the vibrational coordinate, r, will be described. It has been known that an absorption spectrum of dissociating molecules showing broadened peaks contains information of the dissociation dynamics near the Franck-Condon (FC) region.[9,10] In such cases, an absorption spectrum in the energy domain can be transformed into an autocorrelation function in the time domain by the Fourier transformation. On the basis of the autocorrelation function exhibiting recurrences, the dissociation dynamics on a dissociative PES have been discussed in terms of motion of the wavepacket. For example, the dissociative nuclear motion on the dissociative PES of the X-NO type molecules was theoretically studied as described in Fig. 2.[6,11]

However, the absorption spectrum can provide only limited information of the dynamics in the FC region. In order to understand the entire dissociation process, it is necessary to investigate the dynamics after the wavepacket leaves the FC region leading to the fragments.

In the two dimensional case, the molecular Hamiltonian can be expressed as

$$H(\mathrm{R},\mathrm{r}) = -\frac{\hbar^2}{2\mathrm{M}}\frac{\partial^2}{\partial \mathrm{R}^2} - \frac{\hbar^2}{2\mu}\frac{\partial^2}{\partial \mathrm{r}^2} + V(\mathrm{R},\mathrm{r}), \qquad (1)$$

where the reduced masses, M and μ are defined as

$$\mathrm{M} = \frac{\mathrm{m_A}(m_B + m_C)}{\mathrm{m_A} + \mathrm{m_B} + \mathrm{m_C}}, \quad \mu = \frac{\mathrm{m_B m_C}}{(\mathrm{m_B} + \mathrm{m_C})}.$$

Therefore, the time-independent Schrödinger equation is represented as

$$\left[-\frac{\hbar^2}{2M}\frac{\partial^2}{\partial R^2}-\frac{\hbar^2}{2\mu}\frac{\partial^2}{\partial r^2}+V(R,r)-E\right]\Psi(R,r,E)=0\ . \qquad (2)$$

In order to relate the resonant quasi-bound vibration near the Franck-Condon region to the vibration of the diatomic fragment, the vibrational adiabatic basis is useful. The wavefunction, $\Psi(R, r, E)$, on the dissociative PES can be expanded with the adiabatic vibrational wavefunctions, $\varphi_n(r;R)$, and the dissociative wavefunctions, $\chi_n(R,E,n)$ as

$$\Psi(R,r,E)=\sum_n \Psi(R,r,E,n)=\sum_n\sum_{n'}\chi_{n'}(R,E,n)\varphi_{n'}(r;R), \qquad (3)$$

where $\Psi(R,r,E,n)$ is the continuum wavefunction leading to a diatomic fragment with the vibrational quantum number, n. The adiabatic vibrational wavefunction, $\varphi_n(r;R)$, which parametrically depends on the dissociation coordinate, R, fulfills the following equation,

$$\left[-\frac{\hbar^2}{2\mu}\frac{\partial^2}{\partial r^2}+V(R,r)-\varepsilon_n(R)\right]\varphi_n(r;R)=0\ , \qquad (4)$$

where $\varepsilon_n(R)$ stands for a vibrationally adiabatic potential energy curve. In the limit of $R \rightarrow \infty$, $\varphi_n(r;R)$ and $\varepsilon_n(R)$ become the vibrational wavefunction and eigenvalue of the free diatomic fragment, BC, respectively.

From the orthogonal condition of the adiabatic vibrational basis set, $\varphi_n(r;R)$, the Schrödinger equation represented by eq. (2) can be reduced to coupled equations,

$$\left[\frac{d^2}{d\,R^2} + k_{n'}(R)^2 - U_{n'n'}(R)\right] \chi_{n'}(R,E,n)$$

$$= \sum_{n'' \neq n'} \left[U_{n'n''}(R) + Q_{n'n''}(R)\frac{d}{dR}\right] \chi_{n''}(R,E,n), \qquad (5)$$

where

$$k_n(R) = \{\, 2M\,[\,E - \varepsilon_n(R)\,]\,/\hbar^2\}^{1/2} \qquad (6)$$

and the coupling matrix elements for the dissociative kinetic energy operator are defined as

$$U_{n'n''}(R) = -\left\langle \varphi_{n'}(r;R) \left| \frac{\partial^2}{\partial R^2} \right| \varphi_{n''}(r;R) \right\rangle \qquad (7)$$

and

$$Q_{n'n''}(R) = -2\left\langle \varphi_{n'}(r;R) \left| \frac{\partial}{\partial R} \right| \varphi_{n''}(r;R) \right\rangle. \qquad (8)$$

The diagonal elements of $Q_{n'n''}$ are exactly zero from the orthogonal condition, i.e.

$$\left\langle \varphi_{n'}(r;R) \left| \frac{\partial}{\partial R} \right| \varphi_{n'}(r;R) \right\rangle = \frac{1}{2}\frac{\partial}{\partial R}\left\langle \varphi_{n'}(r;R) \middle| \varphi_n(r;R) \right\rangle = 0. \qquad (9)$$

If the motion expressed with the coordinate, r, is much faster than the dissociative motion, the adiabatic vibrational wavefunctions, $\varphi_n(r;R)$, would not be influenced by the change in the dissociation coordinate, R. Therefore, the coupling matrix elements of the dissociative kinetic energy operator become small and the vibrational adiabaticity is

preserved. Although the dissociative excited states of the X-NO type molecules in the VIS and UV region are described relatively well by the vibrational adiabatic picture, it has not been understood how the adiabaticity is kept or broken in general.

In the Jacobi coordinate system, the rotational coordinate, γ, can be regarded as the rotational angle of the free diatomic rotor in the limit of $R \rightarrow \infty$, while it represents the bending coordinate of the parent molecule around the FC region. In the rigid rotor approximation, the vibrational coordinate, r, is fixed and the Hamiltonian can be represented as

$$H(R, \gamma) = -\frac{\hbar^2}{2M}\frac{1}{R}\frac{\partial^2}{\partial R^2}R + \frac{\boldsymbol{L}^2}{2MR^2} + \frac{\boldsymbol{j}^2}{2\mu r^2} + V(R, \gamma), \qquad (10)$$

where $\boldsymbol{L}$ and $\boldsymbol{j}$ are the translational orbital angular momentum and the rotational angular momentum of the diatomic fragment. Under the jet-cooled condition, it can be approximated that the total angular momentum, $\boldsymbol{J}$, of the sample molecule is equal to zero. For simplicity, $\boldsymbol{J} = 0$ is assumed. If $\boldsymbol{J} = 0$, $\boldsymbol{L} = -\boldsymbol{j}$ is fulfilled from $\boldsymbol{J} = \boldsymbol{L} + \boldsymbol{j}$ and the dissociation occurs on a fixed molecular plane to which $\boldsymbol{L}$ and $\boldsymbol{j}$ are perpendicular. Therefore, the Schrödinger equation is described as

$$\left[-\frac{\hbar^2}{2M}\frac{1}{R}\frac{\partial^2}{\partial R^2}R + \left(\frac{1}{2MR^2} + \frac{1}{2\mu r^2}\right)\boldsymbol{j}^2 + V(R, \gamma)\right]\Psi(R, \gamma, E) = E\,\Psi(R, \gamma, E), \qquad (11)$$

where the wavefunction, $\Psi(R, \gamma, E)$, at the eigenenergy, E, can be expanded as

$$\Psi(R, \gamma, E) = \sum_j \Psi(R, \gamma, E, j) = \frac{1}{R}\sum_j \sum_{j'} \chi_{j'}(R, E, j)\, Y_{j'0}(\gamma, \psi = 0). \qquad (12)$$

In eq. (12), $\Psi(R, \gamma, E, j)$ is a continuum wavefunction leading to the diatomic fragment with the rotational quantum number, j, and $Y_{j'\Omega}(\gamma, \psi)$ is the spherical harmonics representing the rotation of the diatomic fragment. If the quantization axis of ***j*** lies on the molecular plane, the projection quantum number, Ω, and the azimuth angle, ψ, are fixed to be Ω = 0 and ψ = 0, respectively. From the expansion of $\Psi(R, \gamma, E, j)$ in eq. (12) and the orthogonality of $Y_{j'\Omega}(\gamma, \psi)$, the Schrödinger equation of eq. (11) can be represented by the coupled equations,

$$\left[\frac{d^2}{d R^2} + k_{j'}^2 - \frac{j'(j'+1)}{R^2}\right] \chi_{j'}(R, E, j) = \frac{2M}{\hbar^2} \sum_{j''} V_{j'j''}(R)\, \chi_{j''}(R, E, j), \qquad (13)$$

where $k_{j'}$ is represented as

$$k_{j'} = [\, 2M \{ E - B_{rot}\, j\,(j+1) \}/\hbar^2 \,]^{1/2} \qquad (14)$$

using the rotational constant of the diatomic fragment, B_{rot}, and the coupling matrix element, $V_{j'j''}$, is described as

$$\begin{aligned} V_{j'j''} &= \left\langle Y_{j'0} \middle| V(R, \gamma) \middle| Y_{j''0} \right\rangle \\ &= \int_0^{2\pi} d\psi \int_0^{\pi} d\gamma \sin\gamma\, Y_{j'0}^{*}(\gamma, 0)\, V(R, \gamma)\, Y_{j''0}(\gamma, 0) \end{aligned} . \qquad (15)$$

The two equations, eq. (12) and eq. (13), respectively represent how the bending wavefunction on the dissociative state is expanded by the spherical harmonics of the diatomic fragment and how the dissociation channels leading to the different rotational state of the fragment are coupled to each other. Several models to explain the

rotational state distribution of fragments have been proposed by taking account of the relationship between the bending motion of the parent molecule and the rotational motion of the fragment.[6]

Although the vibration and rotation of the fragments have been treated separately in the above description, these two motions can not be separated completely from each other. Therefore, the vibrational coordinate, r, and the rotational coordinate, γ, need to be treated simultaneously. The three-dimensional formulation without the assumption of $\boldsymbol{J} = 0$ was explicitly derived by Balint-Kurti and Shapiro.[12] In their treatment, the continuum wavefunction is expanded with the vibrational and rotational eigenfunctions of a free diatomic fragment. The dissociation channels leading to the different ro-vibrational states are coupled to each other via the coupling matrix including the potential term, $V(R, r, \gamma)$.

Experimentally, there have been difficulties in accessing to dissociative continuum states because such dissociative states is in most case located in the vacuum ultraviolet (VUV) wavelength region. In addition, another VUV laser light is often required to probe the fragment atom or diatomic molecules by the laser spectroscopic method such as laser induced fluorescence and resonantly enhanced multiphoton ionization. Therefore, in most of the studies in the VUV region, absorption and fluorescence cross-sections of parent molecules have been measured or product state distributions of fragments produced by the photolysis at a fixed wavelength such as 193 nm and 157 nm have been measured.

A lot of investigations have been performed using a VUV excimer laser with the fixed wavelengths as a photolysis light source and a tunable VUV laser as a probe laser to probe product state distributions of the fragments. At the excitation energy

corresponding to the fixed wavelengths of the excimer lasers, molecules do not always have its state that carries strong quasi-bound characters. However, almost no experimental effort has been made for any VUV wavelength range other than those fixed wavelengths because it requires laborious technique to generate the tunable VUV laser light. It is obvious that a "state-to-state" study is essential to know how the dissociation channels are coupled to each other and how the resonant state in the FC region is connected to the product states.

In this thesis, the ultrafast photodissociation of OCS($2^1\Sigma^+$) is investigated. The $2^1\Sigma^+$ state of OCS is known to exhibit the characteristic vibrational resonances in its absorption and excitation spectra, and to be well isolated from other electronic states.[13-15] Furthermore, the non-adiabatic coupling to other electronic states is considered to be very weak because the dissociation via the $2^1\Sigma^+$ state exclusively produces CO($X^1\Sigma^+$) and S(^1S), which are correlated to the electronic configuration of the $2^1\Sigma^+$ state. Therefore, the $2^1\Sigma^+$ state of OCS provides an ideal opportunity to investigate an ultrafast dissociation dynamics.

In Chapter 2, using two sets of tunable VUV laser generated by the four wave mixing technique OCS is excited to the respective resonant levels in the $2^1\Sigma^+$ state located in the VUV region and electronic, vibrational, and rotational state distribution of the fragments are proposed. As a result of this pump-probe investigation, the existence of the complex mixing among the dissociation channels is identified. In Chapter 3, the excitation spectrum was measured by the two-photon excitation scheme in the entire energy region of the $2^1\Sigma^+$-$1^1\Sigma^+$ band, and the dissociation dynamics around the FC region were investigated on the basis of the weak resonance feature identified in the spectrum.

II. Molecular dynamics in intense laser fields

By using the short pulsed laser generated by the chirped-pulse amplification, electric laser fields as intense as the Coulomb fields within a molecules can be generated. Recently, a research field of molecular science is being widen by such intense lasers.[7] In intense laser fields, dynamics of molecules can not be treated in a perturbative manner. Nuclear motion of molecules in intense laser fields has often been described by the dressed-state picture[16] in which the PES of a n-photon dressed state is energetically shifted down-word by the energy corresponding with n photons. The crossings among the PES's having the same symmetry, are avoided as the laser fields intensity increases. In the case of H_2^+,[7,8,17-19] which is the simplest molecule having only one electron, the nuclear dynamics has been explained clearly by taking account of only the lowest two potential energy curves of the $1s\sigma_g$ and $2p\sigma_u$ states. As a result of the coupling among the potential curves in intense laser fields, new light-dressed potential curves are formed leading to the bond softening[19] and the vibrational trapping,[20] as drawn in Fig. 3.

Light-deformed PES could be utilized for controlling chemical reaction by light fields. Recently, it was reported that the light-induced potential curve of H_2^+ was manipulated by chirping the intensity of a laser pulse.[21]

It was recently found that the structure of triatomic molecules such as H_2O,[22-24] CO_2,[25,26] and NO_2,[27] in intense laser fields are deformed within a temporal duration of a femtosecond laser pulse; i.e. molecular skeletal geometry changes from linear to bent, or vice versa. Such geometrical deformation has been attributed to the light-induced PES's caused by coupling between the PES with linear geometry and that with bent geometry, as shown in Fig. 4.

However, for polyatomic molecules with many electrons, their dynamics in intense laser fields is very complex because a number of electronic states could be involved and more than one nuclear degree of freedom need to be taken into accounts. Furthermore, molecules could be ionized into a multiply ionized state. Therefore, it would be difficult to identify specific electronic states of a certain charge state among a large number of candidates, which are most responsible for forming the dressed PES's governing the nuclear dynamics.

In the previous experiments, in most case neutral molecules are exposed to intense laser pulses, and the fragment atomic ions produced through the Coulomb explosion of the multiply charged parent molecules are detected. Therefore, the information of the intermediate processes between the initial neutral and the final multiply charged ions just before the Coulomb explosion could not be obtained directly.

In Chapter 4, in order to specify the electronic states forming the fate-determining dressed PES, a tandem type time-of-flight mass spectrometer was introduced for the preparation of the molecular ions having a selected charge number. By the selection of the ion charge in the first time-of-flight stage, the number of candidates responsible for the dynamics in intense laser fields could be reduced significantly. On the basis of the experiments for both the neutral and singly charged benzene molecules, it is found that the two specific electronic states in benzene cation are strongly coupled in intense laser fields when the laser wavelength is 400 nm, and are responsible for the fragmentation dynamics.

References

[1] W. Demtroder, *Laser spectroscopy* (Springer -Verlag Berline Heidelberg, 1996).

[2] H. L. Dai and R. W. Field (Eds.), *Molecular dynamics and spectroscopy* (World Scientific, 1995).

[3] D. J. Tanor and S. A. Rice, J. Chem. Phys. **83**, 5013 (1985).

[4] D. J. Tanor, R. Kosloff, and S. A. Rice, J. Chem. Phys. **85**, 5805 (1986).

[5] P. Brumer and M. Shapiro, Acc. Chem. Res. **22**, 407 (1989).

[6] R. Schinke, *Photodissociation dynamics* (Cambridge University Press, New York, 1993).

[7] A. D. Bandrauk, *Molecules in laser fields* (Marcel Dekker, New York, 1993).

[8] B. Sheehy and L. F. Dimauro, Ann. Rev. Phys. Chem. **47**, 463 (1996).

[9] R. T. Pack, J. Chem. Phys. **65**, 4765 (1976).

[10] E. J. Heller, Acc. Chem. Res. **14**, 368 (1981).

[11] J. R. Huber, and R. Schinke, J. Phys. Chem. **97**, 3463 (1993).

[12] G. G. Balint-Kurti, and M. Shapiro, Chem. Phys. **61**, 137 (1981).

[13] A. Hishikawa, K. Ohde, R. Itakura, S. Liu, K. Yamanouchi, and K. Yamashita, J. Phys. Chem. A **101**, 694 (1997).

[14] M. I. McCarthy, and V. Vaida, J. Phys. Chem. **92**, 5875 (1988).

[15] J. W. Rabalais, J. M. McDonald, V. Scherr, and S. P. McGlynn, Chem. Rev. **71**, 73 (1971).

[16] C. Cohen-Tannoudji, J. Dupont-Roc, and G. Grynberg, *Atom-Photon Interactions: Basic Processes and Applications* (Wiley, New York, 1998).

[17] A. Giusti-Suzor, F. H. Mies, L. F. DiMauro, E. Charron, and B. Yang, J. Phys. B **28**, 1995 (1995).

[18] A. Zavriyev, P. H. Bucksbaum, H. G. Muller, and D. W. Schmacher, Phys. Rev. A **42**, 5500 (1990).

[19] P. H. Bucksbaum, A. Zavriyev, H. G. Muller, and D. W. Schumacher, Phys. Rev. Lett. **64**, 1883 (1990).

[20] A. Giusti-Suzor and F. H. Mies, Phys. Rev. Lett. **68**, 3869 (1992).

[21] L. J. Frasinski, J. H. Posthumus, J. Plumridge, and K. Codling, Phys. Rev. Lett. **83**, 3625 (1999).

[22] H. Rottke, C. Trump, and W. Sandner, J. Phys. B **31**, 1083 (1998).

[23] J. H. Sanderson, A. El-Zein, W. A. Bryan, W. R. Newell, A. J. Langley, and P. F. Taday, Phys. Rev. A **59**, R2567 (1999).

[24] S.Liu, A.Hishikawa, A.Iwamae, and K.Yamanouchi, in *Advances in Multiphoton Processes and Spectroscopy,*, edited by Y. Fujimura and R. J. Gordon (World Scientific, Singapore, 2001), Vol. 13, p. 182.

[25] A. Hishikawa, A. Iwamae, and K. Yamanouchi, Phys. Rev. Lett. **83**, 1127 (1999).

[26] W. A. Bryan, J. H. Sanderson, A. El-Zein, W. R. Newell, and A. J. Langley, J. Phys. B **33**, 745 (2000).

[27] A. Hishikawa, A. Iwamae, and K. Yamanouchi, J. Chem. Phys. **111**, 8871 (1999).

Figure Captions

Fig. 1. The definition of the Jacobi coordinate for the dissociation, ABC $\rightarrow$ A + BC. R is the distance between the atomic fragment, A, and the center of mass of the diatomic fragment, BC, r is the nuclear distance of the diatomic fragment, BC, and γ is the angle of the rotation of the diatomic fragment, BC. The points, S and s are the centers of mass of the parent molecule, ABC, and the diatomic fragment, BC, respectively.

Fig. 2. The relationship among the absorption spectra (a), the autocorrelation functions (b), and the *ab initio* PES's (c) in the case of the X-NO (X = F, Cl, and CH_3) type molecules (Ref. 11). The dots in the PES's indicate the Franck-Condon point.

Fig. 3. The light-dressed potential energy curves for the $1s\sigma_g$ and $2p\sigma_u$ states of H_2^+ (Ref. 8). The "n" stands for the number of coupled photons. The potential curves originating from the $1s\sigma_g$ and $2p\sigma_u$ are represented by "g" and "u", respectively. The total symmetry of the potential curves coupled with photons is *gerade* for all curves in this figure.

Fig. 4. A schematic light-induced potential energy curves of a triatomic molecule along the bending coordinate. A light-dressed state is represented by $|\, a, n\hbar\nu\rangle$ as a mixture of the field free molecular state, $|\, a\rangle$, and the n-photon field.

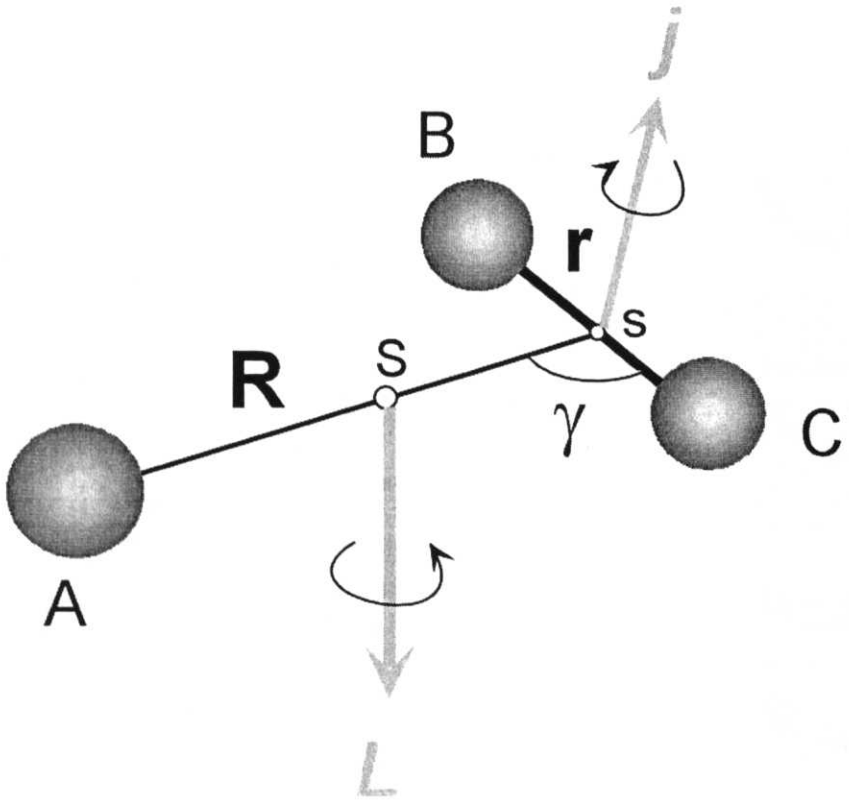

Fig. 1

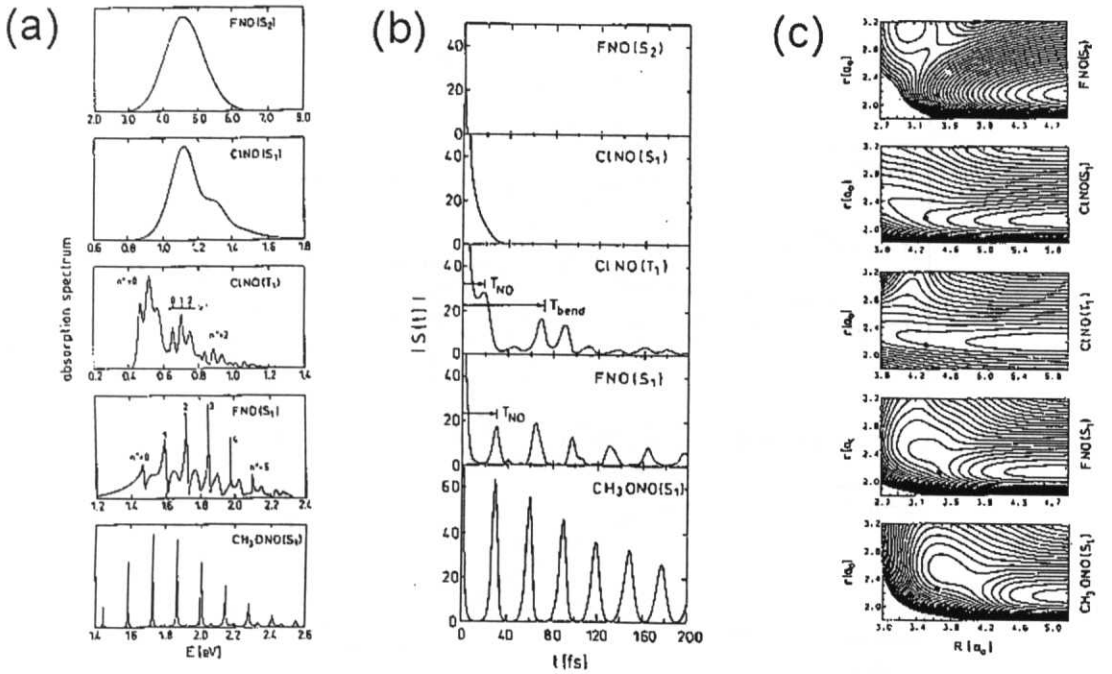
(a)
(b)
(c)
absorption spectrum
E [eV]
|S(t)|
t [fs]
FNO(S2)
ClNO(S1)
ClNO(T1)
FNO(S1)
CH3ONO(S1)
TNO
Tbend

Fig. 2

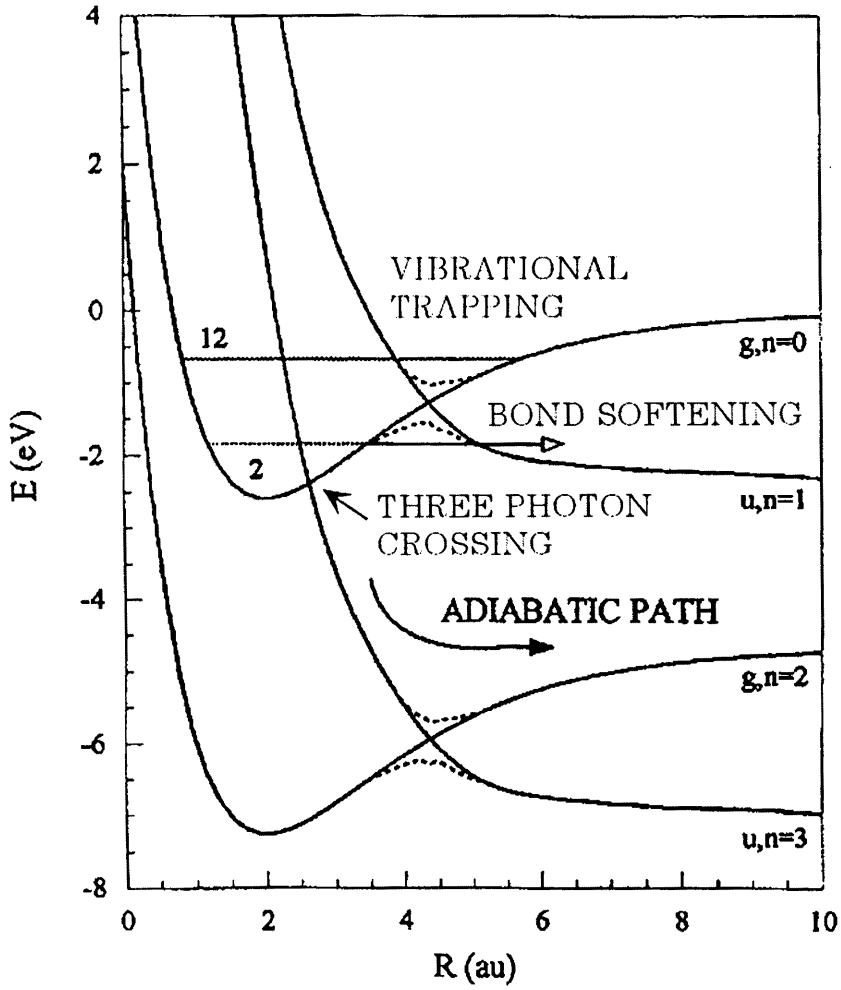
VIBRATIONAL
TRAPPING
12
g,n=0
BOND SOFTENING
2
THREE PHOTON
CROSSING
u,n=1
ADIABATIC PATH
g,n=2
u,n=3
E (eV)
R (au)
4
2
0
-2
-4
-6
-8
0
2
4
6
8
10

Fig. 3

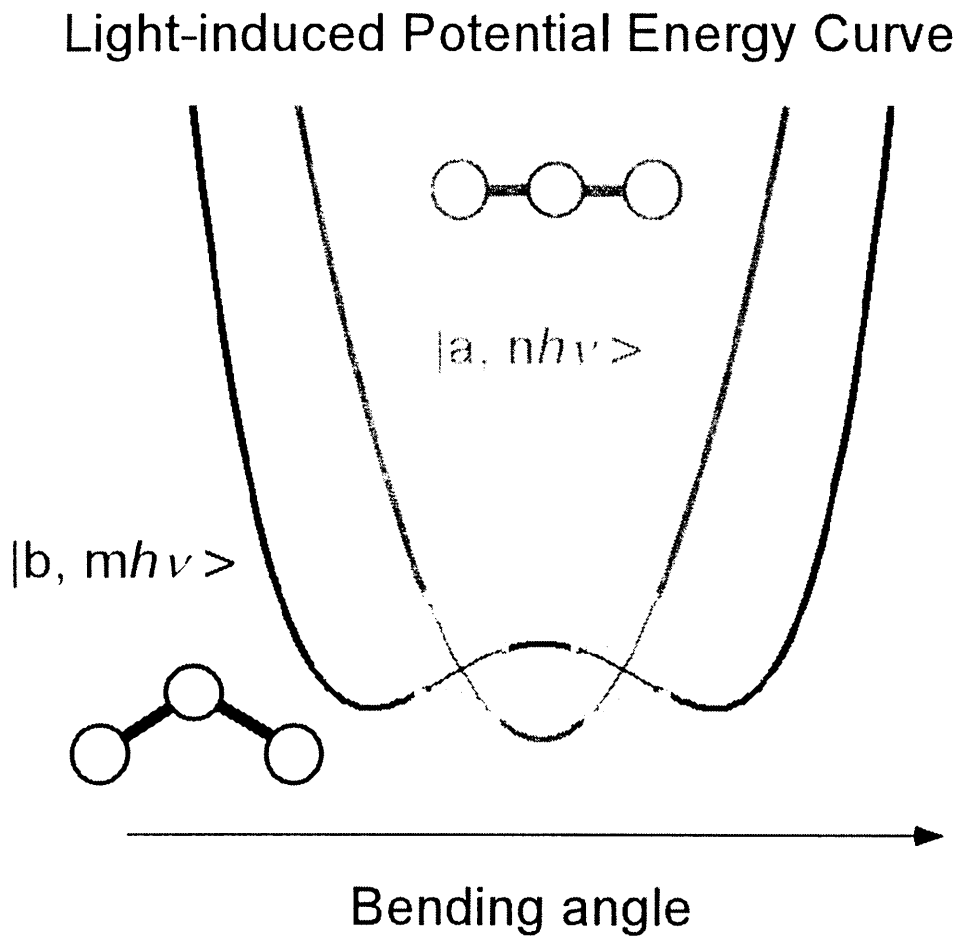
Light-induced Potential Energy Curve
|a, nhν>
|b, mhν>
Bending angle

Fig. 4

Chapter 2

Resonance-state selective photodissociation of OCS ($2^1\Sigma^+$): Rotational and vibrational distributions of CO fragments

Abstract

The rotational and vibrational state distributions of the CO fragments produced through the photodissociation of OCS in the vacuum ultraviolet (VUV) region (150 - 155 nm), OCS ($2^1\Sigma^+$) $\rightarrow$ CO ($X^1\Sigma^+$) + S (^1S), are derived for the three lowest quasi-bound vibrational resonances ($v^* = 0 - 2$) in the $2^1\Sigma^+$ state. The rotational state distributions of the CO fragments in the $v_{CO} = 0$ and 1 vibrational states are determined respectively by the analysis of the rotational structures in the laser-induced fluorescence (LIF) spectra of the $A^1\Pi$-$X^1\Sigma^+$ (0, 0) and (1, 1) transitions of CO. The rotational temperatures of CO in the $v_{CO} = 0$ state are low (~ 100 K) for all the three resonances, while those in the $v_{CO} = 1$ state are substantially higher, i.e., 2210, 940, and 810 K for $v^* = 0$, 1, and 2, respectively. The vibrational state distributions of CO are derived from the Doppler spectroscopy of the counterpart S (^1S) fragments. From the analysis of the observed Doppler profiles, it is found for all the three lowest vibrational resonances of OCS that the vibrational distributions are represented well by the Boltzmann-type distribution with a vibrational temperature of around 7000 K. On the basis of these new findings, the energy partitioning in the photodissociation process through these three vibrational resonances in the $2^1\Sigma^+$ state is discussed.

I. Introduction

When molecules are irradiated by light in the vacuum ultraviolet (VUV) wavelength region, they undergo photodissociation in most cases. In the case of polyatomic molecules, which have more than or equal to three degrees of vibrational freedom, the nuclear motion along the direction perpendicular to the dissociation coordinate are often bound. Therefore, even in the direct dissociation, they could form quasi-bound vibrational resonances appearing as structured profiles with broadened peaks in an absorption spectrum, from which the nuclear motion near the Franck-Condon (FC) region could be extracted.[1,2] However, until recently, little efforts have been made to interpret such rich spectral features of polyatomic molecules in the VUV region. This may be partly due to the overlap of the transitions from the rotationally and vibrationally excited states, which broadens and blurs originally characteristic spectral structures.

In our recent studies,[3-7] the photodissociation process of OCS, OCS ($2^1\Sigma^+$) $\rightarrow$ CO ($X\ ^1\Sigma^+$) + S (^1S), in the 140-160 nm wavelength region was studied by measuring the excitation spectrum called the photofragment excitation (PHOFEX) spectrum under jet-cooled conditions by monitoring the S (^1S) fragments employing a tunable VUV light generated by the four-wave difference frequency mixing technique. As shown in Fig.1, the PHOFEX spectra of the entire region of the $2^1\Sigma^+$ - $1^1\Sigma^+$ band of OCS exhibited five main peaks. These peaks were assigned to the transitions to the resonant vibrational states with respective quantum numbers, $v^* = 0 - 4$, representing the quasi-bound vibrational motion near the FC region on the potential energy surface (PES) of the $2^1\Sigma^+$ state which is mostly repulsive along the dissociation coordinate. This quasi-bound vibration was interpreted as the in-phase CO and CS stretching mode perpendicular to

the dissociation coordinate. On the basis of the PHOFEX spectrum exhibiting characteristic asymmetrical peak profiles with different peak widths, the ultrafast nuclear motion on the $2^1\Sigma^+$ PES near its FC region was discussed.

Even though we were able to understand the ultrafast nuclear dynamics near the FC region from the absorption features, there still remains a question how the energy imposed on molecules by the photoabsorption is partitioned into the fragments in the dissociation process. When considering that the five main peaks, which form the progression of the vibrational resonances, exhibit different characteristic asymmetric profiles, it would be interesting to investigate how the energy flow is influenced by the character of the initially prepared resonant states.

In order to understand the energy partitioning dynamics, it becomes necessary to probe the rotational and vibrational distributions of the CO fragments. Since the first dipole-allowed excited state, $A^1\Pi$, of CO is located in the energy range of ~ 65000 cm^{-1}, we need to introduce another tunable VUV light source to probe the fragments while tuning the first VUV light source to selectively excite the vibrational resonance peaks in the $2^1\Sigma^+$ - $1^1\Sigma^+$ transition of OCS.

In the present study, we probe the rotational distribution of the CO fragments by measuring the laser-induced fluorescence (LIF) spectrum of the $A^1\Pi$ - $X^1\Sigma^+$ bands of CO using the second tunable VUV light source, and probe the S (^{1}S) fragments by tuning the UV light near the $^3D^\circ$ – ^{1}S transition of the sulfur atoms to derive the vibrational distribution of the CO fragments through the measurements of the Doppler profiles. On the basis of the product state distributions, we discuss the mechanism which governs the later stage of the photodissociation of OCS after it leaves the FC region of the $2^1\Sigma^+$ surface.

In spite of the long history of the pump-probe type investigation of molecular dynamics using the laser light sources, as far as we know, the present study reported for the first time the pump-probe experiments in which two sets of tunable VUV laser light source generated by a two-photon resonant four-wave mixing scheme are employed. It is true that two or three photon LIF or resonantly enhanced multiphoton ionization (REMPI) techniques could be used to probe photofragments, but a non-linearity of the process with respect to the laser intensities as well as complex rotational-transition selection rules for molecular fragments causing the overlapping rotational structure tends to introduce a large ambiguity in the product state distribution of the fragments. Therefore, the present success of the one-photon probe followed by one-photon excitation in the VUV region is encouraging in the sense that the number of the research targets of photodissociation spectroscopy in the VUV region could be largely increased.

II. Experiment

The schematic diagram of the experimental setup is shown in Fig.2. A sample gas (OCS (10%) / Ar) was expanded into a vacuum chamber from a pulsed valve (10 Hz) with the 0.8 mm orifice diameter with the stagnation pressure of 1.5 atm. When the pulsed valve was operated, the pressure in the chamber was about 1.5×10^{-4} Torr. The rotational temperature of OCS in the expanded free jet was estimated to be about 6 K, which was obtained for CO contained in OCS sample (Matheson, 97.5% purity) as the trace amount of impurity from the measurements of the VUV-LIF spectra of the $A^1\Pi$ - $X^1\Sigma^+$ (0, 0) transitions.

A tunable VUV laser light was generated by the two-photon resonant four-wave difference frequency mixing in the Xe gas.[8] For the VUV light for the photolysis of

OCS, the output beams of the two dye lasers (Lambda Physik FL3002) simultaneously pumped by a XeCl excimer laser (Lambda Physik LPX 205i) were used. The frequency doubled output (ω_1) of one dye laser was tuned to the two-photon resonant frequency of the Xe $6p[1/2]_0$ (80119.474 cm^{-1}), and then, the output of the other dye laser (ω_2: 13700 – 15385 cm^{-1}) was tuned to generate the VUV frequencies ($2\omega_1-\omega_2$) corresponding to the three lowest resonant peaks ($v^* = 0 - 2$) in the PHOFEX spectrum of the $2^1\Sigma^+ - 1^1\Sigma^+$ band of OCS in Fig. 1, appearing at 64745, 65595, and 66380 cm^{-1}.[7] The two light beams with the frequencies of ω_1 and ω_2 were overlapped co-axially by a dichroic mirror and focused into a stainless steel cell containing the Xe gas (15 - 30 Torr) by a achromatic lens (f = 300 mm). The VUV laser light generated in the Xe cell was collimated or mildly focused by an LiF lens (f = 120 mm) and separated from the ω_1 and ω_2 light beams by an LiF prism placed in the separator chamber connected to the Xe cell. Then, only the generated VUV light beam was introduced into the main chamber and it crossed the free jet of the sample gas 12 mm downstream from the nozzle orifice at an angle of 45 degrees.

In order to probe the vibrational and rotational states of the CO fragments, another tunable VUV laser light was generated by using a dye laser (Lambda Physik Scanmate) and a OPO laser (Lambda Physik Scanmate OPPO) simultaneously pumped by third harmonics of the Nd:YAG laser with the injection seeding (Coherent Infinity 40-100). The same $2\omega_1-\omega_2$ scheme was adopted to generate the second VUV laser to probe the CO fragments as in the generation of the photolysis VUV laser light. The bandwidth of the VUV laser light for both the photolysis and the probe was 0.45 cm^{-1} in FWHM.

The probe VUV laser light was introduced into the chamber so that it hits the crossing point of the molecular beam and the photolysis VUV laser beam at an angle of

45 degrees with the molecular beam and at right angles with the photolysis VUV laser beam. The direction of the polarization of the photolysis VUV laser beam was set to be parallel with that of the probe VUV laser beams. The fluorescence was monitored by a solar-blind photomultiplier (Hamamatsu R1259) placed beneath the triple crossing point through a light-collection optics composed of a pair of LiF lenses (f = 30 mm). By scanning the wavelength of the probe VUV laser, the LIF spectra of the $A^1\Pi$ - $X^1\Sigma^+$ (0, 0) (64640 – 64800 cm^{-1}) and (1, 1) (63900 – 64150 cm^{-1}) bands of CO were measured.

In order to probe the S (^1S) fragments produced from the photolysis of OCS by the VUV light, the output of the dye laser (Lambda Physik Scanmate) pumped by third harmonics of a Nd:YAG laser with injection seeding (Coherent Infinity 40-100) was frequency doubled in a BBO crystal, and tuned around the frequency of the $^3D^\circ$ – ^1S transition (45636 cm^{-1}) of the S atoms. The probe UV laser beam was introduced into the main chamber so that it crosses with the photolysis VUV laser beam and the free jet in the same manner as the probe VUV laser for monitoring the CO fragments.

By monitoring the atomic fluorescence at 148 nm emitted from the $^3D^\circ$ state to the ^3P state of the S atoms, the frequency of the probe laser was scanned to measure the Doppler profile of the S (^1S) fragments. The intracavity etalon was used for the probe laser to make the bandwidth (FWHM) as narrow as 0.08 cm^{-1}. In order to set the polarization of the photolysis VUV laser to be parallel with the direction of the propagation of the probe UV laser, the direction of the polarization of the ω_2 light was rotated by 90 degrees by using a pair of Fresnel rhombs. For achieving the high purity of the linear polarization of the VUV light, the light beam with the frequency of ω_2 was transmitted though a Glan-laser polarizer after it passes through the pair of Fresnel

rhombs.

For the purification of the OCS sample to eliminate impurities of CO, several freeze-pump-thaw cycles were performed at the liquid N_2 temperature. After the purification it was confirmed that the LIF signal of the impurity CO did not appear with detectable intensities except the transition from the $j < 3$ rotational levels of the $v_{CO} = 0$ state.

The probe laser beam was introduced with a certain delay after the photolysis laser radiation to reduce the contribution from the scattered light of the photolysis laser and/or the fluorescence from the impurity CO excited by the photolysis laser. The delay time was about 30 ns when monitoring S (^{1}S) and about 160 ns when monitoring CO ($X^1\Sigma^+$).

The intensities of the respective photolysis and probe VUV laser beams were monitored after they passed through the molecular beam by being reflected by a quartz plate and guided to a solar-blind photomultiplier (Hamamatsu R1259) placed in the housing connected to the vacuum chamber. The probe UV laser intensity was monitored by detecting the weak reflex from a surface of a prism or a window by using a photodiode (Hamamatsu S1336-5BQ) before the UV laser was introduced into the vacuum chamber. The normalization of the fluorescence intensity from the fragments was performed by the monitored photolysis and probe laser intensities.

III. Results and Discussion

A. Rotational state distribution of CO ($X^1\Sigma^+$; $v_{CO} = 0, 1$)

1. Determination of Rotational state distribution

After OCS was selectively excited to the quasi-bound resonances at 64745 cm^{-1} (v*

= 0), 65595 cm^{-1} (v* = 1), and 66380 cm^{-1} (v* = 2), the LIF spectra of the $A^1\Pi$ - $X^1\Sigma^+$ (0, 0) and (1, 1) transitions of the CO fragments were measured. The observed LIF spectra exhibiting well-resolved rotational structure are shown in Figs.3 (a) and (b). On the basis of the rotational assignments, the rotational-state distributions of the CO fragment in the v_{CO} = 0 and 1 states were derived using the unperturbed rotational lines by dividing the observed rotational transition intensities by the corresponding Hönl-London factors. The derived rotational state distributions of the v_{CO} = 0 and 1 states of the CO fragments produced through the three lowest resonances of OCS are plotted in Fig.4. It should be noted in Figs.4 (a)-(f) that the populations derived from the Q branch transitions were always smaller than those derived from the P and R branch transitions. As explained below, these discrepancies are ascribed to the alignment effect of the CO fragments induced by the polarized photolysis laser light, i.e., the angular momentum vector of the CO fragment is formed preferentially in the direction perpendicular to the polarization vector of the photolysis light.[9-12]

The lifetimes of OCS in the lowest three quasi-bound vibrational resonances of $2^1\Sigma^+$, were determined to be 133 fs (v* = 0), 44 fs (v* = 1), and 27 fs (v* = 2) in our previous study.[7] These three values are all much shorter than a rotational period of OCS, and therefore, the CO photofragments could not recoil isotropically with respect to the polarization direction of the photolysis laser light within such an ultra-short time duration. In such an ultrafast dissociation process, a phenomenon originating from the correlation among (i) the polarization vector of the photolysis light, (ii) the recoil vector, and (iii) the angular momentum of the fragment can be observed.

From the conservation of the angular momentum, the total angular momentum of OCS, **J**, before the dissociation is equal to the sum of the angular momentum of the CO

fragment, **j**, and the orbital angular momentum, **L**, of the recoiling fragments of S and CO, i.e. $\mathbf{J} = \mathbf{j} + \mathbf{L}$. In our experiment, OCS is prepared under the ultracold conditions at the very low rotational temperature, the magnitude of the total angular momentum, **J**, is considered to be very small and could be assumed to be zero, i.e. $\mathbf{J} = 0$, for simplification. When $\mathbf{J} = 0$, the recoil vector, **v**, is constrained to be on the molecular plane defined by the three atoms and fixed in space during the dissociation process and both **j** and **L** (= –**j**) become perpendicular to the plane in the high $j = |\mathbf{j}|$ limit. Since the $2^1\Sigma^+ - 1^1\Sigma^+$ transition is a parallel transition, the transition moment, $\boldsymbol{\mu}_{OCS}$, is located in the molecular plane. Therefore, the correlations among the aforementioned vectors are represented as $\mathbf{v} \perp \mathbf{j}$ and $\boldsymbol{\mu}_{OCS} \perp \mathbf{j}$.

In the high j limit, the transition moment of CO, $\boldsymbol{\mu}_{CO}$, for the $A^1\Pi - X^1\Sigma^+$ transition is considered to be parallel to **j** for the Q branch transition and perpendicular to **j** for the P and R branches. In our experimental condition, the direction of the polarization of the photolysis laser light was parallel to the direction of the polarization of the probe light for the CO fragments. Therefore, the LIF intensities in the P and R branch transitions of the CO fragments should be enhanced compared with those in the Q branch transitions due to the anisotropic angular momentum distribution of CO.

By taking account of the $\boldsymbol{\mu}_{OCS}$-**v**-**j** vector correlations and the detection geometrical factor,[9,11] the Doppler line profiles for the respective P, Q, and R branch transitions were calculated in a semi-classical manner described by Dixon.[9] In the calculation, the recoil anisotropy parameter was assumed to be $\beta = 1.8$ for all the rotational states of the CO fragments, which was previously derived for the photodissociation of OCS at 157 nm.[13] After convoluting the calculated Doppler profiles by a Gaussian function with the probe laser bandwidth (FWHM ~ 0.45 cm^{-1}), the rotational spectrum was

synthesized, which can be compared with the observed rotational spectrum. Then, by dividing the observed peak intensities in the LIF spectrum by the simulated rotational transition intensities of the corresponding peaks, the corrected rotational state distributions of the CO fragments were obtained as shown in Fig.5. The extent of the discrepancies in Fig.4 between the rotational distributions obtained from the P and R branch transitions and those obtained from the Q branch transitions decreases considerably in Fig.4 especially in the high j region of the $v_{CO} = 1$ channels. However, even after the correction, there still remain some discrepancies, and the populations derived from the Q branch transitions tend to become larger than those derived from the P and R branch transitions. This tendency is most clearly seen in the low **j** region of the $v_{CO} = 0$ channel. Although the value of β was changed in the simulation to reduce the discrepancies in the low j region, these were not improved in any value of β.

The discrepancies between the populations obtained from the Q branch and those from the P and R branches could be attributed to (i) the assumption of $\mathbf{J} = 0$ and (ii) the semi-classical approximation. Even under the jet-cooled condition (T_{rot} = 6 K), the population of OCS in the rotational ground state with $\mathbf{J} = 0$ is only ~ 5 %. Consequently, the vector correlations of $\mathbf{v} \perp \mathbf{j}$ and $\boldsymbol{\mu}_{OCS} \perp \mathbf{j}$ do not always hold.[12] When the angular momentum of the CO fragment, **j**, is much larger than **J**, the semi-classical approximation becomes appropriate and the deviations from the vector correlations tend to be small. However, in the low j region, it would not be appropriate any more, and this is the reason why the discrepancies between the populations obtained from the Q branch and those from the P and R branches are larger in the low j manifold as shown in Fig.4 even after the correction considering the vector correlations.

On the other hand, as long as we concentrate on the distributions derived from

either the Q branch or the P and R branches, the effect originating from the correction considering the vector correlations was found to be negligibly small. Because the number of rotational states whose populations were determined from the P and R branches were much larger than those from Q branch lines, the P and R branch transitions were adopted to derived the rotational distributions, which were obtained simply by dividing the rotational transition intensities by the Hönl-London factors.

By assuming that the rotational distribution of the CO fragment, C(j), as that expressed by the Boltzmann distribution,

$$C(j) = C_0 (2j+1) \exp(-E_{Rot} / k_b T_{rot}) , \quad (1)$$

with a proportional constant C_0 independent of j, the rotational distributions for the v_{CO} = 0 and 1 channels for the v* = 0 – 2 resonances obtained from the P and R branch transitions were fitted by the least-squares method to derived the rotational temperatures of the CO fragments. The determined rotational temperatures are listed in Table I.

For the photodissociation via v* (= 0 – 2), the rotational temperatures of the CO fragments in v_{CO} = 0 are all very low, i.e. T_{rot} ~ 100 K, while those in v_{CO} = 1 are much higher than in v_{CO} = 0, i.e. T_{rot} = 2210 K, 940 K and 810 K for v* = 0, 1, and 2 respectively and exhibit a tendency to become lower as v* increases.

2. Comparison with model distributions

Prior distribution

We will compare the observed rotational distributions with prior distributions, in which the CO fragments are populated with probabilities proportional to a square root of the translational energy in all the energetically allowed ro-vibrational states.[14,15] If

the total angular momentum **J** of a parent triatomic molecule is approximated to be zero in its dissociation process, the angular momentum of the diatomic fragment, **j**, is perpendicular to the direction of the recoil, and the projection of **j** onto the recoil direction, m_v, becomes zero. Therefore, when calculating a prior distribution function, $P_0(v_{CO}, j)$, of the CO fragment in a single vibrational and rotational state (v_{CO}, j), the (2j+1) degeneracy of the rotational state should not be taken into account, [16] and it is represented by a square root of the translational energy as

$$P_0(v_{CO}, j) \propto (E_{avail} - E_v - E_r)^{1/2} \quad (2)$$

with

$$E_{avail} = E_{hv} - D_0 - E_S, \quad (3)$$

where E_{hv} is the energy of the photolysis light, D_0 the dissociation energy of OC-S in the electronic ground state, E_S the electronic energy of the ^1S state of the S atom measured from the $^3P_2$ state, and E_v and E_r the vibrational and rotational energies of the CO fragment, respectively.

From the rotational state distribution of the CO fragments in their specific vibrational state, $P(v_{CO}, j)$, derived experimentally in Sec. III. A. 1. and the prior distribution, $P_0(v_{CO}, j)$, the rotational surprisal, $I(g_R)$, is obtained[14-17] as

$$I(g_R) = -\ln \frac{P(v_{CO}, j)}{P_0(v_{CO}, j)} \quad (4)$$

as a function of

$$g_R = \frac{E_r}{E_{avail} - E_v} = \frac{E_r / E_{avail}}{1 - (E_v / E_{avail})} = \frac{f_R}{1 - f_v}. \quad (5)$$

The resulting plots of the rotational surprisal are shown in Fig.6 for the CO fragments in the two lowest vibrational states (v_{CO} = 0, 1) when the three lowest vibrational resonances (v* = 0 – 2) of the parents OCS molecules are excited. Then, the surprisal plots were fitted by a linear function to derive a slope. In the case of the CO fragments with v_{CO} = 0, the slopes obtained from the P-branch transitions are 119(32), 149(42), and 147(31) for v* = 0, 1, and 2, respectively, while those obtained from the Q-branch are 123(23), 100(7), and 145(24). Even though the slopes are associated with relatively large uncertainties, it can be said that the plots are well described by a linear function and that they exhibit consistently a slope of 100-150. This suggests that there exists a common mechanism which governs the rotational distribution in the v_{CO} = 0 for the three lowest resonances.[15]

In the case of the surprisal plots for v_{CO} = 1, their behavior is not so simple as that for v_{CO} = 0. In the range below g_R = 0.015, where the data for both v_{CO} = 0 and 1 are available, the P-branch data for v* = 0 and 2 of v_{CO} = 1 exhibit an almost flat distribution with respect to g_R, while those for v* = 1 exhibit a negative slope. When it comes to the global behavior of the plot in the entire range, $0 \le g_R \le 0.15$, both the P-branch and Q-branch data for v* = 0 and 1 exhibit a shallow minimum at g_R = 0.06 – 0.08 and g_R = 0.02 – 0.05, respectively. For v* = 2, it would be hard to describe the tendency due to the small data number in the plot, but the R-branch data above g_R = 0.015 exhibit a clear positive slope. It is uncertain whether the v* = 2 data have a minimum, but it can be said that the transition from the flat region to the positive slope region occurs at g_R = 0.01 – 0.02. The complex behavior of the surprisal plots

described above for the rotational distributions of the CO fragments in the v_{CO} = 1 state suggests that a simple dynamical constraint could not describe the rotational distributions. It is probable that two different kinds of dynamics govern respectively the production of the low-j and high-j CO fragments.

Rotational Franck-Condon model

When the PES of the excited state of OCS around the FC region is flat along the bending angle and no torque is imposed on the CO fragments to drive their rotational motion, the rotational state distribution is determined by the projection of the bending wavefunction of OCS in the electronic ground state onto the rotational wavefunction of the CO fragments. Within the framework of this rotational FC model, Freed and Morse[18] showed that the rotational distribution of diatomic fragments can be represented by a Boltzmann distribution when photodissociation of a linear triatomic molecule occurs from its J = 0 and v_{bend} = 0 state. By adopting the rotational FC model, Strauss *et al.*[13] calculated the rotational temperature, T_{rot}, of T_{rot} = 380 K for the CO fragments produced through OCS ($2^1\Sigma^+$). However, the PES of the $2^1\Sigma^+$ state of OCS could have a certain slope along the bending direction around the FC region which induces the bending motion of OCS and eventually imposes the torque for the rotation on CO. Whether the rotation of the CO fragment is promoted or suppressed depends on the anisotropy of the $2^1\Sigma^+$ PES along the bending angle in the course of the dissociation. Therefore, the deviation from the Boltzmann distribution with T_{rot} = 380 K, derived from the rotational FC model, could be ascribed to the anisotropy of the PES. Since the CO fragments with v_{CO} = 0 have the rotational temperature of around 100 K for all the three low-lying resonances of v* = 0 – 2, the CO fragments with v_{CO} = 0 are

considered to be formed through the anisotropic PES which tends to suppress the rotation of the fragments. On the other hand, the CO fragments with v_{CO} = 1 exhibit much higher rotational temperatures than T_{rot} = 380 K; i.e. 2210, 940, and 810 K for v* = 0, 1, and 2 respectively. Therefore, the CO fragments with v_{CO} = 1 are considered to be formed through the anisotropic PES which tends to promote the rotation of the fragments though the extent of the rotational excitation is suppressed for the higher resonance state of OCS.

3. Effect of resonances in the FC region

Previously, Strauss *et al.* [13] studied the rotational state distribution of the CO fragments produced through the photolysis of OCS at the fixed wavelength of 157 nm. The rotational distributions for v_{CO} = 0 – 3 were found to be well reproduced respectively by the Boltzmann distributions with the rotational temperatures of T_{rot} = 1350, 1300, 980, and 770 K. This decreasing tendency of T_{rot} for a larger v_{CO} shows a marked contrast with the present results obtained at the three lowest vibrational resonances for which the substantially higher rotational temperatures (1000 – 2000 K) are achieved for v_{CO} = 1 than for v_{CO}=0 (~100 K).

As was reported in our previous study,[7] a weak continuum is located at 157 nm under the jet-cooled conditions. At the peaks of the vibrational resonances (v*=0 – 2) there is a large contribution from the resonance component representing the nuclear motion along the direction perpendicular to the dissociation coordinate, while at 157 nm there is mostly the off-resonance component representing the nuclear motion along the dissociative coordinate. Therefore, the observed difference in the v_{CO} dependence of the rotational temperature could be attributed to the difference in the character of the

nuclear motion near the FC region on the upper state PES.

As shown in Fig.1, the vibrational resonances in the PHOFEX spectrum of the $2^1\Sigma^+$ - $1^1\Sigma^+$ band exhibit characteristic peak profiles; the v* = 0 resonance shows a largely asymmetrical profile shading towards the lower energy side with a narrow peak width, while the peak profile becomes more symmetrical and broader as v* increases to the v* = 1 and 2 resonances. It would be natural to expect that such a character of the resonances influences the product state distributions, because the extent of the asymmetry as well as the peak width reflects the extent of the mixing of the continuum and bound characters.[19] However, it seems that the memory of the character of the resonance state is mostly lost in the rotational state distribution for the v_{CO} = 0 channel, suggesting the existence of a strong exit-channel interaction between the FC region and the asymptotic region. The loss of the memory of the resonance states is also seen in the vibrational state distributions of CO described in the next section. On the other hand, the extent of the rotational excitation for the v_{CO} = 1 channel is more suppressed as v* increases from 0 to 2 (see Table I and Fig.6). It is possible that the remnants of the character of the resonances appear in the form of the difference in the rotational excitation for the v_{CO} = 1 channel.

B. Vibrational state distribution of CO ($X^1\Sigma^+$)

1. Vibrational state distribution of CO from Doppler profiles of S (^1S)

In order to derive the vibrational state distribution of the CO fragments, we measured the Doppler profiles of the S (^1S) fragments. Since a ^1S state has no electronic angular momentum, the Doppler profile reflects directly the recoil momentum of the S (^1S) fragments,[9,10,20] from which the kinetic energy distribution of

the S (^{1}S) fragments is obtained. Then, on the basis of the conservation of the energy and the momentum, the internal energy distribution of the CO fragments including their vibrational state distribution can be estimated as described below.

In the case of the $2^1\Sigma^+ - 1^1\Sigma^+$ transition, the electronic transition moment is parallel to the molecular axis, and the fragments are expected to eject preferentially in the direction along the laser polarization. Therefore, in order to observe the Doppler effect in a form of a clearer Doppler profile, the UV probe laser light to detect the S (^{1}S) fragments was introduced along the direction parallel with the electric vector of the photolysis laser light so that the two laser beams cross at right angles with each other.

The observed Doppler profiles obtained by exciting the central position of the peak for the three lowest resonant states; i.e. 64745 (v^* = 0), 65595 (v^* =1), and 66380 cm^{-1} (v^* = 2), are shown in Figs.7 (a)-(c). All the Doppler profiles exhibit a clear dip in the center, indicating that the released energies in the dissociation process are efficiently transferred into the translational motion rather than into the rotational and vibrational degrees of freedom of the CO fragments.

From the rotational analysis of the LIF spectra of the $A^1\Pi - X^1\Sigma^+$ (0, 0) and (1, 1) bands of the CO fragments in Sec. III. A.1., the rotational state distributions of the CO fragments in the vibrational states of v_{CO} = 0 and 1 were found to be approximated by the Boltzmann distributions for the dissociation through the three low-lying resonance states with v^* = 0 – 2. Therefore, in the simulation of the Doppler profiles of the S (^{1}S) atomic fragments, the rotational distributions for the energetically accessible vibrational states of CO were assumed to be described by the Boltzmann distributions. The rotational temperatures for the vibrational states except for v_{CO} = 0 and 1 were assumed to be the same as the corresponding values for v_{CO} = 1; i.e. T_{rot} = 2210, 940,

and 810 K, were adopted for the fragment CO (v_{CO} >1) produced through the three lowest resonance with v* = 0, 1, and 2, respectively. The recoil anisotropy parameter β was assumed again to be β = 1.8.

The Doppler profile of S (^{1}S), obtained when OCS is excited to the lowest vibrational resonance of v* = 0 is shown in Fig.8 (a), and the Doppler profiles calculated assuming that the CO fragments are populated in a single vibrational state in the range between v_{CO} = 0 and 8, are shown in Fig.8 (b). For comparison with the observed Doppler profile, the calculated Doppler profiles for v_{CO} = 0 and 8 are also drawn in Fig.8 (a) in dotted lines. When OCS is excited to v* = 0 and 1, the maximum vibrational quantum number of CO which can be produced energetically is v_{CO} = 8, and when v* = 2, the maximum becomes v_{CO} = 9. It is clearly seen in Figs.8 (a) and (b) that the contribution from the highly excited CO must be relatively small to reproduce the central dip in all the observed Doppler profiles for v* = 0 - 2.

In the course of the simulation of the Doppler profiles, it was found that the Boltzmann type distribution in which the vibrational population exponentially decreases as the vibrational energy increases was found to give the best fit. After a trial-and-error type simulation using the vibrational temperature, T_{vib}, as one variable parameter, the optimized vibrational temperature of T_{vib} = 7000$\pm$2000 K was obtained for all the three resonances of v* = 0 – 2. As shown in Fig.7, the best-fit Doppler profiles reproduced well the observed profiles. This result suggests that there exists a common mechanism for all the three resonances which governs the vibrational population of CO by affecting in a later stage after the FC region regardless of the different excitation energies.

2. Comparison with prior distributions

A prior distribution of vibrational states is obtained by the summation of $P_0(v_{CO}, j)$ over all the rotational states which are energetically accessible as

$$P_0(v_{CO}) = \sum_j P_0(v_{CO}, j) \ . \tag{6}$$

In Fig.9, the best-fit Boltzmann vibrational state distribution of T_v = 7000 K, $P_{obs}(v_{CO})$, to describe the observed Doppler profile is compared with the prior distribution calculated for the v^* = 0 resonant state of OCS. It can be seen in this figure that the CO fragments tend to be populated in the lower vibrational states than in the prior distribution. The discrepancy between the observed distribution, $P_{obs}(v_{CO})$, and the prior distribution, $P_0(v_{CO})$, is described by the vibrational surprisal, $I(f_v)$,[14,17]

$$I(f_v) = -\ln \frac{P(v_{CO})}{P_0(v_{CO})} \tag{7}$$

as a function of $f_v = E_v / E_{avail}$. The surprisal plots of the CO fragments obtained for the three lowest resonances of OCS with v^* = 0 – 2 are presented in Fig.10. All the three surprisal plots exhibits a linear slope in the range of the vibrational states of CO with v_{CO} = 0 – 6, to which most of the fragments are populated. By the fit to a straight line, the slopes were determined to be 1.90(13), 2.14(12), and 2.36(13) for v^* = 0, 1, and 2, respectively. This linear behavior commonly identified for the dissociation through the three low-lying resonances with the close values of the best-fit slopes indicates the existence of a common mechanism which governs the vibrational energy partitioning process.[15]

3. Effect of resonances in the FC region

As shown in Fig.9, the calculated vibrational distribution of CO at 7000 K which reproduces well the observed Doppler profiles obtained via the vibrational resonances of $v^* = 0 - 2$, have the larger populations in the low vibrational states than the three vibrational distributions obtained from the photodissociation at 157 nm by Strauss *et al.*[13] Because the available energy at $v^* = 0 - 2$ is larger than that obtained by the 157 nm photodissociation, this difference is contrary to the statistical model in which the population in the higher vibrational states of the fragments increases as the available energy becomes larger.

Since the photolysis at 157 nm by Strauss *et al*[13] was performed under jet-cooled conditions and the CO fragments formed in the cold region is considered to be sampled, the vibrational state distribution reported in Ref.13 could be regarded as that obtained when the off-resonant continuum is excited. It is interesting to note that the photodissociation via the three resonances, $v^* = 0 - 2$, afforded the lower vibrational temperature than the photodissociation at 157 nm. It can be said that the excitation of the vibration of the CO fragments is suppressed when the dissociation proceeds through the resonance states of the quasi-bound vibration in the FC region, while the energy partitioning into the fragment vibration becomes efficient when the off-resonant continuum is excited.

The observation that the similar vibrational distributions are obtained for all the three resonance states, $v^* = 0 - 2$, indicates that the quasi-bound vibration in the FC region would not affect so much the vibrational distribution of the CO fragments. This means that the product state distribution is determined in the region between the FC region and the asymptotic region. In other words, the memory of the vibration in the

FC region tends to be lost when the dissociation proceeds.

In the cases of the photodissociation of FNO (S_1)[23, 24] and ClNO (T_1, S_1)[25-27], their PHOFEX spectra exhibited distinct vibrational peaks and they were interpreted as the vibrational Feshbach resonances. Therefore, the vibrational dynamics of FNO and ClNO in their FC region is considered to have a certain similarity to OCS $(2^1\Sigma^+)$. However, contrary to OCS, the vibrational distributions of the diatomic photofragments produced from FNO and ClNO were interpreted by an adiabatic picture, in which most of the NO fragments produced via the vibrational Feshbach resonance with the quantum number, v^*, are populated in the vibrational state with the quantum number, v_{NO}, equal to v^* or v^*-1. This type of an adiabatic distributions suggests that the vibrational motion of the NO moiety of the parent molecules in the FC region is very close to the vibrational motion of the NO fragments and keeps its nature of local vibration in the course of the dissociation process.

As far as the vibrational distributions of the diatomic fragments are concerned, the photodissociation of OCS $(2^1\Sigma^+)$ are closer to the symmetric triatomic molecules of H_2O $(\tilde{A}, {}^1B_1)$[28-32] and O_3 (Chappuis Band[33-35] and Hartley Band[36-39]) rather than the X-NO type molecules even though the broad absorption features of H_2O and O_3 exhibit no vibrational progression. When these symmetric triatomic molecules are excited to the dissociative PES of the electronically excited state, they start to move along the symmetric stretch coordinate from the FC point towards the saddle point. Though the potential along the symmetric stretch coordinate is bound, this motion is unstable and is deformed into the mixture of the translational motion along the anti-symmetric stretch coordinate and the vibration of the diatomic fragment, which is expected to cause the breakdown of the vibrational adiabaticity.

In the case of OCS, the vibrational motion near the FC region is considered to be close to the in-phase stretching in both the O-C and C-S bonds as was demonstrated by the wavepacket calculation in our previous study.[7] Therefore, in the course of the dissociative process, the vibrational motion in the FC region would be transferred into both the translational motion and the vibration of the CO fragments, and during this process the vibrational adiabaticity would be lost, resulting in the similar vibrational state distribution to O_3 and H_2O.

IV Conclusion

We investigated the photodissociation of OCS via the $2^1\Sigma^+$ state by measuring the rotational and vibrational state distributions of the CO fragments produced through the three lowest vibrational resonances in the $2^1\Sigma^+$-$1^1\Sigma^+$ band. Since the dissociation, OCS $(2^1\Sigma^+) \rightarrow CO\ (X^1\Sigma^+) + S\ (^1S)$, proceeds on a single PES of the $2^1\Sigma^+$ state, this band system affords us an ideal opportunity to study the pure nuclear dynamics in the course of the dissociation process.

(1) The rotational distributions of the CO fragments in the $v_{CO} = 0$ and 1 vibrational states were derived for the three lowest resonance peaks, $v^* = 0 - 2$, of OCS by measuring the rotational structures of the LIF spectra of the one-photon CO $A^1\Pi$ - $X^1\Sigma^+$ (0, 0) and (1, 1) transitions. The rotational state distributions in $v_{CO} = 0$ for $v^* = 0 - 2$ were all represented approximately by the Boltzmann distribution of around 100 K. On the other hand, the CO fragments in $v_{CO} = 1$ were much more excited rotationally than CO ($v_{CO} = 0$) and the distributions were approximated by the Boltzmann distributions with $T_{rot} = 2210 \pm 280$, 940 ± 120, and 810 ± 65 K for $v^* = 0$, 1, and 2, respectively. From the comparison with the rotational temperatures of the CO

fragments obtained by the photolysis at 157 nm and those by the rotational FC model, the characteristic rotational temperatures derived here were considered to reflect the character of the vibrational resonances in the FC region. The difference in the rotational distribution of the $v_{CO} = 0$ and $v_{CO} = 1$ channels was also identified as the difference in their surprisal plots.

(2) From the measurements of the Doppler profiles of the S (^{1}S) atomic fragments, the vibrational distributions of the CO fragments were determined and they were found to be well approximated by the Boltzmann distribution with the temperature of 7000 ± 2000 K. The common vibrational distribution obtained for all the three lowest resonance states with similar shapes in their surprisal plots indicates that the dissociation channels which form the CO fragments in the different v_{CO} values are coupled strongly with each other after OCS leaves the FC region, leading to the breakdown of the vibrational adiabaticity.

References

[1] R. Schinke, *Photodissociation Dynamics* (Cambridge University Press, New York, 1993)

[2] E. J. Heller, Acc. Chem. Res. **14**, 368 (1981)

[3] C. D. Pibel , K. Ohde, and K. Yamanouchi, J. Chem. Phys. **101**, 834 (1994)

[4] K. Yamanouchi, K. Ohde, A. Hishikawa, and C. D. Pibel, Bull. Chem. Soc. Jpn. **68**, 2459 (1995)

[5] K. Ohde, A. Hisikawa, and K. Yamanouchi, J. Elect. Spec. Rel. Phenom. **79**, 433 (1996)

[6] K. Yamanouchi, K. Ohde, and A. Hishikawa, Adv. Chem. Phys. **101**, 789 (1997)

[7] A. Hishikawa, K. Ohde, R. Itakura, S. Liu, K. Yamanouchi, and K. Yamashita, J. Phys. Chem. A **101**, 694 (1997)

[8] K. Yamanouchi, and S. Tsuchiya, J. Phys. B **28**, 133 (1995)

[9] R. N. Dixon, J. Chem. Phys. **85**, 1866 (1986)

[10] P. L. Houston, J. Phys. Chem. **91**, 5388 (1987)

[11] C. H. Green and R. N. Zare, J. Chem. Phys. **78**, 6741 (1983)

[12] G. E. Hall, N. Sivakumar, D. Chawla, P. L. Houston, and I. Burak, J. Chem. Phys. **88**, 3682 (1988)

[13] C. E. Strauss, G. C. McBane, P. L. Houston, I. Burak, and J. W. Hepburn, J. Chem. Phys. **90**, 5364 (1989)

[14] R. D. Levine, and R. B. Bernstein, Acc. Chem. Res. **7**, 394 (1974)

[15] J. I. Steinfeld, J. S. Francisco, and W. L. Hase, Chemical Kinetics and Dynamics (Prentice-Hall, New Jersey, 1989)

[16] J. T. Muckerman, J. Phys. Chem. **93**, 179 (1989)

[17] E. Zamir, R. D. Levine, and R. B. Bernstein, Chem. Phys. Lett. **107**, 217 (1984)

[18] M. D. Morse and K. F. Freed, J. Chem. Phys. **74**, 4395 (1981)

[19] U. Fano, Phys. Rev. **124**, 1866 (1961)

[20] R. N. Zare, Mol. Photochem. **4**, 1 (1972)

[21] J. W. Rabalais, J. M. McDonald, V. Scherr, and S. P. McGlynn, Chem. Rev. **71**, 73 (1971)

[22] M. I. McCarthy and V. Vaida, J. Phys. Chem. **90**, 6759 (1986)

[23] S. A. Reid, J. T. Brandon, and H. Reisler, J. Phys. Chem. **97**, 540 (1993)

[24] J. T. Brandon, S. A. Reid, D. C. Robie, and H. Reisler, J. Chem. Phys. **97**, 5246 (1992)

[25] C. X. W. Qian, A. Ogai, L. Iwata, and H. Reisler, J. Chem. Phys. **92**, 4296 (1990)

[26] A. Ogai, C. X. W. Qian, and H. Reisler, J. Chem. Phys. **93**, 1107 (1990)

[27] C. X. W. Qian, A. Ogai, J. T. Brandon, Y. Y. Bai, and H. Reisler, J. Phys. Chem. **95**, 6763 (1991)

[28] P. Anderson, G. S. Ondrey, B. Titze, and E. W. Rothe, J. Chem. Phys. **80**, 2548 (1984)

[29] V. Engle, V. Staemmler, R. L. Vander Wal, F. F. Crim, R. J. Sension, B. Hudson, P. Andersen, S. Hennig, K. Weide, and R. Schinke, J. Phys. Chem. **96**, 3201 (1992)

[30] D. W. Hwang, X. Yang, and X. Yang, J. Chem. Phys. **110**, 4119 (1999)

[31] V. Engle, R. Scihnke, and V. Staemmler, J. Chem. Phys. **88**, 129 (1988)

[32] M. L. Doublet, G. J. Kroes, E. J. Baerends, and A. Rosa, J. Chem. Phys. **103**, 2538 (1995)

[33] D. S. Moore, D. S. Bomse, and J. J. Valentini, J. Chem. Phys. **79**, 1745 (1983)

[34] H. B. Levene, J.–C. Nieh, and J. J. Valentini, J. Chem. Phys. **87**, 2583 (1987)

[35] B. Woywod, M. Stengle, W. Domcke, H. Flöthmann, and R. Schinke, J. Chem. Phys. **87**, 2583 (1987)

[36] J. J. Valentini, D. P. Gerrity, D. L. Phillips, J.–C. Nieh, and K. D. Tabor, J. Chem. Phys. **86**, 6745 (1987)

[37] C. Leforestier, F. LeQuéré, K. Yamashita, and K. Morokuma, J. Chem. Phys. **101**, 3806 (1994)

[38] B. R. Johnson and J. L. Kinsey, Phys. Rev. Lett. **62**, 1607 (1989)

[39] B. R. Johnson and J. L. Kinsey, J. Chem. Phys. **91**, 7638 (1989)

Table I. The rotational temperatures (in K) for the CO fragments in the v_{CO} = 0 and 1 states produced through the three lowest vibrational resonances of v* = 0 – 2 of OCS in the $2^1\Sigma^+$ state.[a)]

	v_{CO} = 0	v_{CO} = 1
v* = 0	95 (10)	2210 (280)
v* = 1	100 (30)	940 (120)
v* = 2	90 (15)	810 (65)

a) The numbers in the parentheses represent a standard deviation (σ) derived from the least-square fit to the Boltzmann-type rotational distribution.

Figure Captions

Fig. 1. The PHOFEX spectrum of the entire region of the $2^1\Sigma^+$-$1^1\Sigma^+$ band of OCS measured in our previous study (Ref. 7).

Fig. 2. Schematic diagram of the experimental setup for the pump and probe measurements using two tunable VUV laser light sources. The photolysis light source excites OCS to the three lowest resonances of the $2^1\Sigma^+$ state and the probe light source probes the CO fragments thorough the $A^1\Pi$ - $X^1\Sigma^+$ transitions. For probing the S(^{1}S) fragments, a tunable UV light source is used in place of the VUV light source for the probe (See Sec.II).

Fig. 3. The observed LIF spectra for the (a) $A^1\Pi$-$X^1\Sigma^+$ (0, 0) and (b) $A^1\Pi$-$X^1\Sigma^+$ (1, 1) bands of CO produced via the lowest vibrational resonance with $v^* = 0$ of the $2^1\Sigma^+$ state of OCS.

Fig. 4. The observed rotational state distributions of the CO fragments in the vibrational states of $v_{CO} = 0$ and 1 via the three lowest vibrational resonances of $v^* = 0 - 2$, derived by taking account only of the Hönl-London factor from the peak intensities of the P (▲), Q (○), and R (■) branches in the observed LIF spectra. The length of the bar for the data points represents the experimental uncertainty (σ).

Fig. 5. The corrected rotational state distributions of the CO fragments obtained from Fig.3 by taking account of the vector correlations among the photolysis laser polarization, the fragment recoil, and the angular momentum of the CO fragments.

Fig. 6. The rotational surprisal plots, $I(g_R)$s, for the CO fragments in the vibrational states of v_{CO} = 0 and 1 produced via the quasi-bound vibrational resonances of v* = 0, 1, and 2. The data derived from the intensities of the observed P (▲), Q (○), and R (■) branches in the LIF spectra are plotted with different marks. The straight lines drawn in (a) – (c) represent the best-fit linear lines for the surprisal plots for v_{CO} = 0. For v_{CO} = 1, the three plots do not exhibit simple linear behavior, and therefore, no straight line is drawn.

Fig. 7. The observed (open circles) and best-fit (solid lines) Doppler profiles of the S(^{1}S) fragments for the photodissociation of OCS ($2^1\Sigma^+$) via the quasi-bound states of (a) v* = 0, (b) v* = 1, and (c) v* = 2. In the trial-and-error simulation, the vibrational distributions of the CO fragments were assumed to be represented by the Boltzmann-type distribution and the same optimized vibrational temperatures of T_{vib} = 7000 K were derived for all the three profiles (See text for details).

Fig. 8. (a) The observed Doppler profile of the S(^{1}S) fragments when OCS was excited to the lowest quasi-bound resonances with v* = 0 (solid line). The calculated Doppler profiles are shown for comparison for the lowest vibrational state (v_{CO} = 0) and the highest vibrational state (v_{CO} = 8) (dotted lines) when the CO fragments are assumed to be populated only in the single vibrational state. (b) The calculated Doppler profiles are shown for all the vibrational states, v_{CO} = 0 – 8, which are energetically accessible.

Fig. 9. The normalized vibrational state distributions of the CO fragments produced

after the photodissociation of OCS ($2^1\Sigma^+$); (a) the Boltzmann distribution of 7000 K which reproduces all the observed Doppler profiles of the S(^{1}S) fragments when the v* = 0 – 2 resonances of OCS are excited, (b) the prior distribution calculated for the v* = 0 resonance, and (c) the vibrational distribution for v_{CO} = 0 - 3 obtained by Strauss *et al* [6] for the photodissociation at 157 nm. For the normalization for (c), the amount of the population in each of v_{CO} = 4 - 8 is assumed to be 5 % of v_{CO} = 0, which was estimated in Ref. 13 as an upper limit of the population for these five vibrational states.

Fig. 10. The vibrational surprisal plots, I(f_v)s, for the CO fragments obtained via the quasi-bound resonances; (a) v* = 0, (b) v* =1, and (c) v* = 2. The slopes of the fitted lines to the surprisal plots in the range between v_{CO} = 0 and 6, are 1.90(13), 2.14(12), and 2.36(13) for v* = 0, 1, and 2, respectively.

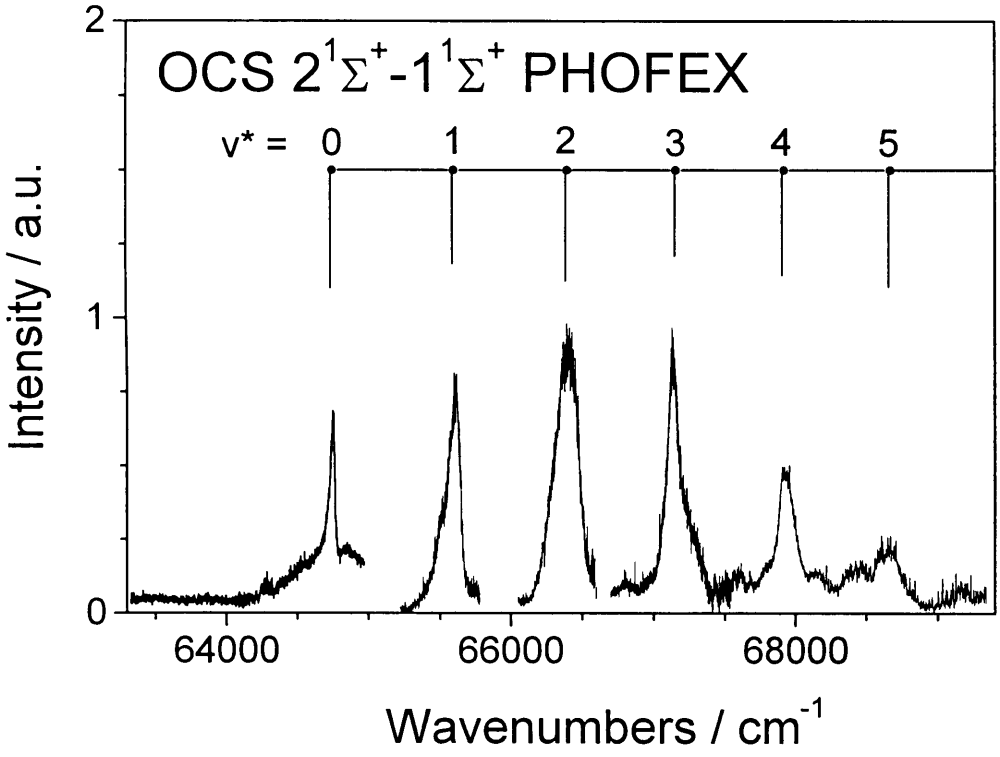
OCS $2^1\Sigma^+$-$1^1\Sigma^+$ PHOFEX
v* = 0 1 2 3 4 5
Intensity / a.u.
0
1
2
64000
66000
68000
Wavenumbers / cm^{-1}

Fig. 1

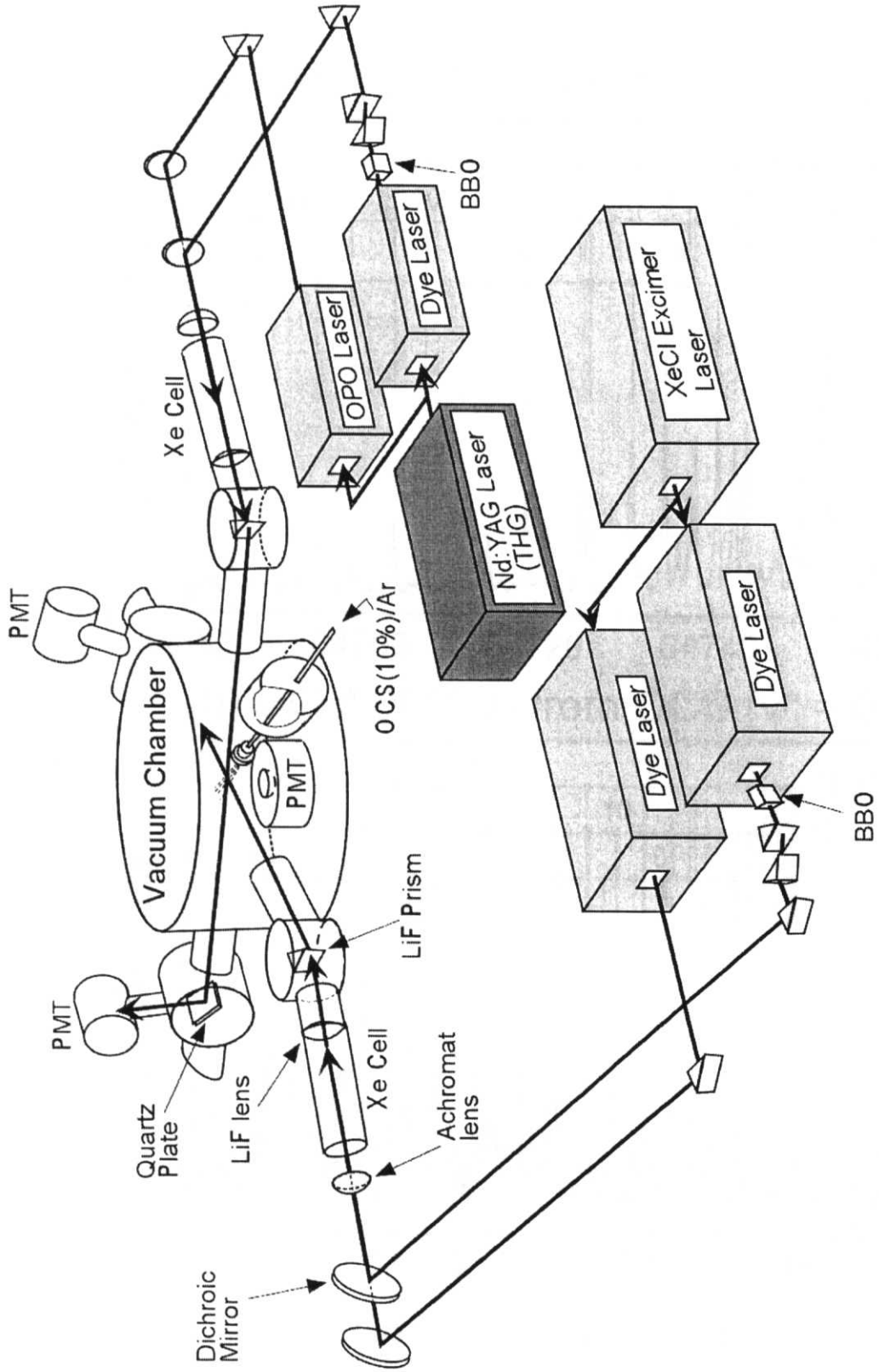
BBO
Dye Laser
OPO Laser
Xe Cell
XeCl Excimer Laser
Nd:YAG Laser (THG)
PMT
OCS(10%)/Ar
Vacuum Chamber
Dye Laser
Dye Laser
BBO
PMT
LiF Prism
PMT
Xe Cell
Quartz Plate
LiF lens
Achromat lens
Dichroic Mirror

Fig.2

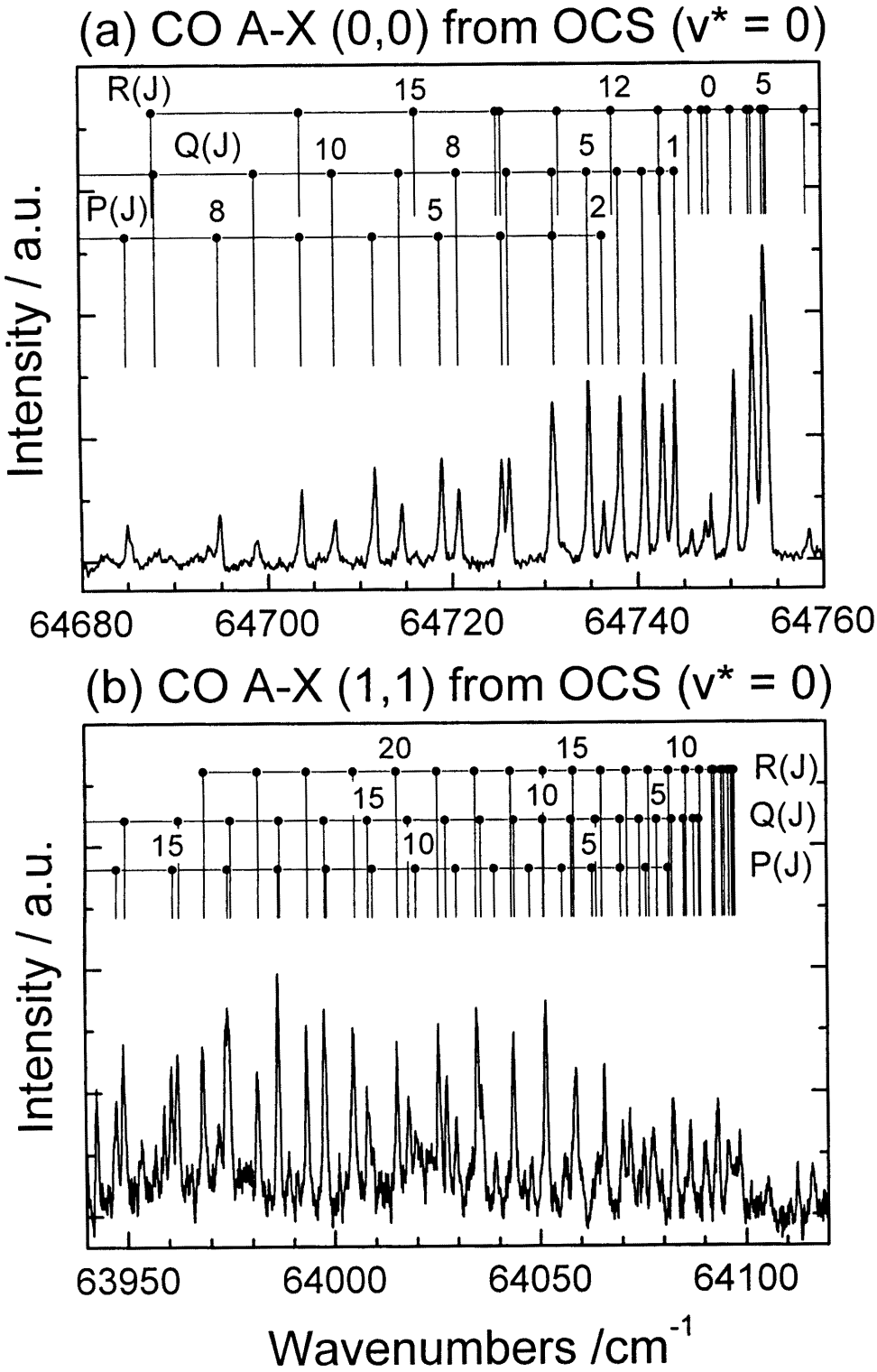
(a) CO A-X (0,0) from OCS (v* = 0)
R(J)
Q(J)
P(J)
15
12
0
5
10
8
5
1
8
5
2
Intensity / a.u.
64680
64700
64720
64740
64760
(b) CO A-X (1,1) from OCS (v* = 0)
20
15
10
R(J)
15
10
5
Q(J)
15
10
5
P(J)
Intensity / a.u.
63950
64000
64050
64100
Wavenumbers /cm-1

Fig. 3

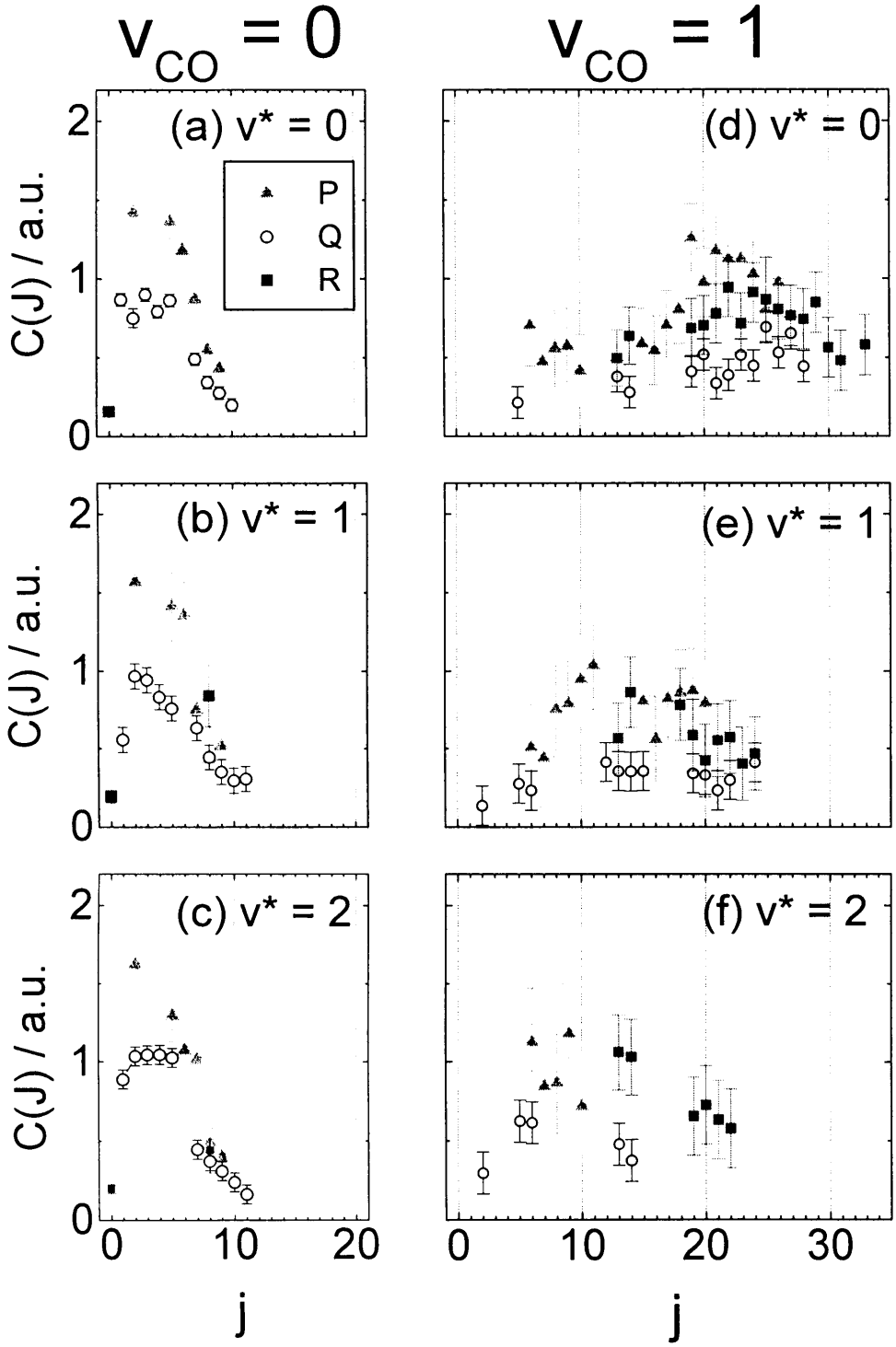

Fig. 4

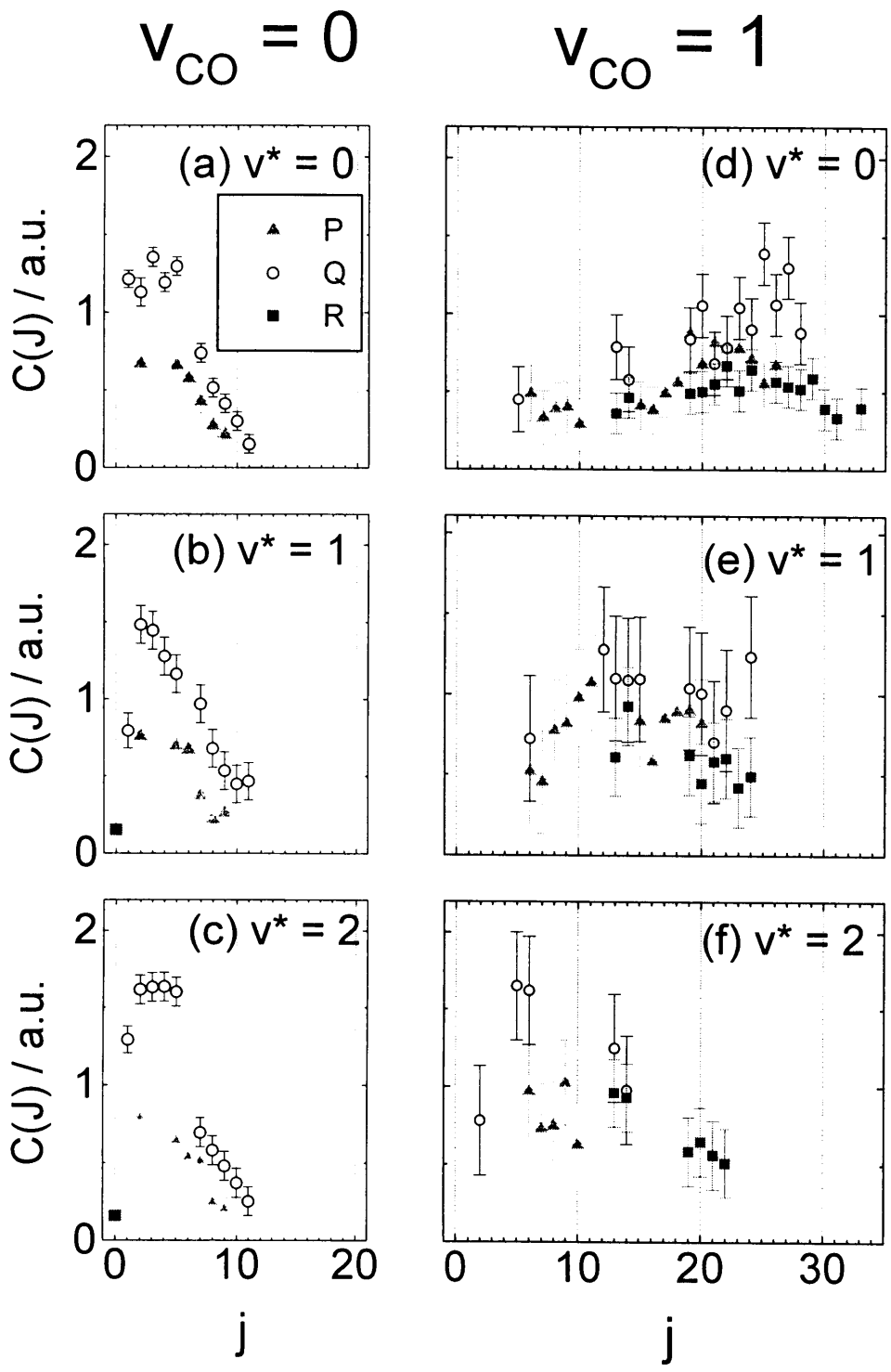

Fig. 5

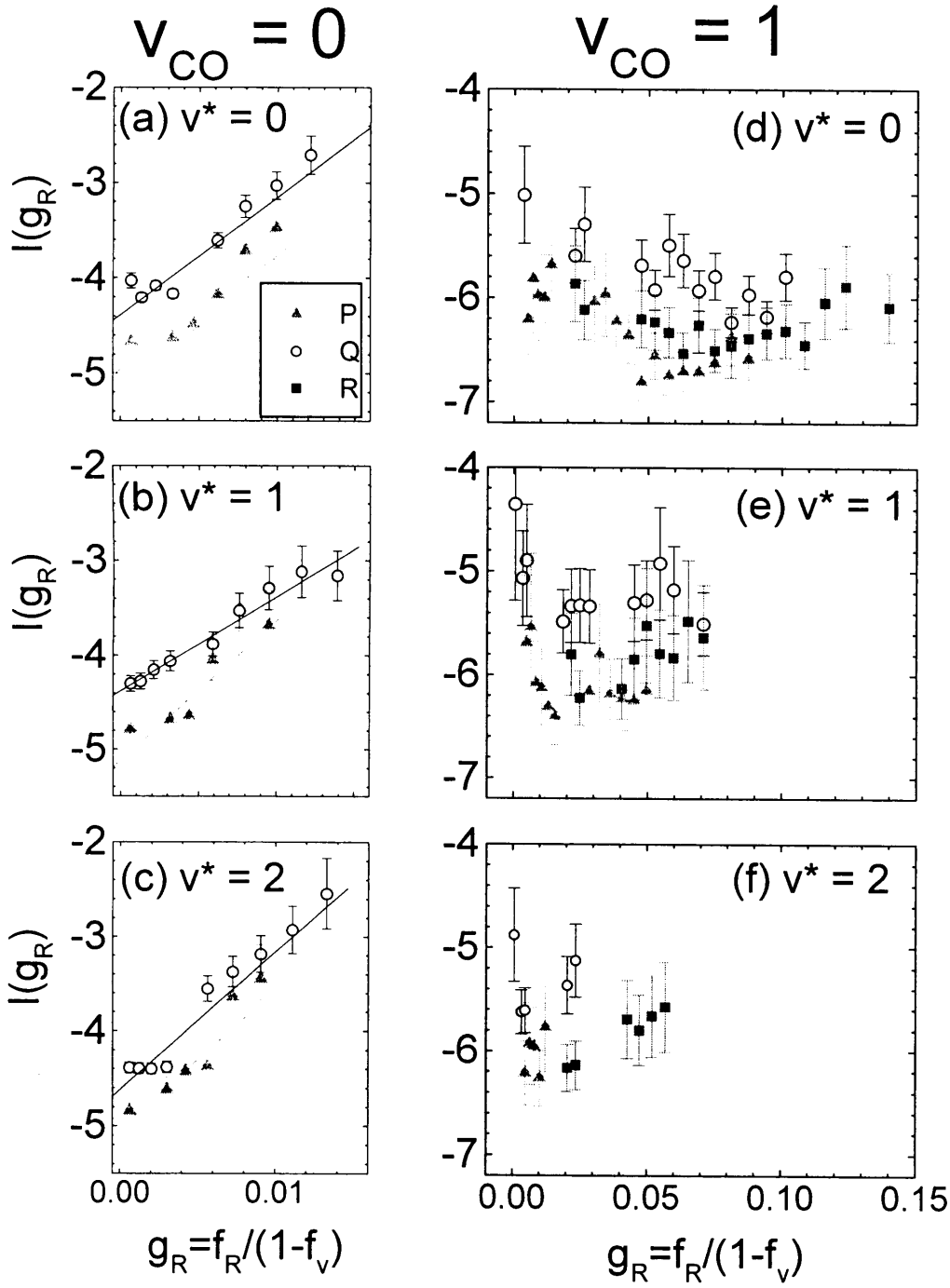
v_CO = 0
v_CO = 1
(a) v* = 0
(b) v* = 1
(c) v* = 2
(d) v* = 0
(e) v* = 1
(f) v* = 2
P
Q
R
I(g_R)
g_R=f_R/(1-f_v)
-2
-3
-4
-5
-6
-7
0.00
0.01
0.05
0.10
0.15

Fig. 6

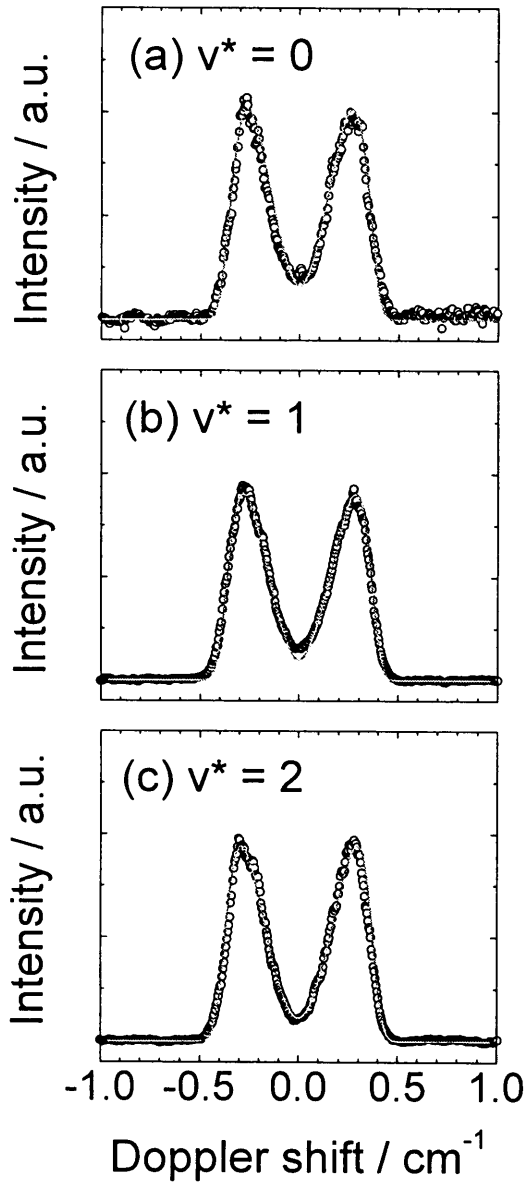
(a) v* = 0
(b) v* = 1
(c) v* = 2
Intensity / a.u.
Intensity / a.u.
Intensity / a.u.
-1.0 -0.5 0.0 0.5 1.0
Doppler shift / cm-1

Fig. 7

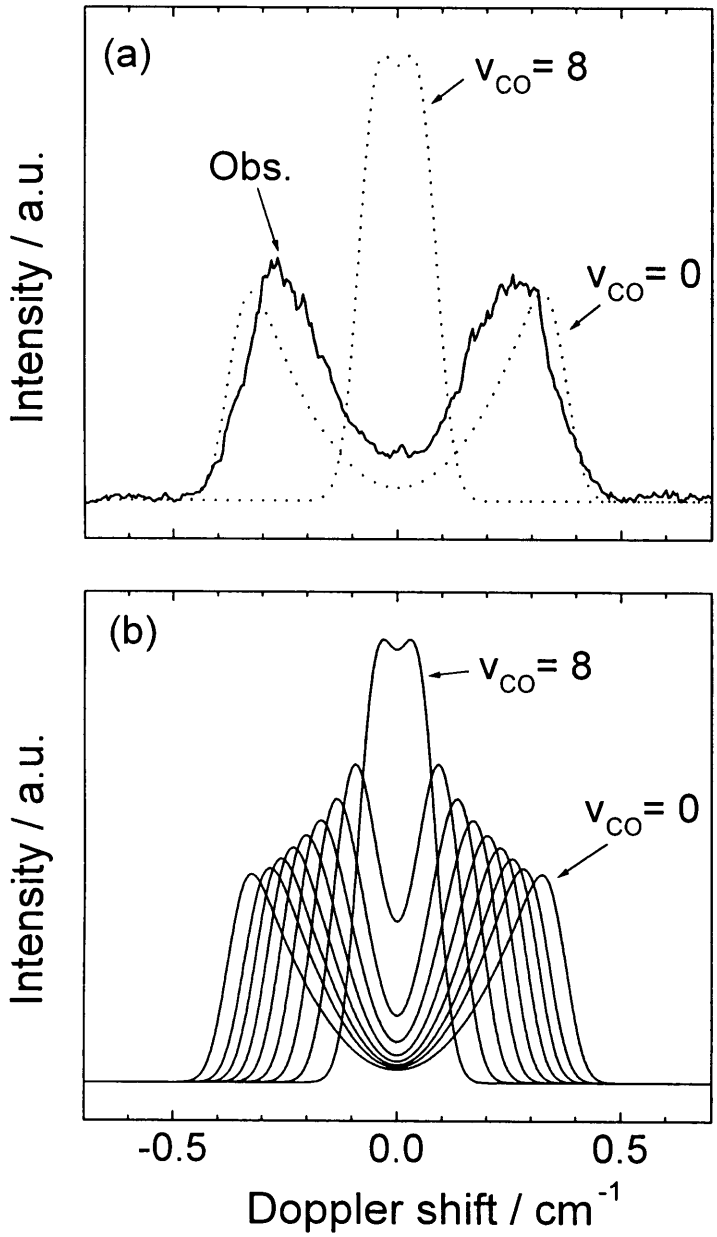
(a)
v_{CO}= 8
Obs.
v_{CO}= 0
Intensity / a.u.
(b)
v_{CO}= 8
v_{CO}= 0
Intensity / a.u.
-0.5
0.0
0.5
Doppler shift / cm^{-1}

Fig. 8

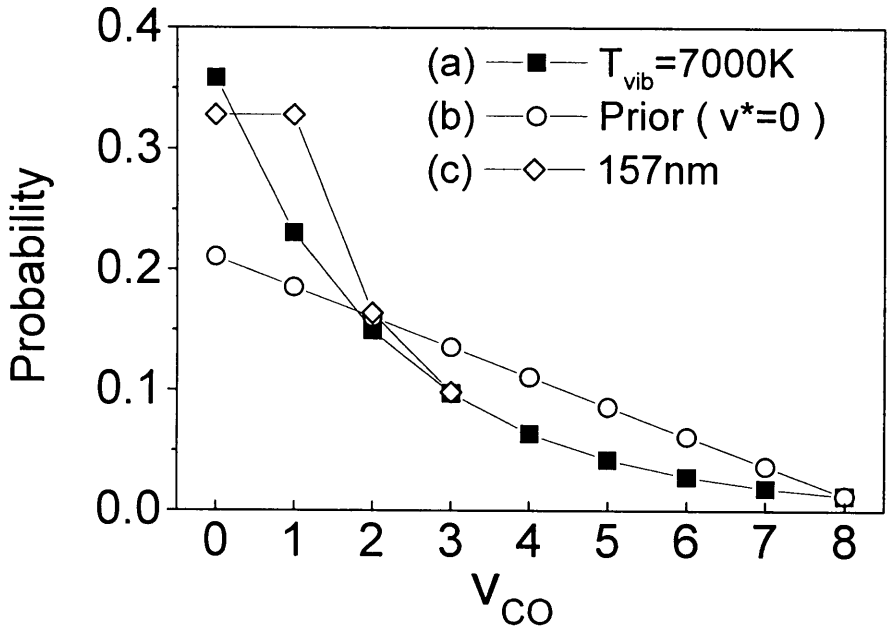
0.4
0.3
0.2
0.1
0.0
Probability
0
1
2
3
4
5
6
7
8
V_{CO}
(a) T_{vib}=7000K
(b) Prior (v*=0)
(c) 157nm

Fig. 9

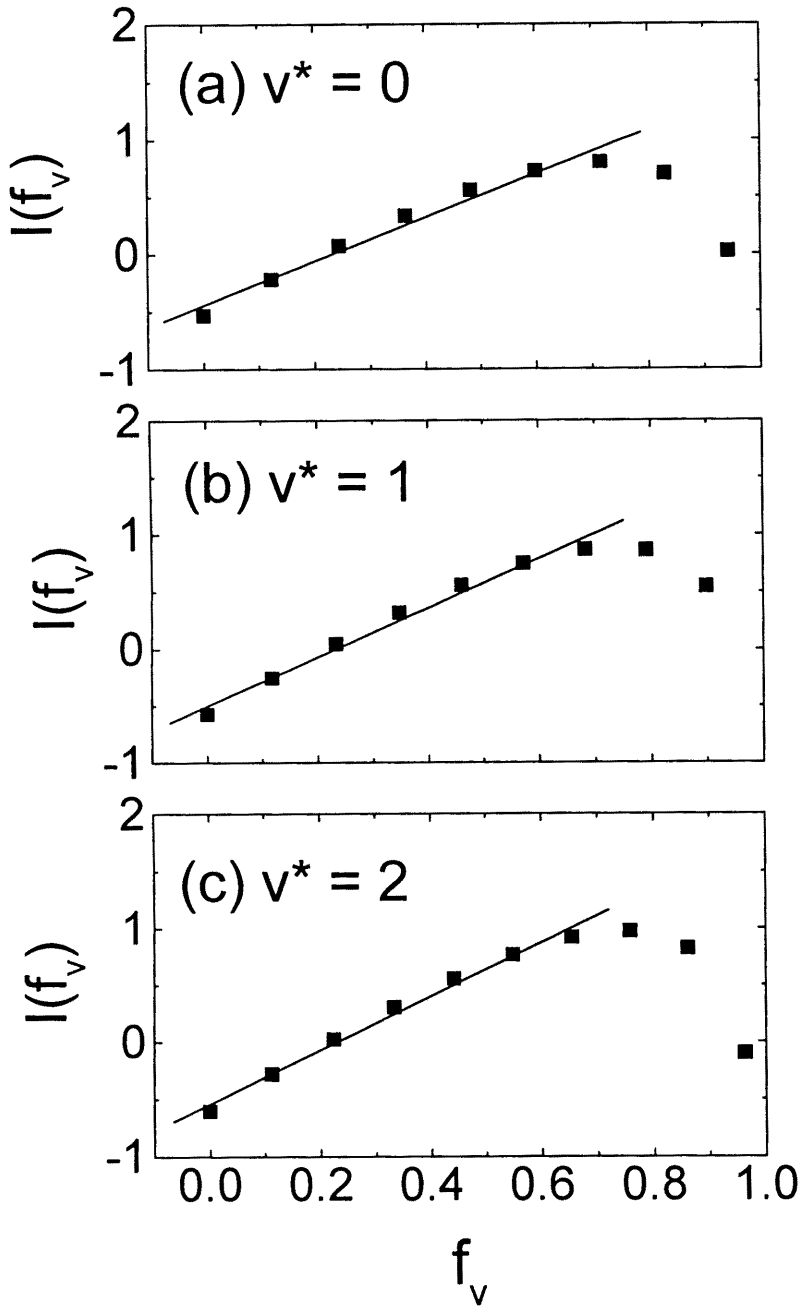

Fig. 10

Chapter 3

Resonances in the ultrafast photodissociation of OCS ($2^1\Sigma^+$) by two-photon excitation spectroscopy

Abstract

By probing S(^{1}S) photofragments, the two-photon photofragment excitation spectrum of OCS was measured in the entire energy region (63800 - 69300 cm^{-1}) of the $2^1\Sigma^+$ - $1^1\Sigma^+$ band. After trial-and-error simulations of the spectrum, weak features identified between the strong resonance peaks were ascribed to the resonances caused by the quasi-bound bending excitation of OCS in the transition state region of the mostly repulsive potential energy surface of $2^1\Sigma^+$.

I. Introduction

The absorption spectrum of the $2^1\Sigma^+$ - $1^1\Sigma^+$ band of OCS exhibits the distinct progression of the strong resonance peaks,[1,2] and more than 80 % of OCS molecules in the $2^1\Sigma^+$ state undergo the fragmentation into $CO(X^1\Sigma^+)$ and $S(^1S)$.[3] In our previous studies, the photofragment excitation (PHOFEX) spectra in which the $S(^1S)$ fragments were monitored were measured by using a tunable VUV laser as an excitation light source.[4-8] The resonance peaks were respectively measured under jet-cooled conditions in which the heterogeneous line broadening caused by the vibrational and rotational excitation of OCS are suppressed. Combining the measured PHOFEX spectra with the wavepacket study on the 2D *ab initio* potential energy surface (PES) of the $2^1\Sigma^+$ state, the nuclear motion of dissociating OCS molecules was discussed.[8] The strong resonance peaks were considered to be caused by the in-phase mixing with the C-S and C-O stretching modes on the $2^1\Sigma^+$ PES.

On the other hand, in our recent measurements of the product state distributions of the CO fragments via the resonant states of $v^* = 0 - 2$,[9] it was revealed that the dissociation channels to the different vibrational states of the CO fragments are strongly coupled to each other and the characteristic rotational distributions of the CO fragments ($v_{CO} = 0, 1$) were obtained. These results suggest that the dissociation dynamics in the $2^1\Sigma^+$ state could not be described using a simple pictures such as a vibrational adiabatic model[10] in which the bending motion of OCS is neglected. In these previous studies, attention has been paid to the strong resonance peaks forming an apparent progression, and the weak profiles appearing in the tail region of the main progression have not been discussed.

It has been well known that the diffused absorption spectrum contains the

information about the nuclear dynamics in the Franck-Condon region on the dissociative PES.[10-13] As the nuclear motion on the PES becomes more complex, it is more important to examine the spectral structure in the entire energy range of the electronic band to derive the dynamical information. For example, from the spectral structure of the Hartley system of O_3, several unstable periodic orbits on its dissociative PES have been discussed.[14,15]

In the present study, the PHOFEX spectrum in the entire energy range of $2^1\Sigma^+$ - $1^1\Sigma^+$ band was measured by the two-photon excitation scheme and the resonance structure in the spectrum was re-investigated to clarify the origin of the weak progression.

II. Experiment

In our previous study, the tunable VUV laser generated by the two-photon resonant four-wave different frequency mixing ($2\omega_1 - \omega_2$) in the Xe gas was employed to pump the jet-cooled OCS molecules to the $2^1\Sigma^+$ state. The details of the experimental setup for the VUV-PHOFEX measurement were described previously.[8,9] When we measure an excitation spectrum by varying the wavelength of the VUV photolysis laser, the beam spot of the VUV laser at the laser molecule interaction region moves along the horizontal direction by the dispersion of a LiF prism used for separating the VUV light from the ω_1 and ω_2 laser beams. It becomes necessary to reduce this beam walk effect in order to derive properly spectral profiles in the observed energy range. Because of this difficulty the measurements of the PHOFEX spectrum have been limited to the narrow energy regions around the resonance peaks in the previous studies.[4-8]

In the present study in order to reduce the beam walk effect of the VUV laser

during the measurements, the angle of the LiF prism was rotated by a stepping motor (Oriental Motor, UFK544A) controlled by a personal computer which controlled the wavelength scan of the dye laser (ω_2) and acquired the signal data simultaneously. During the measurements of the PHOFEX spectrum, the prism was rotated at a constant rate from the optimized angle for the start wavelength to that for the end wavelength. In Fig. 1(a), the PHOFEX peak profile of the 154 nm band measured with the optimized prism rotation and that measured without the prism rotation are compared with each other. This prism-tracking system with the stepping motor enabled us to measure the profiles of the broad feature around the 157 nm (63700 cm^{-1}) as reported previously.[8]

On the other hand, using ultraviolet (UV) laser light the two-photon PHOFEX spectrum of the $2^1\Sigma^+ - 1^1\Sigma^+$ band of OCS was measured. The experimental setup for the PHOFEX measurement by the two-photon excitation is shown in Fig. 2. A sample gas [OCS (10%)/Ar] was expanded into the vacuum chamber by a pulsed nozzle (10 Hz) with 0.8 mm orifice diameter. When the pulsed valve was operated with the stagnation pressure of 1.5 atm, the pressure in the chamber was about 2×10^{-4} Torr. The rotational temperature of OCS under the jet condition was estimated to be about 6 K which is the rotational temperature of CO contained in OCS sample (Matheson 97.5 % purity) derived from the measurement of the excitation spectrum of the $A^1\Pi$-$X^1\Sigma^+$ band of CO. A frequency-doubled output (λ: 287.7 – 314.9 nm) of a tunable dye laser (Lambda Physik, Scanmate) pumped by third harmonics of a Nd-YAG laser (Coherent, Infinity 40-100) was used to excite OCS to the $2^1\Sigma^+$ state through the two-photon absorption. A frequency-doubled output (λ: 219 nm) of the other dye laser (Lambda Physik, Scanmate) pumped by a XeCl excimer laser (Lambda Physik, EMG 101MSG) was tuned to the $^3D^o - ^1S$ transition of S atom for monitoring the yields of the

$S(^1S)$ fragments. The fluorescence of λ = 147 nm from the $^3D^o$ state to the ^3P state was detected by a solar-blind photomultiplier (Hamamatsu, R1259) with a set of light-collection optics.

Even though the selection rules of the rotational transitions for the two-photon UV PHOFEX spectrum are different from those for the one-photon VUV PHOFEX spectrum, the ultrafast photodissociation process occurring on the $2^1\Sigma^+$ PES on the time scale much shorter than a period of molecular rotation is expected to make these two excitation spectra almost identical. The spectral structure of the $2^1\Sigma^+$–$1^1\Sigma^+$ band is determined by the Franck-Condon integral. Indeed, as shown in Fig 1(b), the UV two-photon PHOFEX spectrum and the VUV one-photon PHOFEX spectrum are matched well in the 64400 – 65000 cm^{-1} region as far as the VUV-PHOFEX spectrum was measured with the LiF prism tracking system. Therefore, in order to circumvent the laborious task to correct the beam walk effect, the two-photon excitation scheme was employed in the present study to measure the overall spectral structure in the entire energy range of the $2^1\Sigma^+$ - $1^1\Sigma^+$ band.

III. Results and Discussion

A. Resonances in the PHOFEX spectrum

The observed two-photon PHOFEX spectrum is shown in Fig. 3(a). The weak features are identified between the strong peaks assigned to the quasi-bound vibrational resonances for the in-phase motions of the C-S and C-O stretches.[8] These weak features can be ascribed to either resonance states different from the stronger ones or an interference pattern associated with the main resonances. In order to investigate whether the interference among the stronger resonances could generate such smaller

peaks in their tail region, the simulations were preformed by taking account of only seven stronger resonances.

It has been known that an appropriate linear combination of initial continuum states leading to different ro-vibrational states of molecular fragments can be transformed into one continuum state coupled to the resonance state and the other continuum states decoupled to the resonance state.[9] In our previous studies,[5-8] the shape of the main resonance peaks was fitted to a Fano type line profile formula for the one discrete state coupled to one continuum expressed as

$$\sigma_{v^*} = \sigma_b + \sigma_{v^*} \frac{(q_{v^*} + \varepsilon_{v^*})^2}{1 + \varepsilon_{v^*}^2} , \qquad (1)$$

where (i) $\varepsilon_{v^*} = \frac{2(E - E_{v^*})}{\Gamma_{v^*}}$ is a dimensionless energy offset from the resonant energy, E_{v^*}, (ii) Γ_{v^*} is the width of the peak, and (iii) σ_{v^*} and σ_b are the cross sections to the dissociative continua which are coupled and decoupled to the 0th order resonance state, respectively.[16] The asymmetry parameter q_{v^*} is defined as

$$q_{v^*} = \frac{\langle \phi_{v^*} | \mathbf{T} | \Psi^0_{v^* E} \rangle}{\pi \langle \phi_{v^*} | \mathbf{H} | \Psi^0_{v^* E} \rangle \langle \Psi^0_{v^* E} | \mathbf{T} | \Psi_0 \rangle} , \qquad (2)$$

where **T** and **H** represent the optical transition operator and the molecular Hamiltonian on the $2^1\Sigma^+$ PES, respectively, and Ψ_0, ϕ_{v^*}, and $\Psi^0_{v^*, E}$, are the initial wavefunction in the electronic ground state, the wavefunction of the modified resonance state, and the

wavefunction of the continuum coupled to the resonance state at the energy level of E, respectively.

However, if the widths of the resonance peaks becomes comparable with the spacing among the resonance peaks, an effect of the overlapping resonance needs to be taken into account.[16-18] The extent of the overlap between two continuum wavefunctions coupled respectively to two resonance states, m and n, can be expressed by an overlap matrix defined as [17]

$$\left\langle \Psi^{0}_{\mathrm{m}\,E} \middle| \Psi^{0}_{\mathrm{n}\,E'} \right\rangle = \mathrm{O}_{\mathrm{mn}}\,\delta(E-E'), \quad (0 \le \mathrm{O}_{\mathrm{mn}} \le 1) \tag{3}$$

where $\Psi^{0}_{\mathrm{n}\,E}$ can be expressed as

$$\Psi^{0}_{\mathrm{n}\,E} = \left(\frac{2\pi}{\Gamma_n}\right)^{\frac{1}{2}} \sum_{\beta} V_{n\beta}\,\Psi_{\beta}(E), \tag{4}$$

using the continuum wavefunctions Ψ_{β}(E), leading to the ro-vibrational level of the CO fragments indicated by β, where $V_{\mathrm{n}\beta}$ and Γ_{n} are defined as $V_{\mathrm{n}\beta} = \left\langle \phi_{\mathrm{n}} \middle| \mathbf{H} \middle| \Psi_{\beta}(E) \right\rangle$ and $\Gamma_n = 2\pi \sum_{b} \left| V_{n\beta} \right|^2$, respectively. Using $V_{\mathrm{n}\beta}$ and Γ_{n}, the overlap matrix can be rewrite as

$$\mathrm{O}_{\mathrm{mn}} = \frac{2\pi}{\left(\Gamma_{\mathrm{m}}\Gamma_{\mathrm{n}}\right)^{\frac{1}{2}}} \sum_{\beta} V^{*}_{m\beta}\, V_{n\beta} \,. \tag{5}$$

When $O_{mn} = 0$ ($m \neq n$), the two resonance states, m and n, can be treated separately as the isolated ones, and the total cross section can be expressed as the superposition of the resonance profiles represented by Eq. (1). On the other hand, when $O_{mn} \neq 0$ ($m \neq n$), the resonance states interact with each other through the overlapping of their continuum components.[17,18] If the values of O_{mn} for all m and n ($m \neq n$) are equal to 1, the continuum state coupled to the two resonance states, m and n, are completely identical. For this special case, the total cross-section can be expressed as

$$\sigma = \sigma_{bg} + \sigma_a \frac{\left[1 + \sum_n q_n \Gamma_n / 2(E - E_n)\right]^2}{1 + \left[\sum_n \Gamma_n / 2(E - E_n)\right]^2}, \qquad (6)$$

which is a Fano type profile for coupling among two or more than two resonance states and one continuum state.[16,17] When q_n and $q_{n'}$ of two adjacent resonances have the same sign, the total cross section in the energy range between the two resonances shows a destructive sum and that in the outside range of the two resonances shows a constructive sum. On the other hand, when q_n and $q_{n'}$ have the different signs, the total cross section shows a constructive sum in the inside range and a destructive sum in the outside range.[17]

In order to evaluate the overlap matrix element, O_{mn}, which takes a value between 0 and 1, the knowledge of the phase and the magnitude of the interaction, $V_{n\beta}$, need to be known.[17] Although the magnitude of $V_{n\beta}$ can in principle be estimated from the product state distributions of CO fragments, the phase of $V_{n\beta}$ could not be determined. Because no estimate has been known for $V_{n\beta}$, the simulations of the spectral feature was

preformed assuming either of the two extreme values of $O_{v^*v'^*}$ = 0 and 1 (for all $v^* \neq v'^*$). The purpose of the simulation is not to determine values of a lot of parameters such as q_{v^*}, E_{v^*}, and Γ_{v^*}, but to confirm whether the weak feature identified in the present study is due to the new resonances different from the main ones.

In the limit of the isolated resonances, i.e. $O_{v^*v'^*} = 0$, the parameters, q_{v^*}, E_{v^*}, and Γ_{v^*} (v^* = 0-6) were determined by fitting the respective observed peaks in main resonances to Eq. (1), and then, σ_{v^*} and σ_b values were calculated. On the other hand, in the case of $O_{v^*v'^*} = 1$, the simulation was performed for the entire energy region of the spectrum. Throughout the trial-and-error simulations for both of the extreme cases, it was found that the observed weak features between the main peaks could not appear as an interference effect of the main resonances. Therefore, it is suggested that the weak features in the tail region of the main resonance peaks identified in the present study are caused by a new type of resonances different from the main resonances. It can be noticed that these weak resonances could form a progression with spacing similar to the main progression. Therefore, these small peaks could be assigned to the transition to combination resonance levels, (v^*, s^*), where the second quantum number, s^*, stands for that of the vibrational motion along the direction perpendicular to the motion responsible for forming the main progression of the resonances. By adopting this notation the main resonances can be represented as the transitions to (v^*, 0) levels.

An example of the simulated spectra is shown in Fig. 3(b). In this simulation, all the off-diagonal elements of the overlap matrix are assumed to be equal to 1. For the main resonance features, the peak positions, E_n, and widths, Γ_n, were fixed to the observed values, respectively, and q_n were set to be proportional to the observed peak height. For the weak resonance features, E_n, Γ_n, and q_n, were adjusted by a trial-and-

error procedure. The parameters used in the simulation shown in Fig. 3(b) are listed in Table I. The set of parameters listed in this table is just one of a large number of the possible parameter sets. Similarly, even if all O_{mn} $(m \neq n) = 0$, the weak features appear in the simulated spectrum as shown in Fig. 3(c), in which the parameters listed in Table II are used.

B. Nuclear motion responsible for the weak resonances

As described in Ref. 8, the main resonance progression can be assigned to that of the in-phase stretching of the C-S and C-O bonds. Either of two quasi-bound nuclear motions different from the in-phase motion would be responsible for the weak resonances. One is the bending motion perpendicular to the dissociative coordinate and the other is the out-of-phase stretching along the dissociation coordinate. If the motion along the dissociation coordinate causes the weak resonances, the existence of a barrier along the dissociation coordinate is expected.[10,19]

Because the energy difference between the two resonances, (v*, 0) and (v*, s*), defined as $\Delta E_{v^*} \equiv E_{(v^*, s^*)} - E_{(v^*, 0)}$, corresponds to the frequency of the vibrational mode whose vibrational quantum numbers are represented by s*, it is expected to have information on the assignment. The observed energy differences, ΔE_{v^*}, for v* = 0 to 4 are 111(30), 203(25), 403(25), 588(32), and 564(16), respectively. As plotted in Fig. 4(a), ΔE_{v^*} increases as v* increases from v* = 0 to 3. Such an increase of ΔE_{v^*} suggests that the potential well along the quasi-bound vibrational coordinate becomes deeper as v* increases from 0 to 3.

If the weak resonances are caused by the out-of-phase stretching, i.e. the motion along the dissociation coordinate, the larger ΔE_{v^*} could be realized for the higher

potential barrier along the dissociation coordinate. Since the ΔE_{v^*} value increases as v* increases from 0 to 3, the dissociation lifetimes are expected to become larger when adopting these assignments. However, the observed peak widths of the resonant states, (v*, 0) becomes larger with v* increasing from 0 to 3, suggesting that the lifetime of the quasi-bound resonances becomes shorter. This is inconsistent with the above discussion based on the ΔE_{v^*} values. Therefore, it is unlikely that the weak resonances in the spectrum are caused by the out-of-phase stretching along the dissociation coordinate.

It should be noted that the well depth along the bending coordinate perpendicular to the dissociation coordinate is not directly correlated to the dissociation lifetime. Therefore, it is possible that the bending motion shows the weak resonances without the inconsistency between the dissociation lifetimes and the ΔE_{v^*} values. When the weak resonance can be assigned to the bending vibration, the quantum number of the bending mode, s*, has to be even in view of the molecular symmetry, i.e. the Franck-Condon integral between the bending states with the odd quantum numbers and the state of v = 0 in the electronic ground state is vanished. Therefore, the quantum number, s*, would be equal to 2. However, since the overlapping resonances might cause the mixing among the zero-order quasi-bound states, it might not be appropriate to assign to the state using a single set of quantum numbers, (v*, s*). In our previous study, it was found that the efficient rotational excitation of the CO fragments (v_{CO} = 1) occurs when the dissociation proceeds via the resonance states, (v* = 0 - 2, s* = 0).[9] Since the rotational excitation of the CO fragment is promoted by the bending excitation of OCS,[10] the bending vibration contributes to the resonance state of OCS on the $2^1\Sigma^+$ PES. The dissociation via the bend excited resonances with s* = 2 may promote further

rotational excitation of the CO fragments.

IV. Conclusion

The two-photon PHOFEX spectrum in the entire energy region of the $2^1\Sigma^+$-$1^1\Sigma^+$ band of OCS was measured and the weak features were identified between the strong main resonances. On the basis of the trial-and-error simulation of the excitation spectrum, it was confirmed that these weak features could not be attributed to a interference pattern caused by the overlapping of the strong resonances.

From the correlation between the well depth of the potential along the quasi-bound vibration responsible for the weak resonances and the dissociation lifetime of the main resonance states, it was suggested that the progression of the weak resonances could be attributed to the bending vibration.

References

[1] J. W. Rabalais, J. M. McDonald, V. Scherr, and S. P. McGlynn, Chem. Rev. 71 (1971) 73.

[2] M. I. McCarthy and V. Vaida, J. Phys. Chem. 92 (1988) 5875.

[3] G. Black, R. L. Sharpless, T. G. Slanger, and D. C. Lorents, J. Chem. Phys. 62 (1975) 4274.

[4] C. D. Pibel, K. Ohde, and K. Yamanouchi, J. Chem. Phys. 101 (1994) 836.

[5] K. Yamanouchi, K. Ohde, and A. Hishikawa, Adv. Chem. Phys. 101 (1995) 789.

[6] K. Ohde, A. Hishikawa, and K. Yamanouchi, J. Electron Spectrsc. Relat. Phenom. 79 (1995) 433.

[7] K. Yamanouchi, K. Ohde, A. Hishikawa, and C. D. Pibel, Bull. Chem. Soc. Jpn. 68 (1995) 2459.

[8] A. Hishikawa, K. Ohde, R. Itakura, S. Liu, K. Yamanouchi, and K. Yamashita, J. Phys. Chem. A 101 (1997) 694.

[9] R. Itakura, A. Hishikawa, and K. Yamanouchi, J. Chem. Phys. 113 (2000) 6598.

[10] R. Schinke, Photodissociation dynamics (Cambridge University Press, New York, 1993).

[11] R. T. Pack, J. Chem. Phys. 65 (1976) 4765.

[12] E. J. Heller, Acc. Chem. Res. 14 (1981) 368.

[13] J. R. Huber and R. Schinke, J. Phys. Chem. 97 (1993) 3463.

[14] B. R. Jhonson and J. L. Kinsey, Phys. Rev. Lett. 62 (1989) 1607.

[15] B. R. Jhonson and J. L. Kinsey, J. Chem. Phys. 91 (1989) 7638.

[16] U. Fano, Phys. Rev. 124 (1961) 1866.

[17] F. H. Mies, Phys. Rev. 175 (1968) 1968.

[18] K. Someda, H. Nakamura, and F. H. Mies, Chem. Phys. 187 (1994) 195.

[19] H. U. Suter, J. R. Huber, M. von Dirke, A. Untch, and R. Schinke, J. Chem. Phys. 96 (1992) 6727.

Table I. The values of the parameters used in the simulation of the O_{mn} = 1 case (Fig. 3(b)).

Resonant state	E_n / cm^{-1}	Γ_n / cm^{-1}	q_n
(0, 0)	64741	51	68
(0, s*)	64852	300	35
(1, 0)	65604	106	84
(1, s*)	65807	300	35
(2, 0)	66381	214	96
(2, s*)	66784	300	36
(3, 0)	67130	195	77
(3, s*)	67718	200	25
(4, 0)	67900	187	58
(4, s*)	68464	100	15
(5, 0)	68644	100	34
(5, s*)	69000	100	10
(6, 0)	69375	100	25

Table II. The values of the parameters used in the simulation of the $O_{mn} = 0$ case (Fig. 3(c))..

Resonant state	E_n / cm^{-1}	Γ_n / cm^{-1}	q_n
(0, 0)	64740	37	-26
(0, s*)	64860	100	-12
(1, 0)	65613	93	-3.2
(1, s*)	65840	200	-22
(2, 0)	66400	209	-10
(2, s*)	66800	200	-28
(3, 0)	67120	194	8.7
(3, s*)	67680	150	25
(4, 0)	67905	151	31
(4, s*)	68425	100	15
(5, 0)	68643	308	53
(5, s*)	69140	150	22
(6, 0)	69363	120	49

Figure Captions

Fig. 1. (a) The VUV-PHOFEX spectra measured under jet-cooled conditions. A solid line shows the spectrum obtained by using a LiF prism adjusted during the measurement. A dotted line shows the spectrum obtained using a LiF prism which was optimized at the peak wavelength of the spectrum and was fixed during the measurement. (b) The comparison between the VUV-PHOFEX spectrum (open circles) and the two-photon PHOFEX spectrum (a solid line).

Fig. 2. The schematic diagram of the experimental setup for the PHOFEX measurement by the UV two-photon excitation.

Fig. 3. (a) The observed PHOFEX spectrum in the entire region of the $2^1\Sigma^+$-$1^1\Sigma^+$ band of OCS by the UV two-photon excitation. (b) The simulated spectrum when all O_{mn} are assumed to be equal to be 1. (c) The simulated spectrum when all O_{mn} ($m \neq n$) are assumed to be equal to be 0.

Fig. 4. (a) The energy differences between the two peak position of the resonances (v*,0) and (v*, s*); $\Delta E_{v^*} = E_{(v^*,s^*)} - E_{(v^*,0)}$. (b) The peak width (FWHM) of the resonant states, (v*, 0).

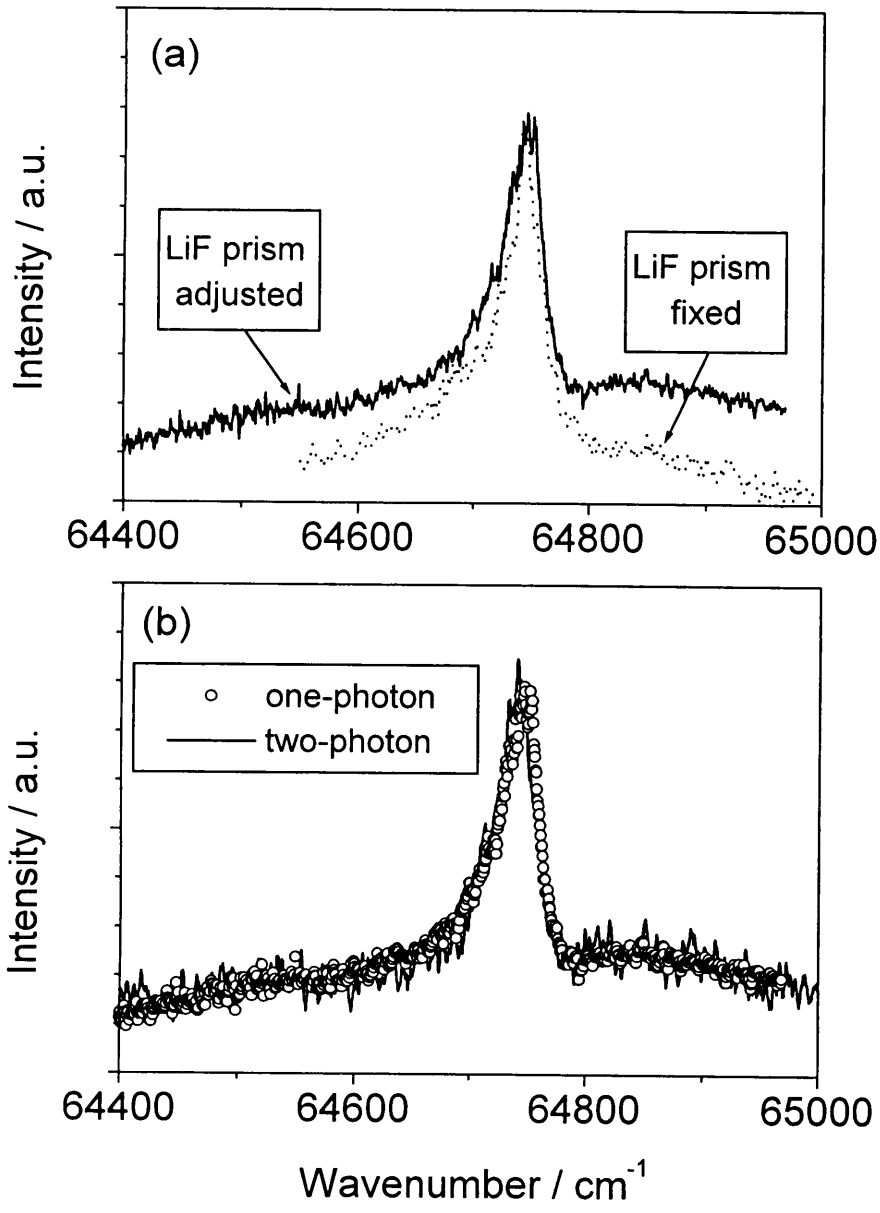
(a)
LiF prism adjusted
LiF prism fixed
Intensity / a.u.
64400
64600
64800
65000
(b)
one-photon
two-photon
Intensity / a.u.
64400
64600
64800
65000
Wavenumber / cm-1

Fig. 1

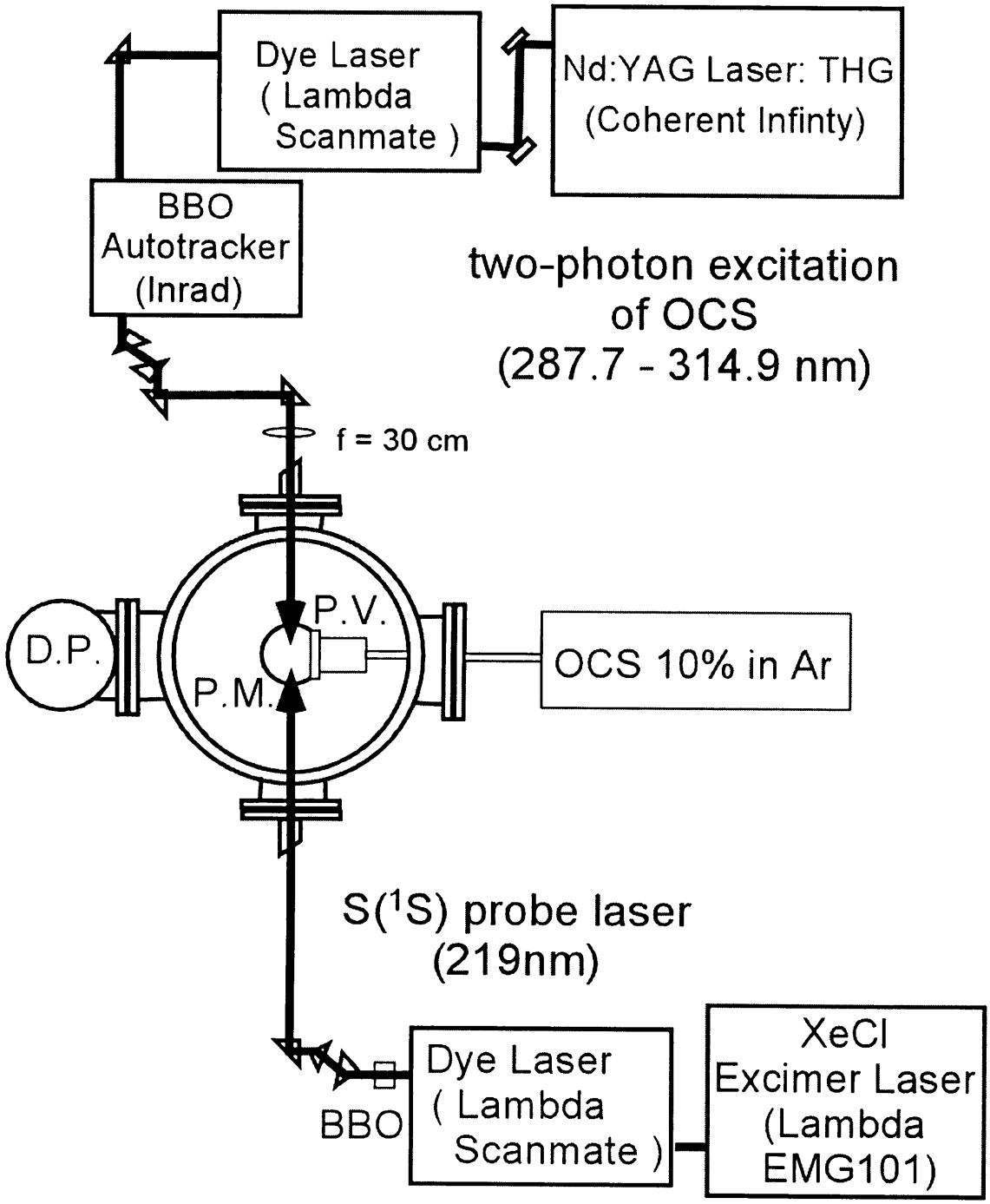
Dye Laser
(Lambda
Scanmate)
Nd:YAG Laser: THG
(Coherent Infinty)
BBO
Autotracker
(Inrad)
two-photon excitation
of OCS
(287.7 - 314.9 nm)
f = 30 cm
P.V.
D.P.
P.M.
OCS 10% in Ar
S(1S) probe laser
(219nm)
BBO
Dye Laser
(Lambda
Scanmate)
XeCl
Excimer Laser
(Lambda
EMG101)

Fig. 2

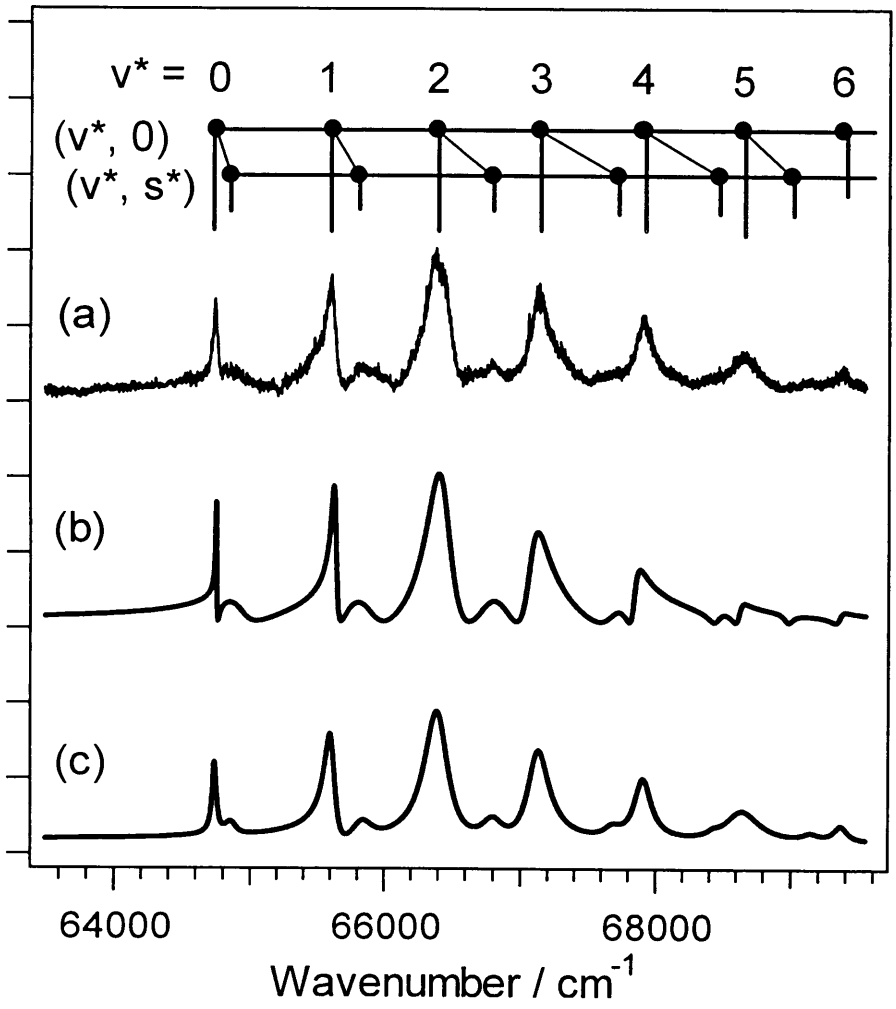

Fig. 3

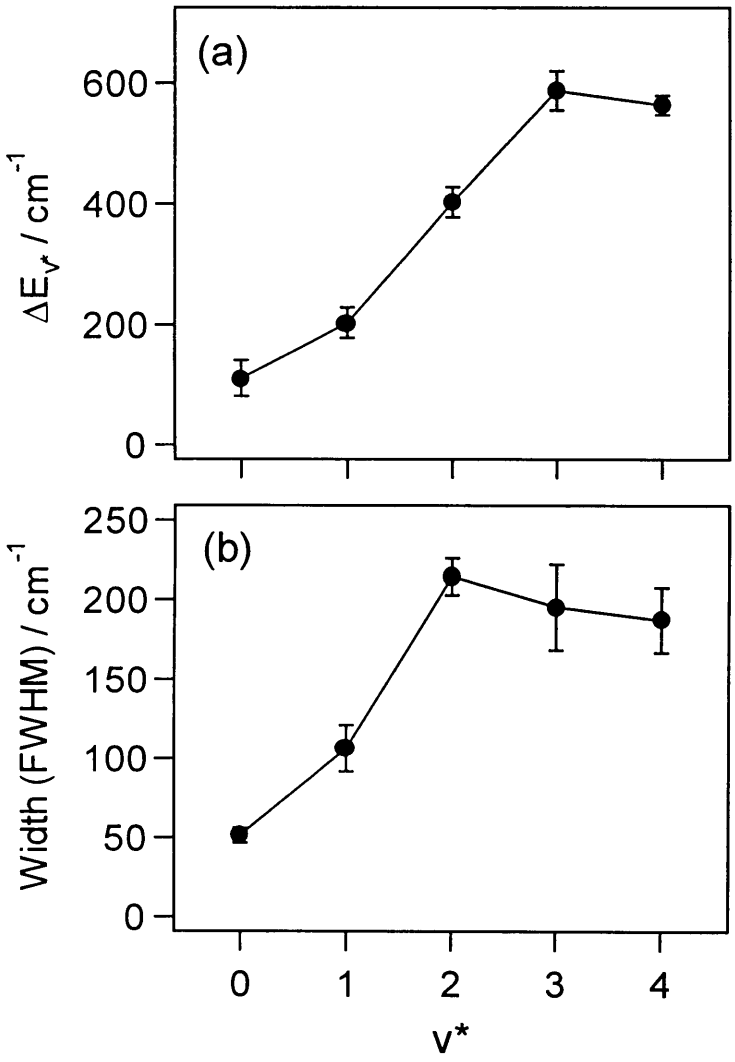
(a)
600
400
200
0
ΔE_{v^*} / cm^{-1}
(b)
250
200
150
100
50
0
Width (FWHM) / cm^{-1}
0
1
2
3
4
v*

Fig. 4

Chapter 4

Ionization and fragmentation dynamics of benzene in intense laser fields by tandem mass spectroscopy

Abstract

Using a tandem time-of-flight mass spectrometer, mass-selected benzene cations produced by the resonantly enhanced multiphoton ionization are exposed to intense laser fields (~ 2×10^{16} W / cm^2) at λ ~ 790 and 395 nm with the pulse duration of ~ 50 fs. Comparing the yields of the product ions with those obtained from neutral benzene molecules, the ionization and dissociation dynamics of benzene in intense laser fields is investigated. At λ ~ 790 nm, the formation of parent benzene ions is a dominant process irrespective of the initial charge states, i.e., major products obtained when starting from neutral benzene are benzene cations and dications, and those obtained when starting from benzene cation are benzene dications. On the other hand, at λ ~ 395 nm, the fragmentation processes to produce $C_4H_i^+$ (i = 2 – 4) and $C_3H_j^+$ (j = 1 – 3) dominate over further ionization to the benzene dication for both cases starting from neutral benzene and benzene cation, indicating the population trapping occurs by the efficient confinement in the light-induced mixture of the $\tilde{C}$ and $\tilde{X}$ states of benzene cations assisted by the ultrafast intramolecular decay process.

I. Introduction

Molecules in intense laser fields are known to exhibit a variety of nuclear dynamics[1,2] such as alignment of a molecular axis along the laser polarization direction[3] and ultrafast structural deformation.[4-7] The ultrafast structural deformation has often been interpreted by referring to the formation of light-dressed potential energy surfaces[1,8,9] by the coupling among electronic states of molecules, but it has been uncertain whether such a strong coupling for the formation of the light-dressed states occurs at the neutral stage, the singly charged stage, or the multiply charged stage when neutral molecules are exposed to intense laser fields.

It should be an important issue to clarify at which stage an efficient coupling occurs to form a time-dependent light-dressed potential energy surface, which induces the ultrafast structural deformation. Theoretical investigations were performed recently to account for the experimental findings. For example, nuclear dynamics of the singly and multiply charged cations such as N_2^{3+},[10] CO_2^+, and CO_2^{2+}, [11] in intense laser fields was investigated on the theoretical potential energy surfaces. Experimentally, the dynamics of H_2^+ in intense laser fields was investigated by preparing H_2^+ by a plasma discharge ion source before the intense laser pulses were introduced.[12] In the present study, we introduce a new approach in which molecular ions are selectively prepared in specific vibrational states by a resonantly enhanced multiphoton ionization (REMPI) scheme, and the mass-and-state-selected ions are exposed to the intense laser pulses using a tandem time-of-flight (TOF) mass spectrometer.

As a target molecule, we chose benzene because its behavior in laser fields has been intensively studied by the laser pulses with wide ranges of temporal width (10^{-8} –

10^{-14} s), wavelength (IR − UV), and intensity ($10^{6}-10^{17}$ W/cm^2) as summarized in Table I, and its dissociation and ionization processes have been known to depend sensitively on the condition of the laser pulses.

When femtosecond laser pulses (50 − 200 fs) are employed, the ionization and dissociation processes are qualitatively different from those in the long pulsed laser fields. When $\lambda \sim 800$ nm with the laser fields intensity of ~10^{13} W/cm^2, benzene cations are the main product ions from the neutral benzene.[13,14] When the laser field intensity was in the $10^{14}-10^{15}$ W/cm^2 range, three different results were reported. First, Ledingham *et al.*[15,16] showed that the benzene cations were mainly observed, and the benzene dications were the second major products, and that the triply charged benzene cations began to appear when the laser intensity reached ~ 10^{15} W/cm^2. In these cases fragmentation processes were identified as minor channels.[16] Secondary, Talebpour *et al.*[17] showed that benzene cations were dominant product ions regardless of the laser field intensities ranging from 1×10^{13} to 2×10^{14} W/cm^2. In their report, when the laser field intensity was in the range of $1\times10^{13}-5\times10^{13}$ W/cm^2, $C_4H_i^+$ (i = 2 – 4) fragments exhibited the largest yields next to the dominant benzene cations. As the laser field intensity increased up to 2×10^{14} W/cm^2, the yields of benzene dications and other fragment ions such as $C_3H_j^+$ (j = 0 – 3), $C_2H_k^+$ (k = 0 - 4), and CH_l^+ (l = 0, 1), became comparable with those of $C_4H_i^+$. Thirdly, Castillejo *et al.*[18] reported that the fragment ions, such as $C_3H_j^+$, $C_2H_k^+$, and CH_l^+, were major products when the laser field intensity exceeded 10^{14} W/cm^2. In the much higher intensity range of ~ 10^{17} W/cm^2, Shimizu *et al.*[19] reported that singly and multiply charged atomic ions were dominant fragment ions, indicating that the Coulomb explosion was a major process.

The wavelength dependence of the ionization and dissociation of benzene in

intense short-pulsed light fields was recently showed by Smith *et al.*[16] Interestingly, when the intense femtosecond laser pulses of $\lambda \sim 375$ nm were used, the multiple ionization to the benzene dication was significantly suppressed and the yields of the fragment ions, $C_4H_i^+(i = 2 - 4)$, became largest next to the benzene cation, exhibiting a marked contrast with the results when $\lambda \sim 750$ nm.[16] In the present study, we focus our attention to this characteristic wavelength dependence of the dynamics of benzene in ultrashort intense laser fields and investigate whether this difference reflects the dynamics in neutral manifold or that in the singly charged or multiply charged manifold.

II. Experiment

Using a mode-locked Ti-sapphire laser (Coherent, Mira Seed) pumped by a frequency-doubled output of a diode-laser pumped Nd:YVO_4 laser (Spectra-Physics, Millennia), femtosecond laser pulses (λ = 785 nm, FWHM = 50 nm) were generated. Output pulses from Mira were introduced to a regenerative amplifier (B. M. Industries, Alpha10), and amplified by the chirped-pulse amplification. The regeneratively amplified laser pulses (λ = 790 nm, FWHM = 22 nm, 10 Hz) were amplified further by two stages of a bow-tie-type amplifier. After the compression, intense laser pulses with a maximum power of around 30 mJ/pulse were obtained. The temporal width (FWHM) of a laser pulse was $\leq$ 50 fs, which was measured by a single-shot auto-correlator (B. M. Industries, AM100). The fs laser pulses at 395 nm were obtained by frequency doubling of the amplified Ti-sapphire output by a β-BBO crystal (1mm thick) after the compression stage. The maximum power of the fs pulses at $\lambda \sim 395$ nm was ~ 10 mJ/pulse. By taking account of the temporal broadening of the laser

pulses by the dispersion in a β-BBO crystal, the temporal width (FWHM) of the frequency-doubled laser pulses at λ ~ 395 nm was estimated to be ~ 42 fs. The laser beam was focused by a quartz lens (f =150 or 200 mm) to generate intense laser light fields, and the direction of the laser polarization was set to be parallel to that of the detection axis of the mass spectrometers.

We need to be careful about non-linear distortions of laser pulses caused by a self-phase modulation and a self-focusing as pointed out by Müller *et al.*[20] They investigated the ionization and dissociation of toluene, and showed that the fragmentation was significantly enhanced when the laser beam was intentionally distorted. In the present study, in order to avoid the beam distortion, the focusing quartz lens was located just outside the window of the vacuum chamber so that the photon density at the window was kept sufficiently low. The distance between the lens and the window was set to be less than 1 cm.

The schematic diagram of a custom made TOF spectrometer (R. M. Jordan Co.) is shown in Fig. 1. The benzene vapor mixed with the He carrier gas (1 atm) was expanded into the vacuum chamber through a pulsed nozzle and collimated through a skimmer (1 mm ϕ). The frequency-doubled output (λ = 258.9 nm) of a dye laser (Lambda Physik, FL3002) pumped by a XeCl excimer laser (Lambda Physik, LPX 105i) was used to produce benzene cations in the electronic ground state by the (1+1) REMPI scheme from neutral benzene molecules via the ν_6 = 1 level in the S_1 ($^1B_{2u}$) state.

At the first stage of the tandem TOF mass spectrometer, the benzene cations were accelerated at around 4 keV by three parallel electrode-plates with Wiley-McLaren condition[21] so that the cations were spatially focused at the second interaction point after

the flight through the field free region of 1 m length. An ion lens collimated the accelerated ion beam whose direction was adjusted by two ion-deflectors for horizontal and vertical deflections. The second stage of the tandem TOF spectrometer is composed of four parallel electrode-grids as shown in Fig. 1. The ion beam was decelerated in the region between the grounded entrance-grid and the second-grid with a voltage of 1400 V. When the mass-selected cations reached the equidistant point between the second-grid and the third-grid, they were exposed to intense laser pulse fields generated by focusing the output of the regenerative amplifier by a quartz lens (f = 200 mm).

In order to repel ions originated from the residual gases in the direction opposite to the detector, the voltage of the third grid was set to be higher by 100 V than that of the second grid. Under this voltage condition, only the benzene cations produced by the REMPI scheme in the first stage of the tandem TOF mass spectrometer were allowed to pass through the third grid. Finally, the multiply charged cations and fragment ions produced by the interaction between the intense laser pulses and the benzene cations were re-accelerated in the region between the third grid and the exit-grid having a ground level potential. After drifting in the field-free region of the 1 m length, the ions hit the MCP detector. The signals from the MCP detector were stored and averaged over more than 1×10^3 shots by a digital oscilloscope (Lecroy, 9384) with a 1 GHz sampling rate as a form of a TOF mass spectrum.

Assuming that the laser spatial profile has a Gaussian distribution and the focusing condition reaches a diffraction limit, the diameter of the focal spot, $2d$, is calculated to be 26 μm at the laser wavelength of 790 nm and 13 μm at the laser wavelength of 395 nm. The peak intensities of laser fields at the focal point were set to be around 25

PW/cm^2 (PW = 10^{15} W) at both wavelengths.

The main chamber was pumped by a turbo molecular pump with a pumping rate of 550 *l* /s (Varian, V550) backed up by an oil-free scroll pump (Anest-Iwata ISP-250; 250 *l* /min). The first and second TOF tubes were pumped separately by two turbo molecular pumps with a pumping rate of 250 *l* /s (Varian, V220) both of which were backed up by another oil-free scroll pump (Anest-Iwata ISP-250; 250 *l* /min). When the pulsed nozzle was operated, the pressure in the main chamber was around 1×10^{-5} Torr and that in the second TOF tube which was pumped differentially was around 5×10^{-8} Torr. The pressure in the second TOF chamber was kept sufficiently low, and neither collision-induced process nor space charge effect was identified.

A conventional linear TOF mass spectrometer[22-24] was also used to record the TOF mass spectra for neutral benzene molecules. The pure benzene vapor (0.6−3 Torr) was expanded into the vacuum chamber through the pulsed nozzle. The pressure range in the main chamber was between $2\times10^{-8}-6\times10^{-8}$ Torr during the nozzle operation. The molecular beam of neutral benzene molecules was collimated by a skimmer (1 mm ϕ) and was exposed to the intense laser fields generated by focusing the short-pulsed laser output by a quartz lens (f = 150 mm). The peak intensities of the laser fields at the focal point were set to be around 20 PW/cm^2 for both wavelengths of 790 nm and 395 nm.

III. Results and Discussion

A. Neutral benzene in intense laser fields

The TOF spectra obtained when neutral benzene molecules were irradiated by intense laser pulses at λ ~ 395 and 790 nm are presented in Figs. 2(a) and 2(b),

respectively. The main product ions were benzene cations at both laser wavelengths, but the yields of other product ions exhibited clear wavelength dependence, as summarized in Table II. The relative yields of the ion species were evaluated by measuring the area of the corresponding peaks in the TOF mass spectra. Although $C_6H_6^{2+}$ and $C_3H_3^+$ have the same mass-to-charge ratio, m/q = 39, they can be distinguished from each other in the present case by the extent of spread of their peak profile. That is, the peak originating from $C_3H_3^+$ should be broadened by the kinetic energy release after the dissociation from the benzene cation, while that originating from $C_6H_6^{2+}$ should appear as a sharp peak.

When the laser wavelength was 395 nm, the yields of $C_4H_i^+$(i = 2 – 4) were largest next to the benzene cation. Because the width of the peak at m/q = 39 (FWHM: 14.4(4) ns) in the TOF mass spectrum was much broader than that of the benzene cations (FWHM: 3.2(1) ns), the peak at m/q = 39 was mainly ascribed to $C_3H_3^+$. The present interpretation would also be confirmed by the experiment using deuterated benzene, C_6H_5D, whose dication has a half-integer mass-to-charge ratio, m/q = 79 / 2.[15] As clearly seen in Fig. 2(a), the yields of the fragment ions tend to become smaller as their size becomes smaller.

On the other hand, when the wavelength was 790 nm, the width of the peak at m/q = 39 (FWHM: 3.8(1) ns) in the TOF mass spectrum was even narrower than that of the benzene cations (FWHM: 4.7(1) ns). Therefore, this peak with no kinetic energy spread could be regarded as the peak originating mainly from the benzene dications. The formation of the benzene dications when $\lambda \sim 790$ nm was previously confirmed by Ledingham *et al.*[15] using 50 fs laser pulses for C_6H_5D. The yields of benzene dications and carbon atomic cations were largest next to the benzene cation, and $C_4H_i^+$ fragments

were identified with only very weak intensities.

These observations of the efficient fragmentation at $\lambda \sim 395$ nm, and the multiple ionization to form benzene dications at $\lambda \sim 790$ nm are consistent with the results obtained by Smith *et al.*[16] and Ledingham *et al.*[15] using the femtosecond laser pulses whose width is shorter than 100 fs with the field intensity range of $10^{13}-10^{15}$ W/cm^2. Contrary, the results obtained by Castillejo *et al.*[18] exhibited an excessive fragmentation into smaller fragment ions when $\lambda \sim 800$ nm even though the pulse width employed were almost the same as ours. This discrepancy of the behavior of benzene in intense short-pulsed laser fields may be ascribed to the distortion of the laser profile in their experiment as suggested by Müller *et al.*[20]

It has been known that as the laser intensity increases a qualitative transition of the ionization mechanism from the multiphoton ionization to the field-induced tunnel ionization occurs. The Keldysh adiabaticity parameter, γ,[25] has been used as a criterion to judge whether the ionization occurs via the field-induced tunneling or the multiphoton absorption. This parameter is defined as the ratio of the optical field frequency, ω, to the tunneling rate of the ionized electron, ω_t, i.e., $\gamma = \omega / \omega_t$. When the laser field intensity is 10^{16} W/cm^2, the Keldysh parameter can be calculated as $\gamma = 0.12$ and 0.24 for $\lambda \sim 790$ and 395 nm, respectively. As represented by these γ values, the tunnel ionization is expected to be enhanced more when $\lambda \sim 790$ nm than when $\lambda \sim 395$ nm, which might explain the efficient formation of the benzene dication when $\lambda \sim 790$ nm.

In the Keldysh model, the tunneling rate of an electron tends to be underestimated because of the assumption of the zero-range potential, leading to the overestimation of the adiabaticity parameter.[26] Therefore, the adiabaticity parameters derived after the

correction of the tunneling rate would become even smaller than the aforementioned γ values, indicating an efficient tunnel ionization.

Within the multiphoton ionization picture, the number of the photons, N, required to reach the second ionization threshold[27] of 26.4 eV to produce benzene dications is N = 9 when $\lambda \sim 395$ nm, which is around one half of the corresponding photon number, N = 17, when $\lambda \sim 790$ nm. Therefore, the larger yield of benzene dications for $\lambda \sim 395$ nm is expected than that for $\lambda \sim 790$ nm with the same photon flux, which is realized when the laser intensity at $\lambda \sim 395$ nm is twice as large as that at $\lambda \sim 790$ nm. However, even when the laser intensity of $\lambda \sim 395$ nm was doubled, the fragmentation process was found to dominate over the formation of dications. Considering that singly charged cations were observed with strong intensities when $\lambda \sim 395$ nm, there should exist a mechanism by which the population in the cation stage is efficiently trapped when $\lambda \sim 395$ nm.

At both laser wavelengths of 395 and 790 nm, the atomic carbon ions, C^+, were observed as shown in Fig. 2. According to the previous studies the C^+ ions could be produced from benzene in intense laser fields through the Coulomb explosion from the multiply charged benzene cations or through the "ladder switching" processes in which photoabsorption and dissociation of fragments are repeated sequentially leading to smaller sized fragments. After scaling the TOF mass spectra of C^+ with respect to the released momenta, momentum-scaled TOF spectra of C^+ at $\lambda \sim 395$ and 790 nm were obtained as shown in Figs 3(a) and 3(b), respectively. By assuming a Gaussian momentum distribution for these peaks, their widths (FWHMs) were determined by a least squares fit to be $223(7)\times10^3$ and $274(6)\times10^3$ amu m/s at $\lambda \sim 395$ and 790 nm, respectively.

It should be noted that the atomic carbon cations, C^+, exhibit much broader peaks in the momentum-scaled TOF spectra than other fragment ions. For example, the FWHMs of the peaks for $C_4H_4^+$ and $C_3H_3^+$ at $\lambda \sim 395$ nm were $35.4(8)\times10^3$ and $34.5(1)\times10^3$ amu m/s , respectively, and that for $C_4H_4^+$ at $\lambda \sim 790$ nm was $40.0(6)\times10^3$ amu m/s. The large momentum release for the C^+ ions suggests that there is an ultrafast tunnel ionization process at both $\lambda \sim 395$ and 790 nm to form highly multiply charged benzene cations, which break into the atomic fragment ions by the Coulomb explosion processes. Such a large kinetic energy release of C^+ could not be expected for unimolecular dissociation of molecular fragment ions originating from benzene cations. On the other hand, the relatively small kinetic energy release of the molecular fragments such as $C_3H_3^+$ suggests that they were mainly produced from the unimolecular dissociation rather than the Coulomb explosion.

The above observation that the momentum spread of C^+ at $\lambda \sim 395$ nm is smaller by 19 % than that at $\lambda \sim 790$ nm indicates that the Coulombic repulsive force is larger at $\lambda \sim 790$ nm than at $\lambda \sim 395$ nm. Therefore, it is possible that (i) the ionization to the higher charged benzene cations at $\lambda \sim 790$ nm occurs more efficiently and/or that (ii) the structural deformation such as elongation of the C-C and C-H bond distances occurs to a larger extent at $\lambda \sim 395$ nm to reduce the Coulombic repulsive force.

Another atomic fragment ion, H^+, could also be produced in the Coulomb explosion process, but the H^+ signal originating from benzene were overlapped by that from background H_2O under the present experimental conditions. Therefore, the H^+ signal could not be used for the discussion of the Coulomb explosion of benzene molecules.

It would be interesting to note that highly multiply charged benzene cations were

not identified either at 395 nm or at 790 nm, while a non-negligible benzene molecules undergo the multiple tunnel ionization, leading to the Coulomb explosion. Even though a definitive interpretation may not be possible, this finding suggests that there is a fate determining stage in the ionization process. When $\lambda \sim 790$ nm, it can be inferred that once a situation in which three electrons are successively ejected is realized, a further tunnel ionization efficiently occurs to reach the highly charged stage. A similar situation may also exist when $\lambda \sim 395$ nm. However, an additional complexity exist at this wavelength because no benzene dication was observed and the singly charged fragment ions were produced.

B. Benzene cation in intense laser fields

Using the tandem TOF mass spectrometer, the TOF mass spectra shown in Figs. 4(a) and 4(b) were obtained respectively by irradiating the mass-selected benzene cations with the intense laser pulses at $\lambda \sim 395$ and 790 nm. The small amount of fragment ions were produced as by-products at the first laser-molecule interaction point, where benzene cations were prepared by a nanosecond laser pulse through the REMPI process, but their flight time was largely different from that of the corresponding ions produced at the second interaction point. Therefore, they did not interfere with the TOF mass spectrum starting from the benzene cations. Benzene dications and $C_3H_3^+$, which have the same mass-to-charge ratio, $m/q = 39$, were discernible to each other by the peak widths in the TOF spectra, as described in Sec. III. A.

When $\lambda \sim 395$ nm, $C_4H_i^+$ (i = 2 – 4) fragment ions were observed as the major products, while $C_3H_j^+$ (j = 3) fragment ions were observed with much weaker intensities, i.e., the total yields of $C_3H_j^+$ estimated by the peak area in the TOF mass spectrum were

only 20 % of the total yields of $C_4H_i^+$. On the other hand, when $\lambda \sim 790$ nm, the fragment ions were hardly identified, and instead, benzene dications appeared with strong peak intensity. When the laser fields intensity was increased up to 6×10^{16} W / cm^2, the further ionization occurred and triply charged benzene ions began to appear in addition to the benzene dications. The carbon atomic cations, C^+, which were observed when starting from the neutral benzene molecules, were not identified either at 395 or 790 nm, probably due to their weak and spread feature.

For both laser wavelengths, the major products obtained when starting from benzene cations were the same as those having the largest yields next to the benzene cations when starting from neutral benzene molecules. This observation suggests that the ionization and dissociation dynamics starting from neutral benzene molecules is governed by the processes common to those starting from benzene cations except for the formation of the benzene cations. Therefore, the dynamics occurring at the benzene cation stage would be important for the characteristic fragmentation as well as for the suppression of the formation of doubly and multiply charged parent ions observed when $\lambda \sim 395$ nm.

After the REMPI preparation, the benzene cations are populated in the electronic ground $\tilde{X}\ ^2E_{1g}$ state whose electronic configuration is $\cdots(a_{2u})^2(e_{2g})^4(e_{1g})^1$. By absorbing a photon of $\lambda \sim 395$ nm (3.14 eV), benzene cations in the electronic ground state are excited resonantly to the electronically excited $\tilde{C}\ ^2A_{2u}$ state whose electronic configuration is $\cdots(a_{2u})^1(e_{2g})^4(e_{1g})^2$. In the photoelectron spectrum, the $\tilde{C}$ state is known to exhibit a diffuse structure with the bandwidth (FWHM) of as large as 0.5 eV.[28] This diffuse structure has been attributed to the dense discrete levels in the $\tilde{C}$ state appearing through the complex vibronic coupling.[29] Since the $\tilde{C} - \tilde{X}$ transition

is a strong dipole allowed transition between the two π orbitals, it is expected that the light-dressed potential energy surfaces are formed by the strong coupling between the $\tilde{C}$ and $\tilde{X}$ states by the laser fields of λ ~ 395 nm.

The time-dependent calculation of a nuclear wavepacket on the $\tilde{C}$ state potential energy surface[29] demonstrated that an initially prepared wavepacket decays very rapidly within 10 fs with no recurrence. This rapid decay was ascribed to an ultrafast intramolecular vibrational redistribution (IVR). It was also shown that the $\tilde{C}(^2A_{2u})$ state of benzene cations undergoes non-radiative internal conversion into the vibrationally highly excited region of the $\tilde{B}(^2E_{2g})$ and $\tilde{X}(^2E_{1g})$ states within 20 – 30 fs.[29] Therefore, it is possible that an ultrafast spread of the nuclear wavefunction occurs once the $\tilde{C}(^2A_{2u})$ state character is induced by the intense laser fields, and the ultrafast geometrical change lowers largely the ionization probability to reach the dication stage,[30] resulting in the effective population trapping within the cation stage.

Even when light-dressed states are formed through the strong coupling between the $\tilde{C}$ and $\tilde{X}$ states, the one-photon crossing[1,31-33], i.e. the crossing between the potential energy surface of the electronically excited state lowered by the one-photon energy and the potential energy surface of the electronic ground state, could not cause a bond breaking to produce $C_4H_i^+$and $C_3H_j^+$ because one-photon energy of the 395 nm light (3.14 eV) is lower than the threshold energies of 4.16 and 4.19 eV for producing $C_4H_4^+$ and $C_3H_3^+$, respectively.[34] However, under the strong laser fields generated in the present study, dynamics could proceed through three-photon crossing and/or even through a larger number-photon crossing. Therefore, benzene cations could gain the $\tilde{C}$ state character through such a multiphoton crossing and eventually carry a character of dissociative continuum assisted by the aforementioned ultrafast vibronic decay

mechanism. It would be possible that an appropriate nuclear configuration for the three-photon coupling is realized within the ultrashort laser pulse duration by the ultrafast IVR process within the $\tilde{C}$ state. It would also be possible that the populations trapped in the light-dressed potential energy surfaces by the $\tilde{C}$ and $\tilde{X}$ states are further excited to a dissociative electronically highly excited state, or ionized to a dissociative state of benzene dications.

When starting from the neutral benzene molecules, at the early stage of the $\tilde{C} - \tilde{X}$ coupling in the benzene cationic stage, a small portion of benzene cations could escape from the $\tilde{C} - \tilde{X}$ manifold by ionizing electrons to reach the highly charged stage. Therefore, the multiply charged benzene ions prepared by the $\lambda \sim 395$ nm laser light could carry an influence of the $\tilde{C} - \tilde{X}$ mixing as schematically shown in Fig. 5. On account of the $\tilde{C} - \tilde{X}$ mixing, the molecular skeletal structure is relaxed to give a smaller amount of the kinetic energy release of C^+ ions produced through the Coulomb explosion from the highly charged stage compared with those when $\lambda \sim 790$ nm, which is consistent with the observed profiles of momentum-scaled TOF spectra for the C^+ ions in Fig. 3.

It was previously reported that the population trapping occurs in the Rydberg states of atoms[35-38] and diatomic molecules[39] in intense laser fields. This type of trapping is caused by the resonances between the Rydberg states, which are energetically shifted by the ac Stark effect, and the electronic ground state. The mechanism of the population trapping in the benzene cation identified in the present study would be regarded as an IVR-assisted trapping, which is different from the Stark-assisted trapping in the Rydberg states.

On the other hand, in the laser light fields of $\lambda \sim 790$ nm, benzene dications and

trications were produced when starting from benzene cations, while benzene cations and dications were produced when starting from neutral benzene molecules. This efficient ionization suggests that there is no strong coupling among specific electronic states on either of the neutral, cation, and dication stages, and non-resonant multiple field-induced tunnel ionization dominates the dynamics in the intense laser fields of $\lambda \sim 790$ nm. It would be possible that trications were also produced when starting from neutral benzene molecules,[15] but the signal was too small to appear in the TOF mass spectral region where the ringing decay after the strong signal of a contaminant H_2O could hide a weak signal.

C. Difference in the fragmentation from neutral and cationic benzene

As described above, when neutral benzene molecules and benzene cations were irradiated by the intense 50 fs laser pulse of $\lambda \sim 395$ nm, major fragment ions were $C_4H_i^+$ and $C_3H_j^+$. When the laser intensity was 2×10^{16} W/cm^2, the yield ratio, R = $(C_3H_j^+)$ / $(C_4H_i^+)$, from neutral benzene molecules was R ~ 0.4. The ratio obtained from benzene cations, R ~ 0.2, is smaller than that from neutral benzene in spite of the larger laser intensity of 2.5×10^{16} W/cm^2.

When the benzene cations produced in the present study by the REMPI via $S_1(\nu_6 = 1)$, they were expected to be populated in the three vibrational states, $\nu = 0$, $\nu_6 = 1$, and 2, in the electronic ground state.[40] Therefore, when the prepared benzene cations were exposed to the intense 50 fs laser pulse at $\lambda \sim 395$ nm, the strong coupling between the $\tilde{C}$ state and the low vibrational states in the $\tilde{X}$ state would occur first.

The dissociation processes of benzene cations through the dense manifold of the vibrationally highly excited region of the electronic ground $\tilde{X}$ state were studied

previously by the statistical treatment of the multiple fragmentation steps.[41] The yield ratio R was found to increase as the internal energy imposed on the benzene cations increases, because the contribution of the multiple fragmentation into the smaller fragment ions increases as the internal energy of the benzene cation increases.

In view of the statistical picture, the larger R value obtained when starting from the neutral benzene molecules indicates that the cation stage from which the fragmentation into $C_4H_i^+$ and $C_3H_j^+$ occurs is expected to have a larger internal energy than the benzene cations prepared by the REMPI process. This means that the memory of the initial vibrational states is kept even after the strong resonance interaction between the $\tilde{C}$ and $\tilde{X}$ states in the intense laser fields. The low vibrational states of the benzene cations produced by the REMPI process tend to access to the lower energy manifold of the $\tilde{C}$ state compared with those reached from the neutral benzene molecules.

When starting from neutral benzene molecules, it is also possible that the re-scattering process[42] occurs, in which the ionized electron excites the molecular ion core within a laser pulse by transferring its ponderomotive energy,[20] resulting in the benzene cations having the larger internal energy than those prepared by the REMPI process.

D. Comparison with the experiment using longer laser pulses

The multiphoton ionization and dissociation of benzene were investigated previously using nanosecond laser light of $\lambda \sim 390$ nm.[43] The benzene cations prepared by the (2+1) REMPI led to an efficient fragmentation process, and the total yields of the fragment ions were much larger than the yield of benzene cations. It was also found that the yields depend strongly on the laser field intensity. When the laser intensity reached ~ 10^9 W/cm^2, the respective yields of $C_4H_i^+$ (i = 2 – 4), $C_3H_j^+$ (j = 0 –

3), $C_2H_k^+$ (k = 0 – 3), and C^+, were all 20 - 30 % of the total ion yields, leaving only very small yields of benzene cations. Carbon atomic cations, C^+, were also produced with the yields of around 20 %. The formation of the small fragment ions such as C^+ was interpreted by the "ladder switching" mechanism,[41,44] in which neutral benzene molecules are ionized first and multiphoton dissociation of the benzene cations occurs to produce molecular fragment ions which then undergo multiphoton dissociation in a sequential manner. This ladder switching mechanism was confirmed by the double laser pulse experiments and the tandem TOF technique.[45-47]

The multiphoton dissociation of benzene cations in nanosecond pulsed laser fields was also investigated at $\lambda \sim 504$ nm, and 259 nm.[45,48] The small differences in the branching ratios of the fragment ions obtained at different wavelengths have been attributed to the differences in the laser field intensity rather than the differences in the wavelength of the laser.[43,45,48]

When the laser intensity of the nanosecond laser pulse was $\sim 10^7$ W / cm^2, benzene cations were dominantly produced.[48] The weak signal of the fragment ions, $C_4H_i^+$, which were directly produced from benzene cations, was also detected. It was found that the ladder switching processes efficiently proceed as the laser intensity increases, and the smaller size fragment ions tend to have larger yields. When the intensity was $\sim 10^9$ W / cm^2, the benzene cation signal disappeared and the atomic carbon ions, C^+, were dominantly produced.[48] This ladder switching process of the ionization and dissociation of benzene was also identified when the 35 picosecond laser pulses ($\lambda \sim$ 532 nm, 10^{13}W/cm^2) were used,[49] indicating that the ladder switching process could proceed within 35 ps.

As demonstrated in the present study, when the 50 fs laser pulses of $\lambda \sim 395$ nm

were employed, the fragmentation into the small ions, $C_2H_k^+$ and C^+, through the ladder switching processes was minor channels. When starting from neutral benzene molecules, the total yields of these small ions were only around 20 % of the yields of $C_4H_i^+$. This suggests that the laser pulse duration of 50 fs is too short for the ladder switching to come into effect.

IV. Conclusion

Using a tandem TOF mass spectrometer, the ionization and dissociation dynamics of the mass-selected benzene cations in intense short pulsed (50 fs) laser fields was investigated. By combining with the corresponding results obtained when starting from the neutral benzene molecules using a single stage TOF mass spectrometer, a remarkable wavelength dependence of the ionization and fragmentation process was identified as summarized in Fig. 5.

When $\lambda \sim 395$ nm, the strong dipole-allowed coupling between the $\tilde{C}$ and $\tilde{X}$ states of the benzene cation suppressed the formation of benzene dications and induced the dissociation into $C_4H_i^+$ or $C_3H_j^+$. It was inferred that the efficient trapping in the singly charged cation stage was induced by the combination of the formation of the light-dressed potential energy surfaces via the coupling between the $\tilde{C}$ and $\tilde{X}$ states and the ultrafast intramolecular decay processes on the multidimensional potential surfaces.

When $\lambda \sim 790$ nm, the multiple ionization was found to dominate the dynamics of benzene cations as well as that of neutral benzene molecules, indicating that a resonance coupling is not induced on either of the neutral, singly charged, or doubly charged stages by the $\lambda \sim 790$ nm light.

References

[1] A. D. Bandrauk, *Molecules in laser fields* (Marcel Dekker, New York, 1993).

[2] K. Codling, and L. J. Frasinski, J. Phys. B **26**, 783 (1993).

[3] J. J. Larsen, H. Sakai, C. P. Safvan, I. Wendt-Larsen, and H. Stapelfeldt, J. Chem. Phys. **111**, 7774 (1999).

[4] H. Rottke, C. Trump, and W. Sandner, J. Phys. B **31**, 1083 (1998).

[5] A. Hishikawa, A. Iwamae, and K. Yamanouchi, Phys. Rev. Lett. **83**, 1127 (1999).

[6] A. Hishikawa, A. Iwamae, and K. Yamanouchi, J. Chem. Phys. **111**, 8871 (1999).

[7] J. H. Sanderson, A. El-Zein, W. A. Bryan, W. R. Newell, A. J. Langley, and P. F. Taday, Phys. Rev. A **59**, R2567 (1999).

[8] A. D. Bandrauk, and M. L. Sink, J. Chem. Phys. **74**, 1110 (1981).

[9] M. V. Fedorov, O.V. Kundrevatova, V. P. Makarov, and A. A. Samokhin, Opt. Commun. **13**, 299 (1975).

[10] A. D. Bandrauk, D. G. Musaev, and K. Morokuma, Phys. Rev. A **59**, 4309 (1999).

[11] H. Kono, private communication.

[12] I. D. Williams, P. McKenna, B. Srigengan, I. M. G. Johnston, W. A. Bryan, J. H. Sanderson, A. El-Zein, T. R. J. Goodworth, W. R. Newell, P. F. Taday, and A. J. Langley, J. Phys. B **33**, 2743 (2000); K. Sändig, H. Figger, and T. W. Hänsch, Phys. Rev. Lett. **85**, 4876 (2000).

[13] M. J. DeWitt, D. W. Peters, and R. J. Levis, Chem. Phys. **218**, 211 (1997).

[14] M. Castillejo, S. Couris, E. Koudoumas, and M. Martin, Chem. Phys. Lett. **289**, 303 (1998).

[15] K. W. D. Ledingham, D. J. Smith, R. P. Singhal, T. McCanny, P. Graham, H. S. Killic, W. X. Peng, A. J. Langley, P. F. Taday, and C. Kosmidis, J. Phys. Chem. A

103, 2952 (1999).

[16] D. J. Smith, K. W. D. Ledingham, R. P. Singhal, H. S. Killic, T. McCanny, A. J. Langley, P. F. Taday, and C. Kosmidis, Rapid. Commun. Mass. Spectrom. **12**, 813 (1998).

[17] A. Talebpour, A. D. Bandrauk, K. Vijayalakshmi, and S. L. Chin, J. Phys. B **33**, 4615 (2000).

[18] M. Castillejo, S. Couris, E. Koudoumas, and M. Martin, Chem. Phys. Lett. **308**, 373 (1999).

[19] S. Shimizu, J. Kou, S. Kawato, K. Shimizu, S. Sakabe, and N. Nakashima, Chem. Phys. Lett. **317**, 609 (2000).

[20] A. M. Müller, C. J. G. J. Uiterwaal, B. Witzel, J. Wanner, and K.-L. Kompa, J. Chem. Phys. **112**, 9289 (2000).

[21] W. C. Wiley, and I. H. McLaren, Rev. Sci. Instr. **26**, 1150 (1955).

[22] A. Hishikawa, A. Iwamae, K. Hoshina, M. Kono, and K. Yamanouchi, Chem. Phys. Lett. **282**, 283 (1998).

[23] A. Hishikawa, A. Iwamae, K. Hoshina, M. Kono, and K. Yamanouchi, Chem. Phys. **231**, 315 (1998).

[24] A. Iwamae, A. Hishikawa, and K. Yamanouchi, J. Phys. B **33**, 223 (2000).

[25] L. V. Keldysh, Sov. Phys. JETP **20**, 1307 (1965).

[26] M. J. Dewitt, and R. J. Levis, J. Chem. Phys. **108**, 7739 (1998).

[27] M. E. Wacks, and V. H. Dibeler, J. Chem. Phys. **31**, 1557 (1959).

[28] P. Baltzer, L. Karlsson, B. Wannberg, G. Ohrwall, D. M. P. Holland, M. A. MacDonald, M. A. Hayes, and W. von Niessen, Chem. Phys. **224**, 95 (1997).

[29] H. Köppel, L. S. Cederbaum, and W. Domcke, J. Chem. Phys. **89**, 2023 (1988).

[30] A. Saenz, J. Phys. B **33**, 4365 (2000).

[31] A. Giusti-Suzor, X. He, O. Atabek, and F. H. Mies, Phys. Rev. Lett. **64**, 515 (1990).

[32] P. H. Bucksbaum, A. Zavriyev, H. G. Muller, and D. W. Schumacher, Phys. Rev. Lett. **64**, 1883 (1990).

[33] A. Zavriyev, P. H. Bucksbaum, H. G. Muller, and D. W. Schmacher, Phys. Rev. A **42**, 5500 (1990).

[34] H. Kühlewind, A. Kiermeier, and H. J. Neusser, J. Chem. Phys. **85**, 4427 (1986).

[35] M. P. de Boer, and H. G. Muller, Phys. Rev. Lett. **68**, 2747 (1992).

[36] R. B. Vrijen, J. H. Hoogenraad, H. G. Muller, and L. D. Noordam, Phys. Rev. Lett. **70**, 3016 (1993).

[37] J. G. Story, D. I. Duncan, and T. F. Gallagher, Phys. Rev. Lett. **70**, 3012 (1993).

[38] A. Talebpour, C.-Y. Chien, and S. L. Chin, J. Phys. B **29**, 5725 (1996).

[39] A. Talebpour, Y. Liang, and S. L. Chin, J. Phys. B **29**, 3435 (1996).

[40] S. R. Long, J. T. Meek, and J. P. Reilly, J. Chem. Phys. **79**, 3206 (1983).

[41] F. Rebentrost, and A. Ben-Shaul, J. Chem. Phys. **74**, 3255 (1981).

[42] P. B. Corkum, Phys. Rev. Lett. **71**, 1994 (1993).

[43] L. Zandee, and R. B. Bernstein, J. Chem. Phys. **71**, 1359 (1979).

[44] W. Dietz, H. J. Neusser, U. Bosel, E. W. Schlag, and S. H. Lin, Chem. Phys. **66**, 105 (1982).

[45] U. Boesl, H. J. Neusser, and E. W. Schlag, J. Chem. Phys. **72**, 4327 (1980).

[46] U. Boesl, H. J. Neusser, and E. W. Schlag, Chem. Phys. Lett. **87**, 1 (1982).

[47] U. Boesl, R. Weinkauf, K. Walter, C. Weickhardt, and E. W. Schlag, J. Phys. Chem. **94**, 8567 (1990).

[48] U. Boesl, J. Phys. Chem. **95**, 2949 (1991).

[49] V. R. Bhardwaj, K. Vijayalakshmi, and D. Mathur, Phys. Rev. A **59**, 1392 (1999).

Table I. Comparison of the previous studies on benzene in intense laser fields

	Wavelength (nm)	Width	Intensity (W/cm^2)	Products [a]	
				Parent ions	Fragment ions [b]
Zandee *et al.*[c]	~ 390	5 ns	~ 10^9		$C_2H_k^+$ (0.3)
					$C_3H_j^+$ (0.2)
					$C_4H_i^+$ (0.2)
					C^+ (0.2)
Bosel *et al.*[d]	259	5 ns	3×10^8		C^+ (0.4)
					$C_2H_k^+$ (0.2)
					$C_3H_j^+$ (0.2)
	504	5 ns	5×10^9		C^+ (0.5)
					$C_2H_k^+$ (0.2)
Bhardwaj *et al.*[e]	532	35 ps	4×10^{13}		C^+ (0.3)
					$C_3H_j^+$ (0.2)
					$C_2H_k^+$ (0.2)
DeWitt *et al.*[f]	780	170 fs	3.8×10^{13}	$C_6H_6^+$ (1.0)	
Castillejo *et al.*[g]	800	200 fs	1×10^{13}	$C_6H_6^+$ (1.0)	
	400		1.2×10^{12}	$C_6H_6^+$ (0.4)	$C_4H_i^+$ (0.4)
Castillejo *et al.*[h]	800	50 fs	2×10^{14}	$C_6H_6^+$ (0.2)	C^+ (0.2)
					$C_3H_j^+$ (0.2)

Talebpour *et al.*[i]	800	200 fs	$< 5\times10^{14}$	$C_6H_6^+$ (0.9)	$C_4H_i^+$ $C_3H_j^+$
Smith *et al.*[j]	750	50 fs	3×10^{14}	$C_6H_6^+$ (0.5) $C_6H_6^{2+}$ (0.3)	
	375	90 fs	1×10^{14}	$C_6H_6^+$ (0.6)	$C_4H_j^+$ (0.2)
Ledingham *et al.*[k]	790	50 fs	2×10^{15}	$C_6H_6^+$ (0.7) $C_6H_6^{2+}$ (0.2)	
Shimizu *et al.*[l]	800	120 fs	1×10^{17}		C^+, C^{2+}

[a] The values in parentheses represent the yield ratio of the product ions to the total yields of all the product ions. [b] The subscripts, i, j, and k, in $C_4H_i^+$, $C_3H_j^+$, and $C_2H_k^+$, could be in the ranges of i = 2 – 4, j = 0 – 3, and k = 0 – 3. [c] Ref. 43. [d] Ref. 46. [e] Ref. 49. [f] Ref. 13. [g] Ref. 14. [h] Ref. 18. [i] Ref. 17. [j] Ref. 16. [k] Ref. 15. [l] Ref. 19.

Table II. The branching ratio of product ions obtained from neutral benzene molecules in intense laser fields (2.0×10^{16} W / cm^2).[a]

Products	λ ~ 790 nm	λ ~ 395 nm	
$C_6H_6^+$	1.00	1.00	
$C_6H_6^{2+}$	0.07	-	
$C_6H_5^+$	-	0.19	
$C_5H_3^+$	-	0.05	
$C_4H_4^+$	-	0.40	1.03
$C_4H_3^+$	-	0.37	
$C_4H_2^+$	-	0.26	
$C_3H_3^+$	-	0.28	0.43
$C_3H_2^+$	-	0.07	
C_3H^+	-	0.08	
$C_2H_3^+$	-	0.07	0.14
$C_2H_2^+$	-	0.07	
C^+	0.07	0.21	

[a] The yield of benzene cations was normalized as unity.

Figure Captions

Fig. 1. The schematic diagram of the tandem time-of-flight mass spectrometer (TOF-MS). In the first TOF-MS stage, the voltages for the first and second electrode plates are set to be V_{A1} = 4185 V and V_{A2} = 3885 V, respectively. In the second TOF-MS stage, the voltages of the second and third grids are set to be V_{B1} = 1400 V and V_{B2} = 1500 V, respectively. The ions with specific mass and charge numbers are decelerated in the region (1) and are exposed to intense laser fields at the equidistant point between the second-grid and third-grid. The product ions are re-accelerated in the region (2).

Fig. 2. The TOF mass spectra obtained when neutral benzene molecules were irradiated by intense laser pulses with the wavelengths of (a) 395 nm and (b) 790 nm. The peak laser-field intensities were set to be ~ 2×10^{16} W / cm^2 for both cases. The ion signals originating from residual gases, N_2, O_2, and H_2O were also identified.

Fig. 3. The momentum-scaled TOF spectra of the atomic carbon cations, C^+ (solid line), which were produced from neutral benzene molecules irradiated by intense laser pulses at (a) 395 nm and (b) 790 nm. The dotted lines in (a) and (b) are the best-fit Gaussian momentum distribution with peak widths (FWHM) of $223(7)\times10^3$ and $274(6)\times10^3$ amu m/s, respectively.

Fig. 4. The TOF spectra obtained when mass-selected benzene cations were irradiated by intense laser pulses with the wavelengths of (a) 395 nm and (b) 790 nm. The peak laser-field intensities were set to be ~ 2.5×10^{16} W / cm^2 for both cases. The peaks with an asterisk (*), two asterisks (**), and three asterisks (***) are those of the $C_6H_5^+$,

$C_6H_4^+$, and $C_5H_3^+$ fragment ions produced by the nanosecond laser pulse after the REMPI process, respectively. The broad tail region around 10.5 μs is ascribed to an artifact appearing as a response of the MCP detector after the strong signal of the benzene cations.

Fig. 5. The schematic diagram of the ionization and fragmentation processes of benzene in intense laser fields. Shorter and longer vertical arrows represent photons with the wavelengths of 790 nm and 395 nm, respectively.

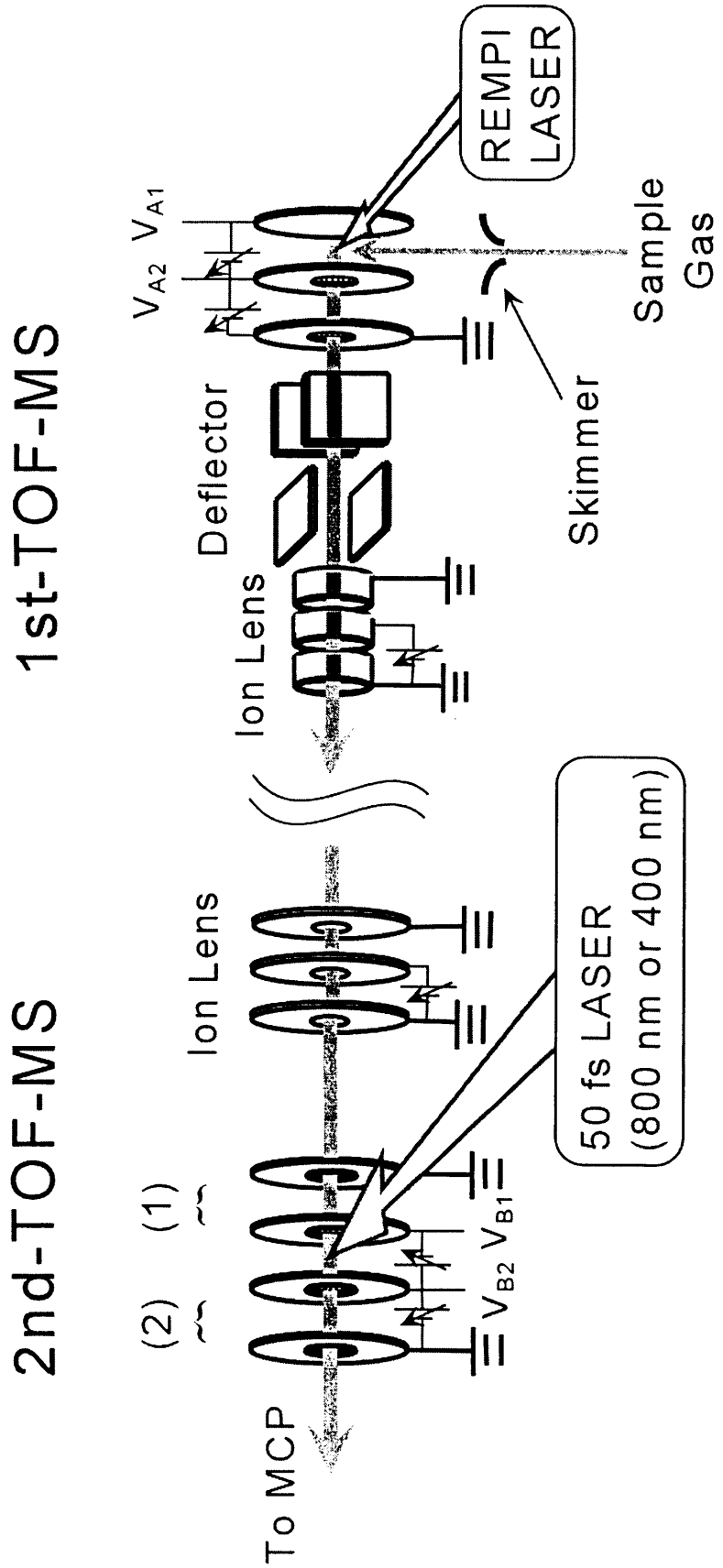
2nd-TOF-MS
1st-TOF-MS
REMPI LASER
Sample Gas
Skimmer
Deflector
Ion Lens
Ion Lens
50 fs LASER (800 nm or 400 nm)
To MCP
(1)
(2)
V_{A1}
V_{A2}
V_{B1}
V_{B2}

Fig. 1

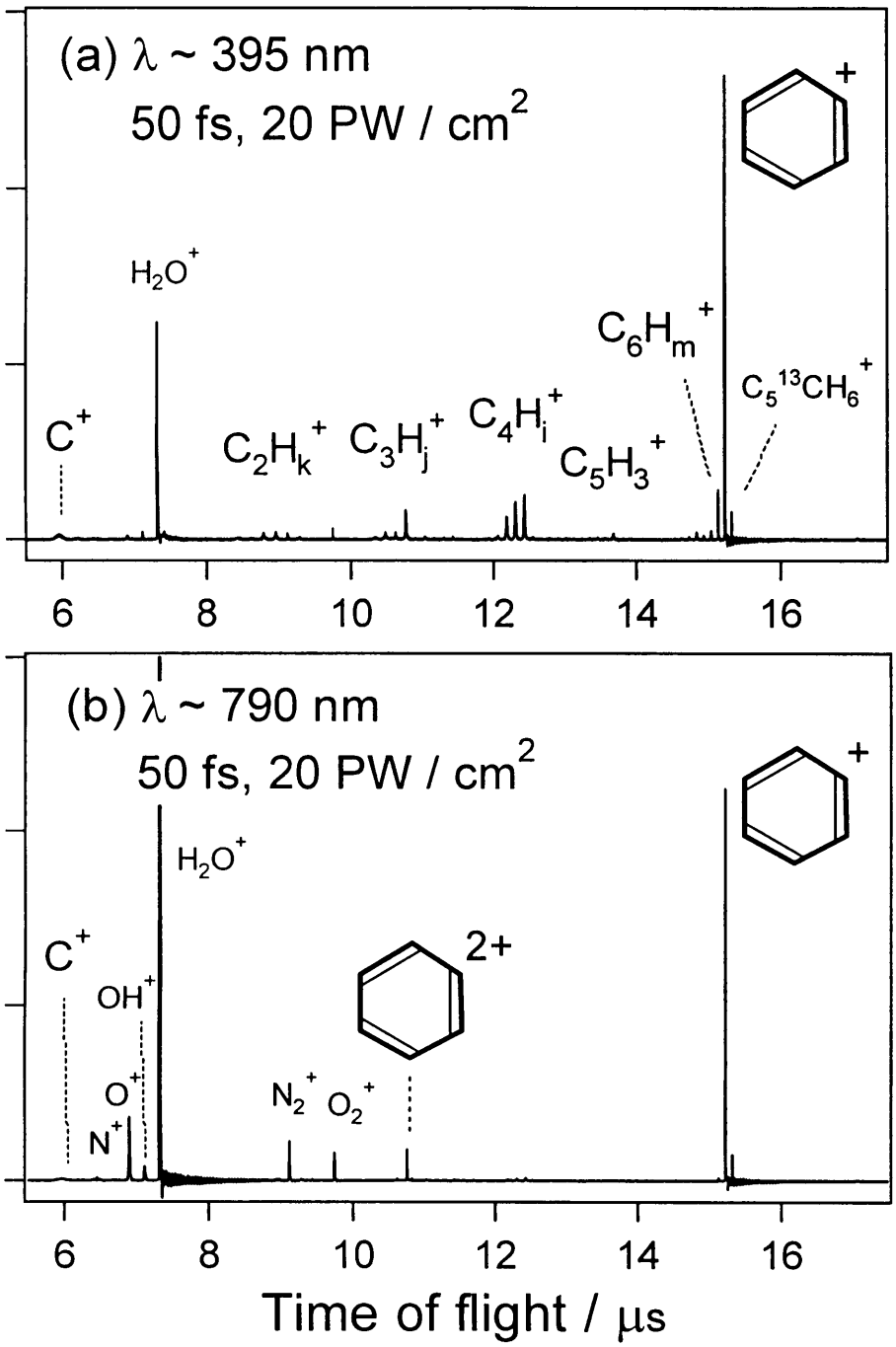
(a) λ ~ 395 nm
50 fs, 20 PW / cm2
H2O+
C+
C2Hk+
C3Hj+
C4Hi+
C5H3+
C6Hm+
C513CH6+
+
6
8
10
12
14
16
(b) λ ~ 790 nm
50 fs, 20 PW / cm2
H2O+
C+
OH+
O+
N+
N2+
O2+
2+
+
6
8
10
12
14
16
Time of flight / μs

Fig. 2

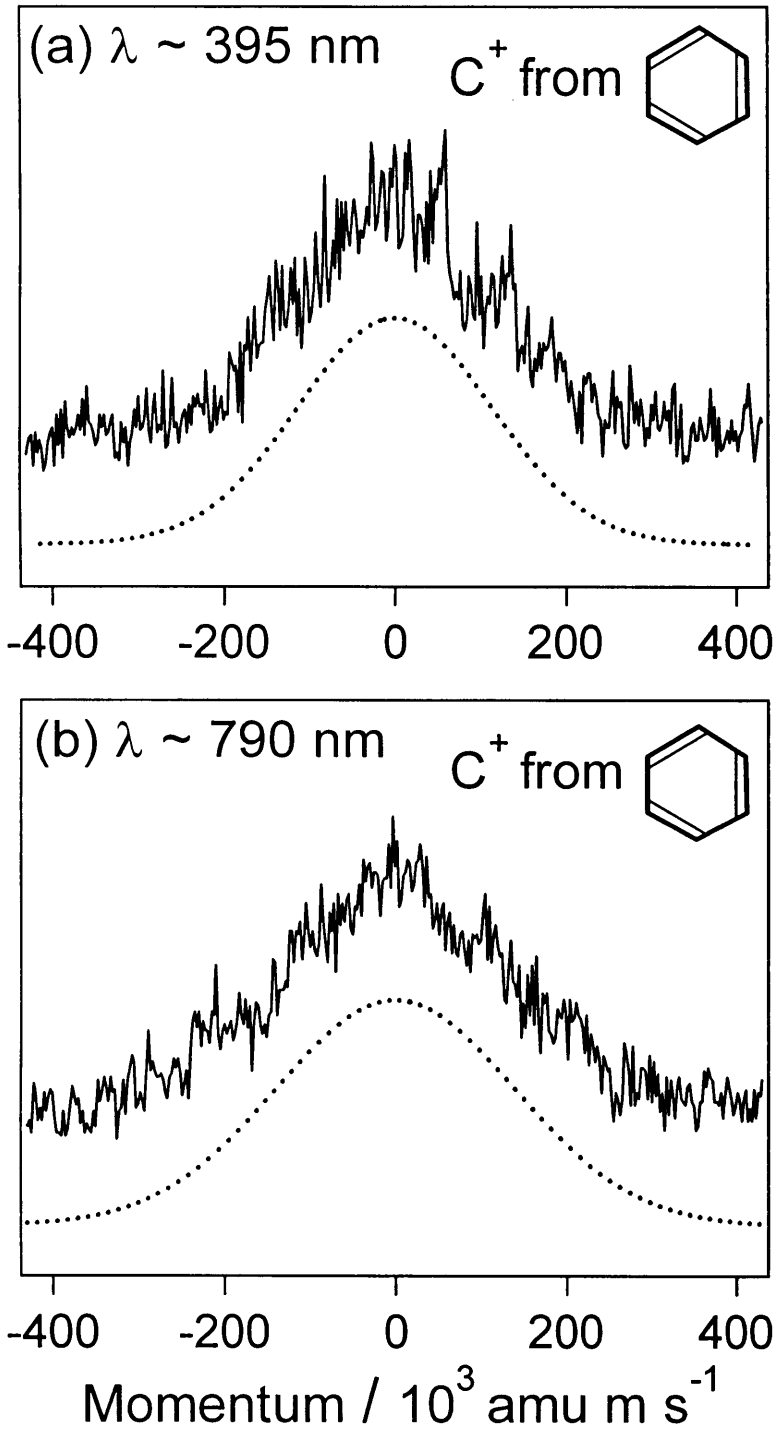
(a) λ ~ 395 nm
C+ from
-400
-200
0
200
400
(b) λ ~ 790 nm
C+ from
-400
-200
0
200
400
Momentum / 10^3 amu m s^-1

Fig. 3

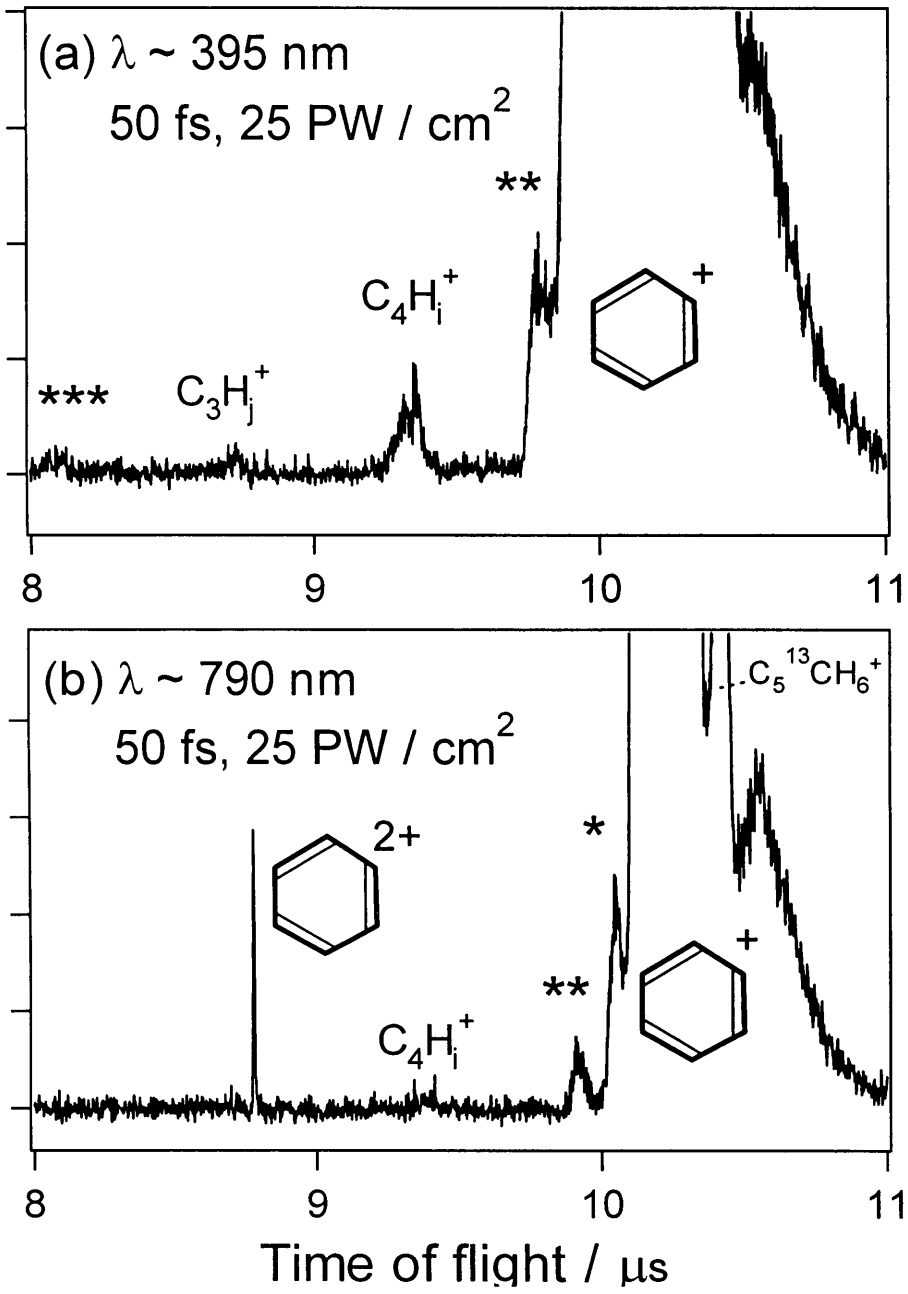
(a) λ ~ 395 nm
50 fs, 25 PW / cm2
**
C4Hi+
***
C3Hj+
+
8
9
10
11
(b) λ ~ 790 nm
50 fs, 25 PW / cm2
C5 13CH6+
2+
*
**
C4Hi+
+
8
9
10
11
Time of flight / μs

Fig. 4

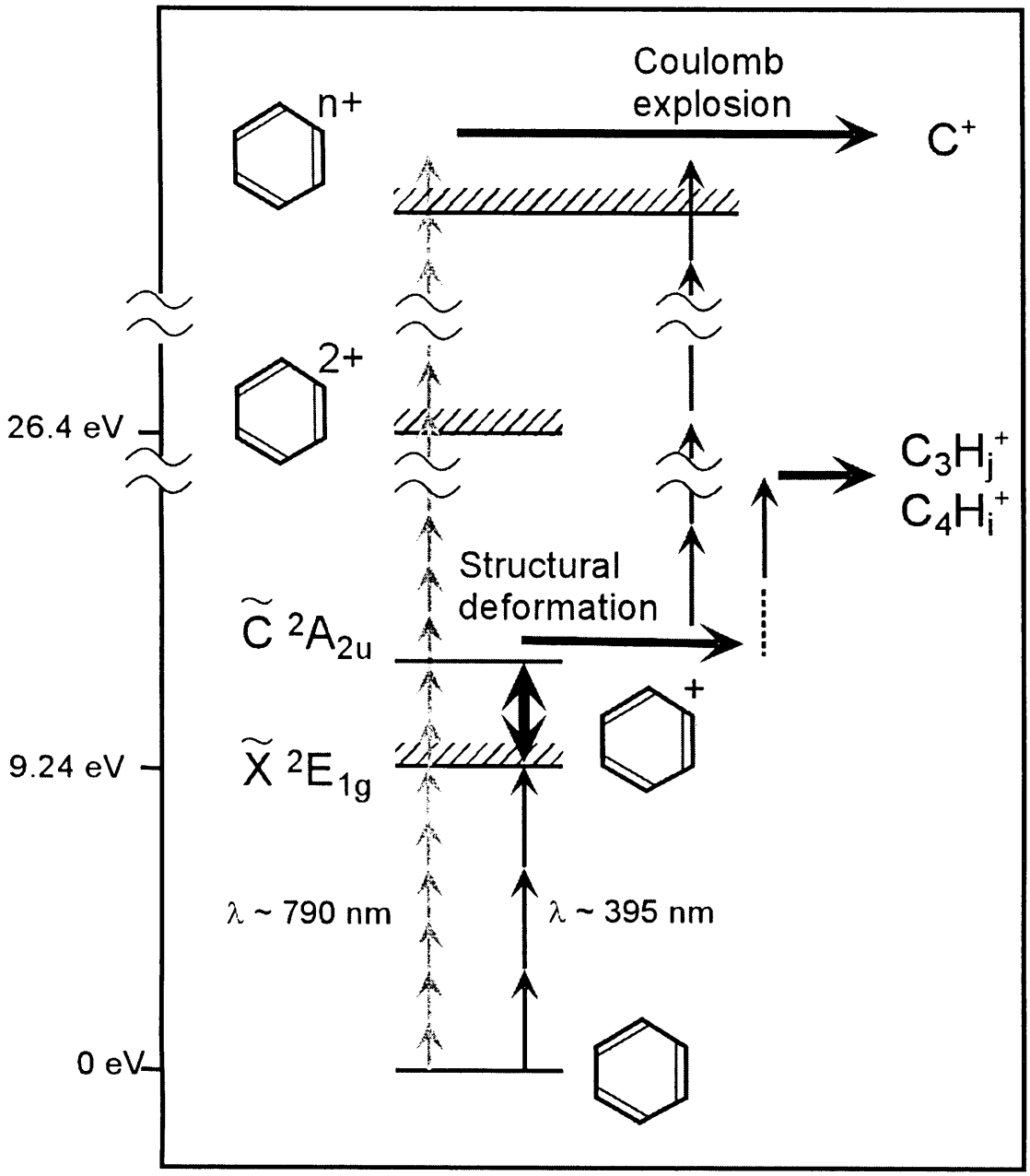
Coulomb
explosion
n+
C+
2+
26.4 eV
C3Hj+
C4Hi+
Structural
deformation
C̃ 2A2u
+
X̃ 2E1g
9.24 eV
λ ~ 790 nm
λ ~ 395 nm
0 eV

Fig. 5

Chapter 5

Summary

The main theme of this thesis is ultrafast unimolecular reaction processes in laser fields. In chapters 2 and 3, the ultrafast state-to-state dissociation dynamics of OCS excited into the VUV wavelength region was investigated. In chapter 4, the ionization and fragmentation dynamics of benzene and singly charged benzene in intense laser fields was investigated. The following two sections are summaries of the contents of this thesis.

I. Ultrafast dissociation of OCS in VUV region

The ultrafast dissociation process of OCS ($2^1\Sigma^+$) in the energy region of vacuum ultraviolet (VUV) light was investigated. The attention was paid to the vibrational Feshbach resonances caused by the quasi-bound vibration of the in-phase C-O and C-S stretching on the $2^1\Sigma^+$ potential energy surface of OCS. OCS was excited to the resonant continuum states by a tunable VUV laser generated by two-photon resonant four-wave different frequency mixing technique. The product state distributions of the CO fragments via the quasi-bound resonant states ($v^* = 0 - 2$) of OCS were measured.

The vibrational state distributions of the CO fragments were investigated through

the momentum distributions of the S(^{1}S) counterpart fragments, which were obtained from the Doppler profiles of the S(^{1}S) fragments. It was found that the vibrational distributions of the CO fragments were approximately represented with the Boltzmann distribution of 7000 K for the dissociation via all the quasi-bound vibrational states, v* = 0 - 2. This result indicates that the vibrational adiabaticity is destroyed completely even if the dissociation occurs within the time scale of the quasi-bound vibrational period.

The rotational state distributions were directly measured through the laser induced fluorescence of the $A^1\Pi$ - $X^1\Sigma^+$ transition of CO ($X^1\Sigma^+$, v_{CO} = 0, 1) by using another tunable VUV laser. The CO fragments in v_{CO} = 0 via the quasi-bound vibrational states, v* = 0 – 2, were found to have a very low rotational temperature. The rotational distributions were approximately represented with the Boltzmann distribution of around 100 K independent of v*. On the other hand, the CO fragments in v_{CO} = 1 were much more excited rotationally than those in v_{CO} = 0, and were approximately represented with the Boltzmann distribution of 2210(280), 940(120), and 810(65) K for the dissociation via the resonant states, v* = 0, 1, and 2, respectively. The significant difference between the rotational distributions of the CO fragments in v_{CO} = 0 and 1 indicates that the bending motion of OCS is not separable from the stretching and dissociative motions on the $2^1\Sigma^+$ potential energy surface. The rotational distributions of the CO fragments in v_{CO} = 1 shows the weak dependence of v*. This dependence might reflect the contribution of the bending motion to the respective quasi-bound resonant states.

From the measurements of the vibrational and rotational distributions of the CO fragments, it was found that the complex mixing among the vibrational modes of OCS

exists in the course of the ultrafast dissociation.

The VUV-VUV pump-probe experiments using two tunable VUV lasers would extend the research area in the VUV wavelength region where a lot of interesting issues about unimolecular reactions could be investigated.

II. Benzene in intense laser fields

In intense laser fields, multi-electron molecules are almost multiple-ionized. In most of the previous studies, neutral molecules are exposed to intense laser fields and the fragment ions produced after the multiple ionization are detected. Therefore, the ionization process from a neutral stage to multiply charged parent ions from which Coulomb explosion occurs is ambiguous. In this thesis, in order to investigate the dynamics starting from a specific charge stage, a tandem type time-of-flight mass spectrometer was applied to prepare the singly charged benzene cations.

When the neutral benzene molecules were exposed to the intense laser fields, the ionization and fragmentation of benzene in intense laser fields showed an obvious dependence on the laser wavelength. Although the benzene cations were the major products at both of $\lambda \sim 395$ and 790 nm, the products with the second largest yields were $C_4H_i^+$ at $\lambda \sim 395$ nm, and $C_6H_6^{2+}$ at $\lambda \sim 790$ nm. When the intense laser pulses with the wavelength of $\lambda \sim 395$ nm were used, the fragmentation to $C_4H_i^+$ and $C_3H_j^+$ is dominant except for the ionization to $C_6H_6^+$. On the other hand, when the intense laser pulses with the wavelength of $\lambda \sim 395$ nm were applied, the multiple ionization to $C_6H_6^{2+}$ dominated over the fragmentation.

In order to clarify at which charged stage and in which electronic state these fragmentation occurs, the initially prepared benzene cation in intense laser fields was

investigated. The benzene cations were ionized into the lower vibrational levels in the electronic ground state through the resonantly enhanced multiphoton ionization by using the nano-second pulsed dye laser.

When the laser wavelength was $\lambda \sim 395$ nm, the fragmentation to $C_4H_i^+$ was dominant and $C_3H_j^+$ was also detected. It was found that the ionization to the benzene dication, $C_6H_6^{2+}$, was suppressed, even if the starting point was the singly charged stage. This suppression of the ionization to the dication and the fragmentation of $C_4H_i^+$ and $C_3H_j^+$ was attributed to the dipole allowed strong coupling between the $\tilde{C}$ and $\tilde{X}$ states of benzene cation in intense laser fields. It was considered that the population trapping in the singly charged cation stage was efficiently induced by the light-dressed potential energy surfaces composed of the $\tilde{C}$ and $\tilde{X}$ states and that it induced the ultrafast structural deformation.

When the initially prepared benzene cations were irradiated with the intense laser pulse whose wavelength was $\lambda \sim 790$ nm, the benzene cations were ionized mainly to the multiply charged parent ions, $C_6H_6^{2+}$ and $C_6H_6^{3+}$ in a similar manner as the neutral benzene molecules. This suggested that, in the intense laser fields of $\lambda \sim 790$ nm, the resonant coupling leading to the efficient population trapping could not be realized on either of the neutral, singly charged, or doubly charged stages.